Andrej Tomeljak

NONEQUILIBRIUM DYNAMICS OF CHARGE AND COLLECTIVE MODES IN CHARGE DENSITY WAVE COMPOUNDS

Doctoral Dissertation

NERAVNOVESNA DINAMIKA NABOJA IN KOLEKTIVNIH MODOV V SNOVEH Z VALOM GOSTOTE NABOJA

Doktorska disertacija

Supervisor: Assist. Prof. Dr. Jure Demšar

September 2009

MEDNARODNA PODIPLOMSKA ŠOLA JOŽEFA STEFANA
JOŽEF STEFAN INTERNATIONAL POSTGRADUATE SCHOOL
Ljubljana, Slovenia

Contents

Abstract

This thesis presents studies of ultrafast carrier relaxation dynamics in charge density wave (CDW) materials by means of *femtosecond time-resolved optical spectroscopy*. In these experiments, a femtosecond *pump* pulse excites electrons via interband transitions, thereby changing the optical properties of the material. The dynamics of relaxation processes is then recorded by measuring the resulting photoinduced changes in the dielectric function as a function of time after photoexcitation. Utilizing this technique, one can therefore measure the non-equilibrium quasiparticle and phonon relaxation dynamics in real time.

The motivation for this research was on one side the major progress that has been made in the last couple of years in theoretical understanding of the relaxation phenomena in systems with a narrow gap in the density of states. The Rothwarf-Taylor (RT) model, developed for understanding the non-equilibrium dynamics in superconductors was originally used to interpret the relaxation phenomena in CDWs as well. On the other hand, several arguments could be made against the simple RT model interpreted in CDWs. Using *femtosecond time-resolved optical spectroscopy*, we systematically measured the temperature and excitation intensity dependence of photoinduced reflectivity changes in CDW materials $K_{0.3}MoO_3$ and $(TaSe_4)_2I$. We found that at low perturbations the quasiparticle relaxation dynamics is excitation intensity independent, which speaks against the validity of the RT model in CDW materials and calls for the models to be revisited.

The reason for choosing these particular two prototype CDW materials, i.e. $K_{0.3}MoO_3$ and $(TaSe_4)_2I$, was to compare the ultrafast dynamics of weakly and strongly coupled CDW systems. The aim was to understand their dynamics in order to gain further complementary knowledge about these materials and the role of interaction strengths in CDW physics. Surprisingly, we have shown that the temperature evolution of the electronic and phonon responses in both systems were qualitatively the same.

We have also systematically explored for the first time the high perturbation physics in both CDW materials and found that non-thermal melting of the CDW can be achieved. The temperature evolution of the energy E_{sat} needed to induce CDW meltdown was also studied. In fact, the uncharacteristically low value for E_{sat} in $(TaSe_4)_2I$, as compared

to $K_{0.3}MoO_3$, was the only clue suggesting any qualitative difference between the two systems.

Systematic studies, where the excitation intensity was changed by more than four orders of magnitude, suggest that during the process of melting and sub-ps recovery of the electronic modulation, the electronic and lattice systems are uncoupled. This could explain why the order parameter recovery is so extremely fast ($\tau \approx 200$ fs) in this entire class of low-dimensional materials, because a frozen lattice and consequent $2k_F$ modulation would present a strong potential well driving ultrafast reformation of the charge density modulation.

Finally, we grew a series of thin $K_{0.3}MoO_3$ films using pulsed laser deposition. The films were characterized using various experimental techniques including *femtosecond time-resolved optical spectroscopy*. We observed the amplitude mode along with zone-folding phonons characteristic for $K_{0.3}MoO_3$, proving existence of CDW domains. The systematic study of temperature and excitation intensity dependence of relaxation dynamics in films revealed that there is no major difference between the CDW physics of $K_{0.3}MoO_3$ in films or in bulk.

KEY WORDS: Carrier relaxation dynamics, femtosecond time-resolved optical spectroscopy, charge density waves.

PACS: 78.47.J-, 71.45.Lr, 72.15.Nj

Povzetek

V tem delu predstavljamo raziskavo ultrahitre relaksacijske dinamike nosilcev naboja v materialih z valom gostote naboja (VGN) s pomočjo *femtosekundne časovno ločljive spektroskopije*. Pri tej tehniki s femtosekundnim *vzbujevalnim* sunkom vzbudimo elektrone v višja stanja in s tem spremenimo optične lastnosti snovi. Dinamiki relaksacijskih procesov nato sledimo s tem, da merimo fotoinducirane spremembe v dielektrični funkciji kot funkcijo časa po fotovzbuditvi. Z uporabo te metode lahko torej merimo dinamiko relaksacije kvazidelcev in kolektivnih eksitacij VGN ter fononov v realnem času.

Ena od motivacij, da smo se teh raziskav lotili, je bil ogromen napredek zadnjih let pri teoretičnem razumevanju relaksacijskih pojavov v sistemih z majhno energijsko režo v gostoti stanj. Model Rothwarfa in Taylorja (RT), ki je bil razvit za razumevanje neravnovesne dinamike v superprevodnikih, je bil namreč prvotno uporabljen tudi pri razlagi neravnovesnih pojavov v snoveh z VGN. Po drugi strani pa je veliko opažanj, kot npr. dve časovni skali v snoveh z VGN, ki so temeljno različna med obema sistemoma. S pomočjo *femtosekundne časovno ločljive spektroskopije* smo kot funkcijo temperature in moči vzbujanja sistematično merili spremembe v odbojnosti v $K_{0.3}MoO_3$ in $(TaSe_4)_2I$. Ugotovili smo, da je relaksacijska dinamika pri majhnih perturbacijah sistema neodvisna od moči vzbujanja, kar govori proti veljavnosti modela RT.

$K_{0.3}MoO_3$ in $(TaSe_4)_2I$ smo izbrali z namenom, da bi primerjali šibko in močno sklopljena sistema z VGN. Dodatno znanje o teh snoveh, predvsem boljše razumevanje o vlogi moči interakcij v fiziki VGN, smo želeli pridobiti preko boljšega razumevanja relaksacijske dinamike. Proti pričakovanjem smo pokazali, da je temperaturna odvisnost elektronskega in fononskega odziva v obeh sistemih kvalitativno enaka.

Prvič do zdaj smo sistematično raziskali tudi fiziko visokih vzbuditev v obeh snoveh z VGN in ugotovili, da lahko uničimo VGN povsem netermalno. Izmerili smo tudi temperaturno odvisnost energije E_{sat}, ki je potrebna za uničenje VGN in ugotovili, da je neznačilno nizka E_{sat} v $(TaSe_4)_2I$ edini namig o kvalitativni razliki med obema sistemoma.

Sistematične raziskave, v sklopu katerih smo moč vzbujanja spreminjali za več kot za štiri rede velikosti, kažejo na to, da so v času na časovni skali pod ps, ko pride do uničenja in ponovne vzpostavitve VGN, elektroni in mreža nesklopljeni. S tem bi lahko pojasnili, zakaj poteka ponovna vzpostavitev parametra reda na tako hitri časovni skali ($\tau \approx 200$ fs) v tej skupini nizkodimenzionalnih snovi. Nevzbujena mreža namreč ostane modulirana z valovnim vektorjem $2k_F$, kar ustvari potencialno jamo, ki pospeši ponovno vzpostavitev VGN.

Za zaključek smo s pomočjo sunkovne laserske depozicije naredili celo serijo tankih filmov $K_{0.3}MoO_3$. Filme smo karakterizirali s pomočjo različnih eksperimentalnih metod vključno s *femtosekundno časovno ločljivo spektroskopijo*. Poleg amplitudnega moda smo izmerili več različnih fononov, ki so karakteristični za $K_{0.3}MoO_3$ in s tem dokazali obstoj domen z VGN. Sistematična raziskava relaksacijske dinamike kot funkcije temperature in moči vzbuditve je pokazala, da v primeru $K_{0.3}MoO_3$ ni bistvene razlike med fiziko VGN v filmih in kristalu.

PREDMETNE OZNAKE: Relaksacijska dinamika nosilcev naboja, femtosekundna časovno ločljiva spektroskopija, val gostote naboja.

STVARNI VRSTILEC: 78.47.J-, 71.45.Lr, 72.15.Nj

Abbreviations

1D	=	**1 D**imensional
3D	=	**3 D**imensional
AOM	=	**A**cousto **O**ptic **M**odulator
AM	=	**A**mplitude **M**ode
ARPES	=	**A**ngular **R**esolved **P**hotoelectron **S**pectroscopy
AFM	=	**A**tomic **F**orce **M**icroscopy
CDW	=	**C**harge **D**ensity **W**ave
CW	=	**C**ontinuous **W**ave
DC	=	**D**irect **C**urrent
DECP	=	**D**isplacive **E**xcitation of **C**oherent **P**honons
FFT	=	**F**ast **F**ourier **T**ransform
FWHM	=	**F**ull **W**idth **H**alf **M**aximum
HFP	=	**H**igh **F**requency **P**honon
PI	=	**P**hoto**i**nduced
PLD	=	**P**ulsed **L**aser **D**eposition
QP	=	**Q**uasi**p**article
RT	=	**R**othwarf-**T**aylor
SC	=	**Super**counductor
STO	=	**S**r**T**i**O**$_3$
TR	=	**T**ime **R**esolved
TA	=	**T**ransversal **A**coustic
TO	=	**T**ransversal **O**ptical
TRARPES	=	**T**ime **R**esolved **ARPES**
UED	=	**U**ltrafast **E**lectron **D**iffraction
XRD	=	**X**-**R**ay **D**iffraction

Chapter 1

Introduction

Throughout the history of humankind the development of technology has, hand in hand with the development of new experimental techniques, led to exploration of phenomena on ever shorter time scales. One of the frontiers was reached when in 1999 Ahmed Zewail was awarded the Nobel Prize in Chemistry for "showing that it is possible with rapid laser techniques to see how atoms in a molecule move in a chemical reaction" [1]. At the same time, the power and utility of ultrafast femtosecond optical pump-probe spectroscopies became clear and led to further discoveries in both physics and chemistry.

In femtosecond time-resolved techniques the sample under investigation is photoexcited by a femtosecond optical pulse and the resulting relaxation dynamics is measured by following the dynamics of changes in the dielectric function (ultrafast optical spectroscopy), the structural parameters (mainly ultrafast X-ray diffraction [2–5] and X-ray absorption fine structure [6] and more recently also ultrafast electron diffraction [7–9]) or momentum and energy dependence of the electron occupation number (time and angular resolved photoelectron spectroscopy (TRARPES)[10, 11]) as a function of the time delay after perturbation. The discovery of Ti:sapphire lasers and the subsequent development of ultrafast lasers [12] has led to commercial lasers with pulse durations shorter than 10 fs. Since the pulse duration determines the time resolution of the technique, typical time-scales in condensed matter can be probed. Typical time-scales of interest range from tens of femtoseconds in the case of electron-electron interactions, to tens of picoseconds for electron-phonon, spin-lattice or phonon-phonon processes. Importantly, due to typical penetration depths on the order of 100 nm, one can consider the technique (with the exception of TRARPES) to probe bulk properties. Also, one of the characteristics of the approach is that the investigated system is driven out of the thermodynamic equilibrium by the photoexcitation pulse, however since one of the qualities of the technique is high

sensitivity (relative changes of optical properties of the order of 10^{-7} can be measured), studies close to equilibrium are possible.

The most extensively and successfully studied materials using different pump-probe techniques include simple metals, semiconductors and semiconductor nanostructures [13]. The success of these techniques in the past 20 years was mostly based on a well known electronic band structure. However, the focus of attention in condensed matter physics has switched to strongly correlated systems in the past decade or so, mostly due to the heightened interest in these technologically important systems. This led to significant progress in the field of ultrafast phenomena in strongly correlated systems, even though their electronic structure is complicated and in general not agreed upon. Systematic studies implementing pump-probe techniques on high temperature superconductors [14–18], colossal magneto-resistance compounds [19–22], low-dimensional charge density waves [23, 24] and heavy fermions [25, 26] have shown that these techniques can yield new, important and complementary (to the more conventional time-averaging frequency-domain spectroscopies) information on the low energy electronic structure, together with interaction strengths between various degrees of freedom (electronic, lattice, spin, orbital). On top of that, recent studies of manganites [27], high temperature superconductors [28] and low-dimensional charge density waves [29] have shown that the technique can be used to nonthermally switch the electronic phase on a femtosecond time scale, opening up new possibilities in technological applications.

The first time resolved measurements of the photoexcited relaxation dynamics on the charge density wave (CDW) compounds were performed on the prototype quasi-1D CDW semiconductor blue bronze $K_{0.3}MoO_3$ [23] (see Figure 1.1). These experiments showed dramatic changes in the dynamics upon cooling through the CDW transition temperature $T_c^{3D} = 183$ K. Four distinct components have been observed in the photoinduced reflectivity transient, all showing sensitivity to the CDW transition. The first was an oscillatory component attributed to the coherently excited amplitude mode of the CDW[1]. In addition, there were also two distinct fast decay components which were well fitted by a double exponential decay with decay times 0.5 ps and 10 ps, respectively. The fast decaying component displayed critical behavior near T_c^{3D} tying it to the dynamics of the CDW order parameter. Its temperature dependence was very similar to the dynamics in cuprate superconductors, and was therefore attributed to the single particle recombination dynamics, which is in the phonon bottleneck scenario governed by the decay of phonons with energy higher than 2Δ, Δ being the magnitude of the single particle gap in the density of states. The slowly decaying component was tentatively attributed to the overdamped phase mode of the CDW since the damping constant

[1] See Section 2.5.

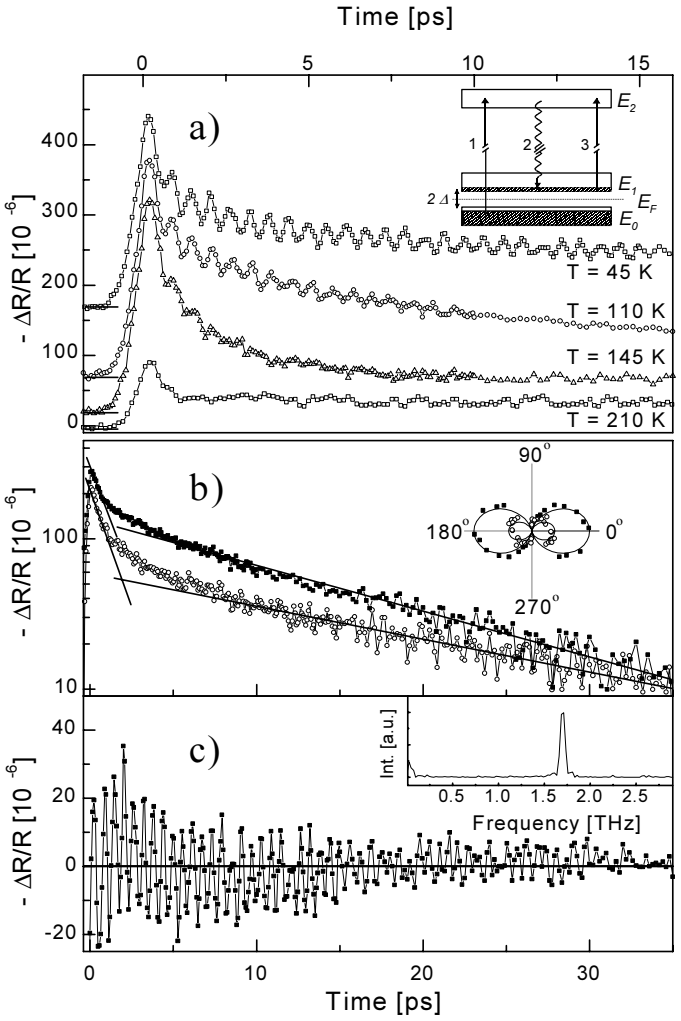

FIGURE 1.1: The first published ultrafast measurements on a CDW material [23]. a) shows the transient change of reflectivity of $K_{0.3}MoO_3$ after being excited with an ultrafast laser pulse at different temperatures below and above the transition temperature $T_c = 183$ K. b) shows the data in a semi-logarithmic scale to emphasize bi-exponential decay behavior. c) shows the oscillatory part of the signal which the authors recognized as the oscillations of the amplitude of the CDW.

matched the width of the phase mode line. Finally, the long lived component was observed with decay time much longer than 10 ns, which was attributed to photogenerated in-gap localized states.

Since the first report [23] several experimental papers have been published on ultrafast dynamics in a variety of CDW systems, adding experimental pieces to the CDW puzzle. A brief chronological overview of the more interesting publications starts in 2002 when Demsar et al. [24] showed that the dynamics in 1T-TaS_2 and 2H-$TaSe_2$ display the same qualitative behavior as the dynamics in $K_{0.3}MoO_3$ [23]. Mihailovic et al. [30] discussed the use of CDW materials as THz optical modulators for femtosecond data storage as they used a three-pulse experiment to show that the CDW amplitude mode can be coherently enhanced or suppressed in 1T-TaS_2 crystals. The coherent control mechanism

was later shown to be general as it was also observed in $K_{0.3}MoO_3$ [31]. In 2004 Ren et al. [32] revisited the original experiment [23] but used different probing wavelengths to measure the dependence of different signal components. Besides from the optical-like amplitude mode, they observed an acoustic mode which they suggested were the oscillations of the transversal CDW phason[2] since its dispersion relation corresponded to the theoretically predicted behavior for a phason [33].

This is roughly where the research presented in this thesis sets in. At that point, several open questions about the CDW dynamics had yet to be resolved, e.g. one of the most interesting puzzles was why the time-scale of the initial electronic relaxation in different CDW materials was about one order of magnitude faster than in superconductors. Also, the low temperature ($T < 50$ K) and excitation intensity dependent measurements were still missing. On top of that, there were questions about the initial theoretical description of the CDW relaxation [23], e.g. 2Δ is comparable to the phonon cut-off frequency, in some compounds even much larger. The tentative assigment of the phase mode to the picosecond relaxation component in the original work [23] also presented a challenge - even if the phase mode had been observed, it was unclear how an IR active mode would cause the measured reflectivity change. On the other hand, our laser system (described in Chapter 3) was much improved since the original report [23], providing much better signal to noise ratio and enabling us to reach orders of magnitude higher laser pulse energies. This, combined with further progress in the theory describing the relaxation in gapped systems [34], led us to expand our research efforts to resolve some of the open questions. Using *femtosecond time-resolved optical spectroscopy*, we systematically measured the temperature and excitation intensity dependence of photoinduced reectivity changes in CDW materials $K_{0.3}MoO_3$ and $(TaSe_4)_2I$. Due to high signal to noise ratio, we were able to systematically measure for the first time the CDW dynamics in $K_{0.3}MoO_3$ at near equilibrium conditions in a temperature range from 4 K – 300 K [35]. The most important observation from these measurements was the lack of excitation intensity dependence in the relaxation dynamics over orders of magnitude in excitation intensity. This result was inconsistent with the theoretical predictions [36]. We also for the first time systematically explored the relaxation dynamics in the high perturbation regime [29]. This study provided us with several important findings. We learned that the CDW can be nonthermally melted, we measured the energy required to induce the CDW meltdown and perhaps most importantly, we observed that the electron and lattice systems seem to be uncoupled on very short time scales [29, 35]. Our research continued with a similar study of the quasi one-dimensional CDW system $(TaSe_4)_2I$, which is often discussed in the framework of the strong coupling theory [37]. Our motivation was to learn more about the role of electron-phonon coupling strength

[2] See Section 2.5

in CDW phenomena. We managed to obtain only limited evidence for the difference between the two CDW systems which will be discussed in Chapter 5. At the same time, a lot of effort was put into growing thin $K_{0.3}MoO_3$ films which would enable one to gain complementary or new information about the CDW relaxation dynamics by probing the ultrafast dynamics with electron or THz pulses (see Section 4.4.1). So far we investigated several films by means of *femtosecond time-resolved optical spectroscopy* and the results suggest that we managed to grow polycrystalline films that qualitatively display very similar relaxation dynamics as bulk (see Section 4.4.3).

In parallel with our research, there were several interesting publications by other groups that were consistent with our conclusions. Toda et al. [38] focused their attention to the phonon spectrum of the 2D CDW material 1T-TaS_2, which contains zone-folded modes in addition to the amplitude mode. They observed that while the amplitude mode appeared instantaneously after perturbation, the strongest zone-folded mode showed a gradual increase. Their temperature dependences indicated that the rise time of the zone-folded mode was strongly correlated to the decay of both amplitude mode and single particle relaxation[3]. The same group also expanded their research interest on $NbSe_3$ [39] which is a very interesting material to explore CDW physics since $NbSe_3$ crystallizes in the form of whiskers which then naturally form ring, Möbius and figure-of-eight geometries. They were able to show that the single particle relaxation time divergence is quenched in quasi-one-dimensional ring crystals (as opposed to whiskers) and proposed an explanation in terms of the enhanced phase fluctuation in the closed-loop topology (see Figure 1.2). They also proposed an interesting suggestion that there were two distinct CDW phases in $NbSe_3$ and tested their claim by measuring the transient response using different photon energies [40]. Their results suggested that specific signal components couple differently to different probe wavelengths. Consequently they successfully found the photon energy range where just a single phase was probed. In 2007 $K_{0.3}MoO_3$ was again studied using time-resolved spectroscopy, ellipsometry, and polarized Raman spectroscopy [41]. In addition to the amplitude mode observed before [23], two additional phonons were observed and attributed to zone folding modes associated with the CDW transition. Photoexcitation intensity dependence was also measured and it showed that the single particle (incoherent electronic signal) and amplitude mode signal components scale differently with excitation fluence. This made it questionable whether displacive excitation of coherent phonons is indeed the generating mechanism for the observed amplitude mode. Instead, a phenomenological model was proposed in which the ultrafast decay of the photo excited quasiparticles is responsible for transferring the energy to the coherent excitation. The frequency-dependent experiments were also

[3]One can observe this also in $K_{0.3}MoO_3$, however it is our conclusion that the observed phenomenon in both materials is due to beating of two modes that are close to each other (see Chapter 4).

in line with the proposed generation mechanism as the transient reflectivity response was found to be consistent with the equilibrium absorption determined by ellipsometry measurements. The second conclusion from the wavelength-dependent experiments was that the generation of coherent amplitudons and quasiparticles is strongly enhanced for wavelengths in the vicinity of the interband plasmon, suggesting an efficient coupling of the charge excitations to the interband plasmon excitations. In 2008 Yusupov et al. [42] investigated for the first time the evolution of the CDW gap and the coupling of the amplitude mode and single-particle excitations with phonons in the 1d- and 2d-ordered states of three tritellurides: $HoTe_3$, $DyTe_3$ and $TbTe_3$. The data from all three different componds were qualitatively similar to the data for other CDW compounds although one should note the high signal to noise ratio in these experiments.

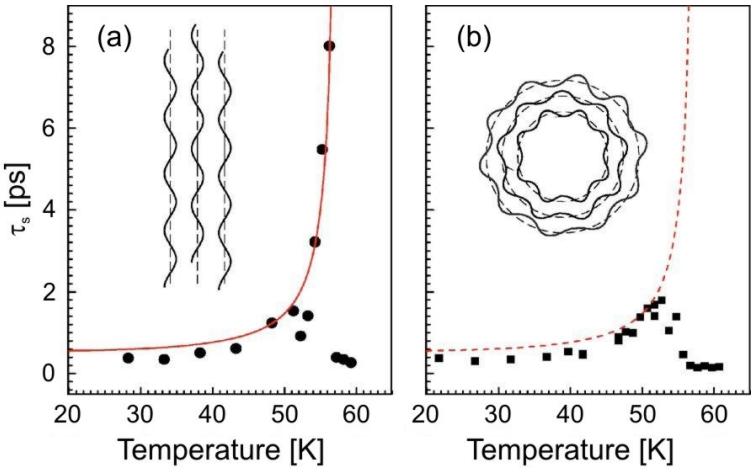

FIGURE 1.2: Comparison of the temperature dependencies of the relaxation times in (a) whisker and (b) closed loop topologies show that CDW is suppressed in the latter case [39].

The other experimental technique that further elucidated the nature of the femtosecond dynamics in CDW materials combined ultrafast laser sources with angular resolved photoelectron spectroscopy (ARPES). So called time resolved ARPES is especially powerful since it directly monitors the temporal evolution of the electronic distribution after photoexcitation with an optical pulse. Perffeti et al. [10, 11] measured the transient ARPES spectra in 1T-TaS_2 after an intense infrared excitation pulse induced an insulator to metal transition and the excitation of a coherent phonon mode (see Figure 1.3). Their measurements confirm the original assignment of the amplitude mode [24]. On the other hand, the measurements also show that upon photoexcitation of the insulating phase the electronic gap quasi-instantaneously collapses and subsequently recovers on a subpicosecond timescale. Very recently, Schmitt et al. did a similar experiment in $TbTe_3$ [43]. They drove a transient charge density wave melting, excited collective vibrations, and observed them through their time-, frequency-, and momentum-dependent influence on the electronic structure. The technique enabled the authors to identify the

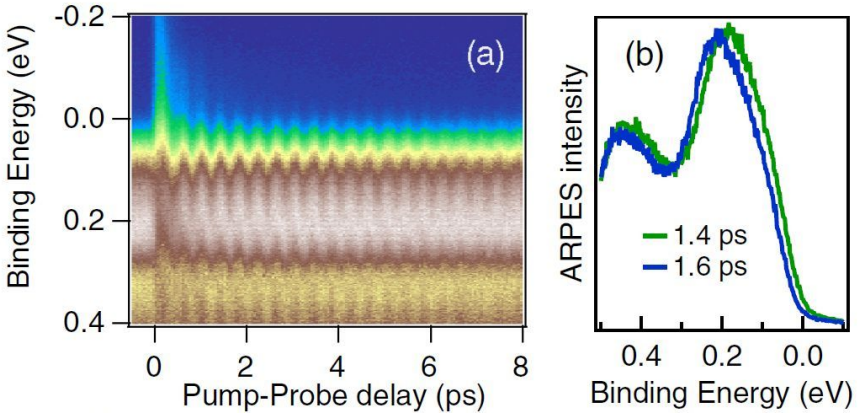

FIGURE 1.3: (a) Time resolved ARPES spectra of 1T-TaS_2 measured in Ref [10] as a function of pump-probe delay and binding energy. (b) Two spectra acquired on a maximum and minimum of one CDW oscillation period display a rigid shift with respect to each other.

role of the observed collective vibration in the transition and to document the transition in real time. More importantly, both time resolved ARPES studies provided an explicit link between the amplitude mode and CDW gap modulation via momentum-dependent analysis[4].

1.1 Scope of the Dissertation

In Chapter 2 we present the basic phenomenology of the physics of charge density waves.

In Chapter 3 we present the pump-probe technique, we describe the two experimental set-ups used in our measurements and we discuss the heating effects that are commonly experienced in these type of experiments. In the last part of Chapter 3, fitting of ultrafast transients is discussed.

In Chapter 4 we present a series of experiments on the prototype CDW materials $K_{0.3}MoO_3$ and $Rb_{0.3}MoO_3$ divided into three parts. First, the data obtained on $K_{0.3}MoO_3$ and $Rb_{0.3}MoO_3$ crystals in the low perturbation regime are presented and discussed. The lack of excitation intensity is observed at $T = 4$ K over several orders of magnitude, together with the lack of relaxation dynamics dependence on external field. The results suggest that the strong bottleneck description of the dynamics and the assignment of the 10 ps relaxation time to the phase mode need to be reconsidered. The data obtained on $K_{0.3}MoO_3$ crystals in the high perturbation regime are presented and discussed in the second part of Chapter 4. It is shown that the CDW can be nonthermally melted and

[4]In a nesting-driven CDW, the electrons are most susceptible to scattering by the CDW phonon wave vector (see Equation 2.7 in Section 2.2).

the temperature dependence of the energy needed to induce the CDW meltdown is measured. The final Section of Chapter 4 presents our efforts to grow thin $K_{0.3}MoO_3$ films. We first discuss the film characterization and then present the photoinduced reflectivity transients in both low and high perturbation regimes.

In Chapter 5 we present pump-probe experiments on $(TaSe_4)_2I$ in the low and high perturbation regime. The main motivation for these measurements was to see how electron-phonon coupling strength affects the CDW response dynamics, however the results seem to suggest little qualitative difference between the weakly coupled (i.e. $K_{0.3}MoO_3$) and strongly coupled (i.e. $(TaSe_4)_2I$) systems.

In Chapter 6 the main results are summarized.

Chapter 2

Physics of Charge Density Waves

2.1 Introduction

The first time that charge density wave (CDW) materials were postulated was more than 50 years ago when Fröhlich (1954) [44] and Peierls (1955) [45] discussed that a highly anisotropic metal would undergo a transition into a new ground state with decreasing temperature. It will be shown in Section 2.2 that reducing the dimensionality of a metal from 3D to 1D causes divergence in the electronic response function $\chi(2k_F)$. This drives the transition to a new ground state with a spatial modulation of the charge density and ionic positions (hence the name charge density wave). The transition occurs because the system gains energy due to the opening of a gap in the density of states at the Fermi energy. The opening of a gap causes the electron system to gain energy due to its high susceptibility to modulation with $k = 2k_F$, while the accompanied lattice distortion costs energy. However, Peierls has shown analytically [45] that the electron system energy gain overcomes the cost of the lattice distortion energy at $T \rightarrow 0$ for noninteracting electrons. However when Coulomb interactions are taken into account, the 1D electron gas can stabilize in other ground states (see for example [46]), leading to superconductivity or spin density wave ground state.

The theoretical predictions received experimental confirmation roughly twenty years later when several groups of organic and inorganic metallic materials with a linear chain structure were discovered and examined. The first investigations include $K_2Pt(CN)_4Br_{0.3}$ (KCP) and tetracyanoquinodimethanide (TCNQ) salts [47], $NbSe_3$ [48, 49] and $TaSe_3$ [50, 51]. Since then, the CDW has been observed in an increasing number of other low dimensional conductors, including $K_{0.3}MoO_3$, $Rb_{0.3}MoO_3$ and $(TaSe_4)_2I$, which are all in the scope of this work. Interestingly, experimental fingerprints of CDWs were perhaps first observed as early as 1972, when Fogle et. al [52] measured the nonlinear electrical

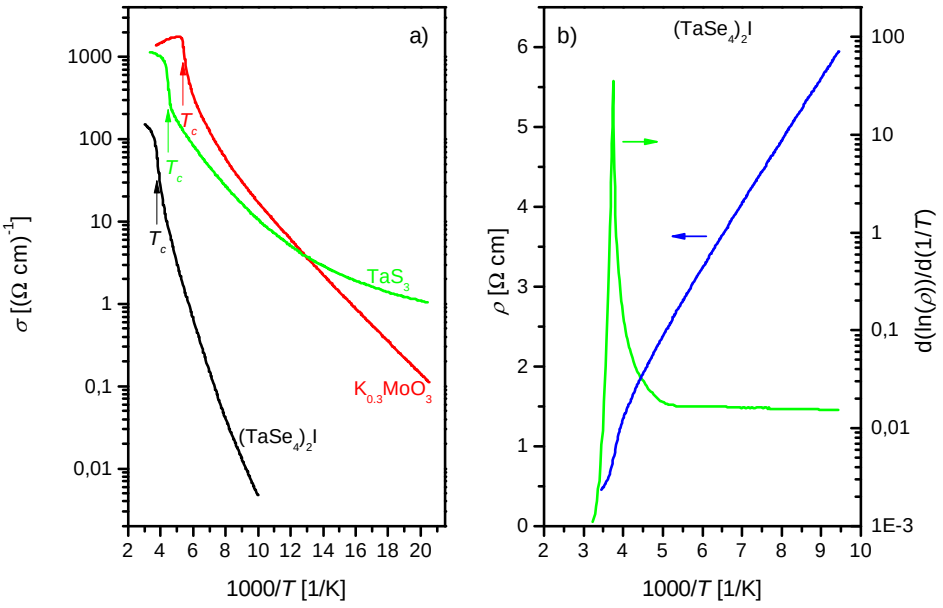

FIGURE 2.1: a) The dc conductivity of three different CDW materials as a function of temperature. The transition temperatures for all three compounds are marked with arrows. b) The dc resistivity and the derivative of the logarithm of resistivity that peaks at the transition temperature and has the value of the gap at small temperatures due to the temperature dependence of resistivity [60]. The data was extracted from [51].

conduction in $K_{0.3}MoO_3$.[1] However, these results remained fairly unnoticed until optical measurements gave undisputed evidence of the 1D properties in $K_{0.3}MoO_3$ as late as in 1981 [54].

The richness of physical manifestations in CDWs include the aforementioned metal to semiconductor transition [51] (see Figure 2.1) and the energy gap at the Fermi energy associated with it, strong renormalization of the phonon spectrum above T_C also known as the Kohn anomaly [55], lattice distortion [56], anomaly in the specific heat [57–59] and the collective excitations of the CDW (also known as the phase and the amplitude mode (AM)) [23]. It is therefore difficult to focus on just one physical phenomenon in CDW state without understanding at least the basic phenomenology of all of them. Some basic theoretical background for these phenomena will be given in this chapter but the reader is encouraged to consult References [60, 61] for a more detailed theory.

2.2 Ground State of a 1D Electron Gas

In this section we will show how the CDW transition can be understood theoretically if we consider the electrons in a strongly anisotropic material containing quasi-1D chains to behave as a one-dimensional (1D) electron gas [60]. One can intuitively consider

[1] The material has been known since 1964 [53].

such a physical problem since the phase space is reduced to one dimension so the Fermi surface consists of only two points $2k_F$ apart. At $T \to 0$ the system is very susceptible to perturbations with the wavevector $2k_F$. An analytical examination of the problem requires us to write down the dispersion relation for free electrons in 1D $\epsilon = \frac{\hbar^2 k^2}{2m_e}$. The Fermi energy is given by

$$\epsilon_F = \frac{\hbar^2 k_F^2}{2m_e}, \tag{2.1}$$

where m_e is the electron mass and k_F is the Fermi wavevector. The Fermi wavevector is given by

$$k_F = \frac{N_0 \pi}{2L} \Longrightarrow \epsilon_F = \frac{\hbar^2}{2m_e} \left(\frac{N_0 \pi}{2L} \right)^2, \tag{2.2}$$

where N_0 is the total number of electrons and L is the length of the 1D chain. The total number of orbitals $N(\epsilon)$ of energy $\leq \epsilon$ can be extracted from Equation 2.2 to obtain

$$N(\epsilon) = \frac{2L}{\pi\hbar}\sqrt{2m_e\epsilon}. \tag{2.3}$$

Using Equation 2.3 the density of states can be written as

$$n(\epsilon) \equiv \frac{\partial N}{\partial \epsilon} = \frac{L\sqrt{2m_e}}{\pi\hbar}\frac{1}{\sqrt{\epsilon}} = \frac{N(\epsilon)}{2\epsilon}. \tag{2.4}$$

Having written down the basic relations for a 1D electron gas, the electron response to a time independent potential can also be determined

$$\phi(\vec{r}) = \int_q \phi(\vec{q}) e^{i\vec{q}\cdot\vec{r}} d\vec{q}, \tag{2.5}$$

where the induced charge is expressed through the relation

$$\rho^{ind}(\vec{q}) = \chi(\vec{q})\phi(\vec{q}). \tag{2.6}$$

$\chi(\vec{q})$ in the above equation is the so-called Lindhard response function. It is given in d dimensions [62, 63] as

$$\chi(\vec{q}) = \int \frac{d\vec{k}}{(2\pi)^d} \frac{f_k - f_{k+q}}{\epsilon_k - \epsilon_{k+q}}, \tag{2.7}$$

where $f_k = f(\epsilon_k)$ is the Fermi function

$$f(\epsilon) = \frac{1}{\exp\left(\frac{\epsilon-\mu}{k_B T}\right) + 1}. \tag{2.8}$$

Here k_B is the Boltzmann constant and μ is the chemical potential that is chosen for a particular problem in such a way that the total number of particles in the system comes out correctly. At absolute zero $\mu = \epsilon_F$ which is the value which will be used in the following calculations.

Calculating the response in 1D at $T = 0$ is straightforward since it can be assumed that Fermi function is a step function which simplifies Equation 2.7 to

$$\chi^{1D}(q) = -\frac{m}{\pi\hbar^2} \int_{k_F-q}^{k_F} \frac{dk}{2qk + q^2} = -\frac{m}{\pi\hbar^2} \frac{1}{q} \ln\left|\frac{q + 2k_F}{q - 2k_F}\right|. \tag{2.9}$$

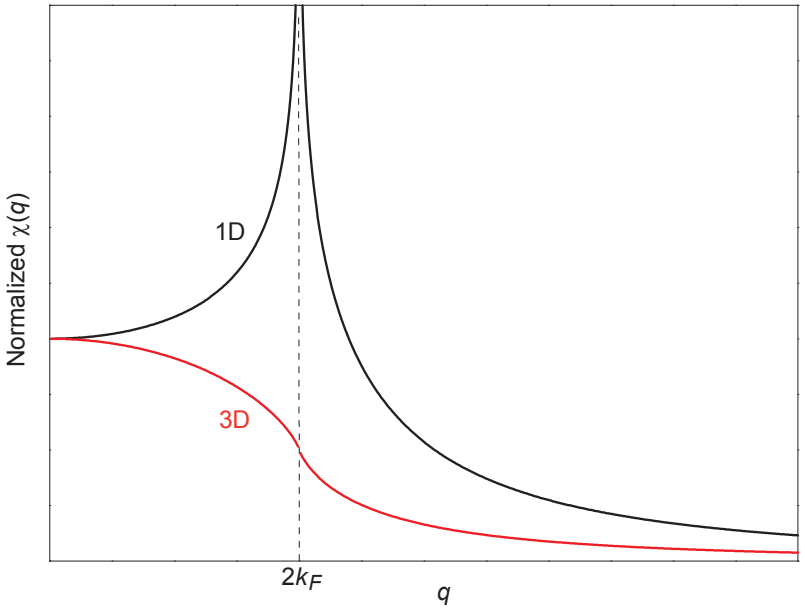

FIGURE 2.2: The Lindhard response function for a 1D metal at zero temperature. The 3D response function is plotted for comparison.

The 1D response function is displayed in Figure 2.2 and one can see that its logarithmic dependence is divergent at $q = 2k_F$. This implies that at $T \to 0$ any perturbation with

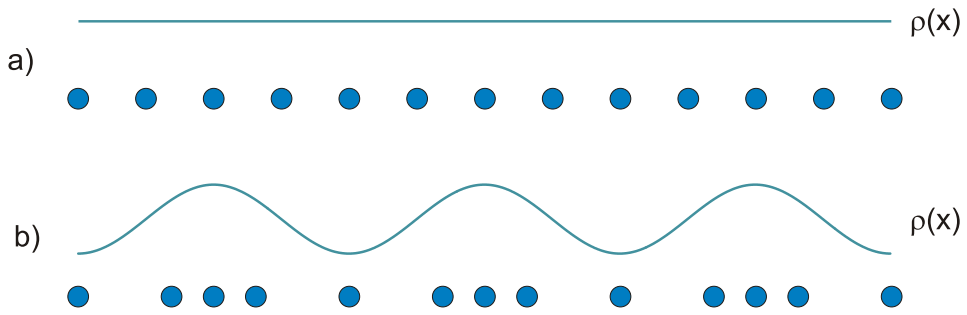

FIGURE 2.3: a) A schematic representation of a 1D chain above the transition temperature when it is in metallic state. The ions in the chain are spaced equidistantly and there is no modulation of the charge density $\rho(x)$. b) A schematic representation of a 1D chain below the transition temperature when it is in the CDW state. Both the ionic positions and the charge density are modulated with $k = 2k_F$.

wavevector $q = 2k_F$ leads to a redistribution of charge. Equation 2.6 tells us that the wavevector of the redistribution will be $q = 2k_F$; presenting a charge density modulation with $q = 2k_F$ (see Figure 2.3).

The result of Equation 2.7 can also be calculated for finite temperatures around $2k_F$ to show it still displays logarithmic dependence

$$\chi^{1D}(q) = -e^2 n(\epsilon_F) \ln\left(\frac{1.14\epsilon_0}{k_B T}\right), \tag{2.10}$$

where ϵ_0 is an arbitrarily chosen cut-off energy that is usually taken to be equal to the Fermi energy. All these results show that a 1D electron gas will be unstable against charge density modulation $T \to 0$.

2.3 CDW: The Mean Field Theory

A 1D free electron gas coupled to the underlying 1D ion lattice can be treated using the mean field approach (see section 3.1 in Ref. [60]). Fröhlich [44] and Peierls [45] have used the mean field approximations and weak electron-phonon coupling limit to describe such a system with a so-called Fröhlich Hamiltonian:

$$H = \underbrace{\sum_k \epsilon_k a_k^\dagger a_k}_{\text{electron } H} + \underbrace{\sum_k \hbar\omega_q b_q^\dagger b_q}_{\text{phonon } H} + \underbrace{\sum_{k,q} g|q| a_{k+q}^\dagger a_k (b_{-q}^\dagger + b_q)}_{\text{e-ph coupling } H}. \tag{2.11}$$

The first term is the Hamiltonian for free electrons where $a_k^\dagger$ and a_k are the creation and annihilation operators for the electron states with energy $\epsilon_k = \frac{\hbar^2 k^2}{2m}$. The second term is the lattice Hamiltonian where $b_k^\dagger$ and b_k are the creation and annihilation operators for phonons characterized by the wavenumber q. Finally, the third term describes the electron-phonon coupling, where g is the coupling constant. By solving the equation of motion of the normal coordinates Q for this Hamiltonian, the renormalized phonon frequency is obtained

$$\omega_{ren,q}^2 = \omega_q^2 + \frac{2g^2\omega_q}{M\hbar}\chi(q,T) \xrightarrow{q\to 2k_F} \omega_{2k_F}^2 \frac{T - T_{CDW}^{MF}}{T_{CDW}^{MF}}. \tag{2.12}$$

Here M is the ionic mass. The renormalized phonon frequency goes to zero with decreasing temperature and this behavior defines the mean field transition temperature T_{CDW}^{MF} as the point where the renormalized frequency reaches zero. It also indicates a "frozen-in" lattice distortion. This means a macroscipically occupied phonon mode with nonvanishing expectation values $\langle b_{2k_F} \rangle = \langle b_{-2k_F}^\dagger \rangle$. Using Equations 2.10 and 2.12 the mean field transition temperature T_{CDW}^{MF} can therefore be written as

$$k_B T_{CDW}^{MF} = 1.14\epsilon_0 e^{-1/\lambda}, \tag{2.13}$$

where the dimensionless electron phonon coupling constant λ is

$$\lambda = \frac{g^2 n(\epsilon_F)}{\hbar\omega_{2k_F}}. \tag{2.14}$$

Equation 2.13 is a BCS-type relation [64] that provides an intuitive result that stronger electron-phonon coupling results in a higher transition temperature. This equation also hints that the equations describing the CDW state are similar to the ones describing superconductors. Ginzburg and Landau asserted that the superconducting state can be characterized by a *complex order parameter* $\psi(\vec{r})$ [65], which vanishes above T_c and whose magnitude measures the degree of superconducting order at position $\vec{r}$ below T_c.[2] The CDW order parameter is defined in a similar fashion. Since the CDW order is "measured" by the lattice distortion, the mean amplitude of the "frozen-in" phonon mode defines the order parameter. By definition, a "frozen-in" phonon exists when the mean value of the distortion $u(x) \propto \sum_q (b_q + b_{-q}^\dagger)e^{iqx}$ is not zero for a given q. Also, it has already been shown that the lattice distortion wavevector is equal to $2k_F$, therefore the order parameter is defined as

[2] The situation in a Heisenberg ferromagnet is a very good analogy. The order parameter there can be viewed as the mean value of the local spin $\vec{s}(\vec{r})$. It gives the local value of spontaneous magnetization below T_c and it vanishes above T_c.

$$|\Delta|e^{i\phi} = g\left(\left\langle b_{2k_F}\right\rangle + \left\langle b^{\dagger}_{-2k_F}\right\rangle\right), \tag{2.15}$$

where the average number of phonons that form the lattice distortion is counted. Using this mean field equation, Equations 2.13 and 2.14 can be rewritten as

$$2\Delta = 3.52 k_B T^{MF}_{CDW} \tag{2.16}$$

$$\frac{1}{\lambda} = \int_0^{\epsilon_0} \tanh\left(\frac{\epsilon_k}{2k_BT}\right) \frac{d\epsilon_k}{\sqrt{\epsilon_k^2 + |\Delta|^2}}. \tag{2.17}$$

Equation 2.16 gives us the well known BCS relation between the zero temperature gap and the transition temperature, whereas the temperature dependence of the CDW gap in Equation 2.17 is the same as the temperature dependence of the superconducting gap within the BCS theory framework (see Figure 2.4). As a result, the formulas worked out for superconductors can be applied to describe temperature dependencies of various quantities in the charge density wave state, including $|\Delta|$ and the CDW condensate density $f(T)$.[3] At low temperatures (when $\Delta \gg k_BT$) the temperature dependence of Δ is weak and can be approximated by [66]

$$\Delta = \Delta_0 - \sqrt{2\pi T\Delta_0}\left(1 - \frac{T}{8\Delta_0}\right)^{\frac{1}{2}}. \tag{2.18}$$

Close to T^{MF}_{CDW} the gap approaches zero and Equation 2.13 reduces to square root dependence [66]

$$\frac{\Delta(T)}{\Delta(T=0)} = 1.74\left(1 - \frac{T}{T^{MF}_{CDW}}\right)^{\frac{1}{2}}. \tag{2.19}$$

However there is one crucial difference between the equations describing the CDW materials and superconductors; that is the relevant cutoff energy ϵ_0 which was defined in Equation 2.13. In superconductors, retardation (relaxation) effects of the lattice need to be taken into account so the cutoff frequency is taken to be of the order of the Debye frequency ω_D. On the other hand, the CDW energy gap develops in response to a static distortion of the underlying lattice so the relaxation effects do not come into

[3] It has to be pointed out that this is only true in the weak interchain coupling limit since in the strong coupling limit the 1D chain approximation is wrong. A material's anisotropy is a good measure for the coupling strength.

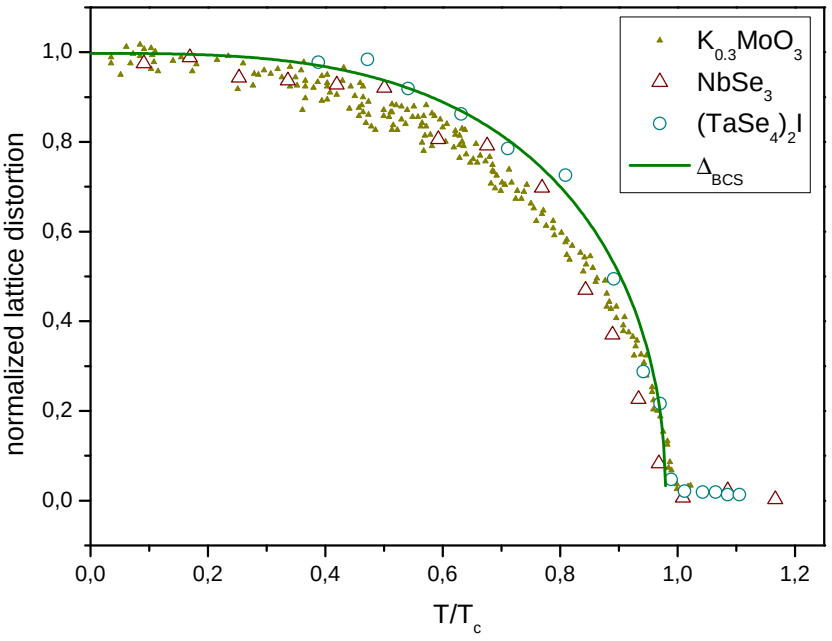

FIGURE 2.4: Temperature dependence of superlattice reflection intensities in $NbSe_3$ (data obtained from [67]), in $(TaSe_4)_2I$ (data obtained from [68]) and in $K_{0.3}MoO_3$ (data obtained from [69]). The data reveal relatively good agreement with the temperature dependence of the amplitude of the order parameter (gap) calculated within the frameworks of the BCS theory.

play. Therefore the electron-phonon interaction influences the whole electron spectrum, thus making the relevant cutoff energy equal to the Fermi energy ϵ_0. Since there is a substantial difference between the two energies, the transition temperatures in CDW materials tend to be much higher than in superconductors.

The energy gain due to the formation of a CDW can also be written in terms of Δ, the order parameter, and can be obtained after some algebra from the Hamiltonian defined in Equation 2.11 (see Chapter 3 in Ref. [60] for the full derivation) The energy change consists of the change in electronic energy E_{el} and the change in lattice energy E_{latt}

$$E_{total} = n(\epsilon_F)\Delta^2 \left(\underbrace{-\frac{1}{2} - \log\frac{2\epsilon_F}{\Delta}}_{E_{el}} + \underbrace{\frac{1}{2\lambda}}_{E_{latt}} \right). \tag{2.20}$$

Equation 2.20 can be minimized to obtain the amplitude of the order parameter

$$\Delta = 2\epsilon_F \exp(-1/\lambda). \tag{2.21}$$

The final result is the so called condensation energy that measures the actual energy gain of a material that undergoes a metal to CDW transition and is written as[4]

$$E_{con} = E_{normal} - E_{CDW} = \frac{n(\epsilon_F)}{2}\Delta^2. \tag{2.22}$$

2.4 Fluctuation and Interchain Coupling Effects

The mean field solution of the 1D model leads to a finite transition temperature T^{MF} where the "frozen-in" lattice distortion develops. However, one must be aware that the long-range nature of this solution is only an artifact of the mean field approximation because the fluctuations of the order parameter have been neglected. Actually, the fluctuations become important in strongly anisotropic materials at low temperatures because of the reduction of the phase space. In fact, a strictly 1D system with short range interactions does not develop long range order at finite temperatures at all [70]. The argument is virtually the same as in a Heisenberg antiferromagnet. A gapless collective excitation prevents long range order so only short range correlations occur at low temperatures. In a CDW system, the gapless excitation is the so called phase mode or phason (see Section 2.5).

None of the real materials are strictly one dimensional, of course. One must therefore account for the interactions between the neighboring chains (e.g. the Coulomb forces) and also one-electron inter-chain tunneling. These effects cause long-range 3D ordering below a finite temperature T_{3D}. If the inter-chain coupling is weak then T_{3D} is significantly smaller than T^{MF} as is the case in most CDW materials. For example, the single particle gap in $K_{0.3}MoO_3$ is $\Delta \approx 700$ K ≈ 60 meV so Equation 2.16 yields $T^{MF} = 330$ K. This is well above the phase transition temperature $T_{3D} = 183$ K. The temperature region between T_{3D} and T^{MF} is characterized by 1D fluctuations that cross over to two- or three-dimensional fluctuations as T_{3D} is approached from above. The Coulomb interactions seem to be dominant since the neighboring chains tend to align themselves with phase difference π (see Figure 2.5).

In Figure 2.5 we plot the schematic temperature evolution of a system of coupled chains that is in a metallic state above T^{MF}. At T^{MF} correlations build up along the chains with the correlation length $\xi_{1D} \propto 1/T$ [60][5] (see Figure 2.6). The interchain coupling

[4]Note the positive sign that means that the CDW ground state has, in 1D, lower energy than the normal state.

[5]$1/T$ temperature dependence is a good approximation when only phase fluctuations need to be considered. At high temperatures, the correlation length is given by $\xi_{||} = \frac{[7\zeta(3)]^{\frac{1}{2}} v_F}{4\pi k_B T}$ [71], where $\zeta(3)$ is the third order zeta function.

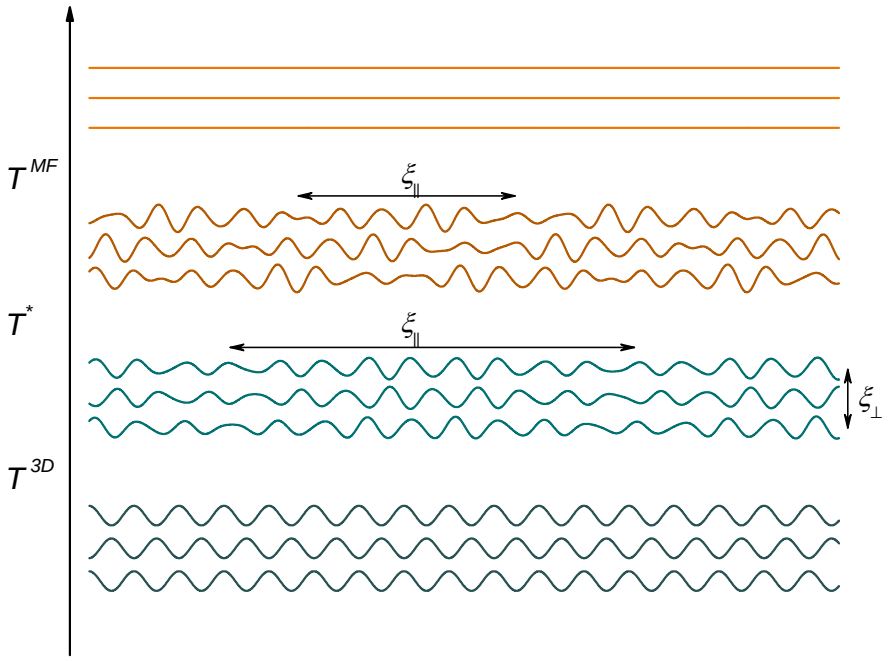

FIGURE 2.5: The temperature dependence of fluctuations in a CDW material from the metallic state to the 3D ordered state.

becomes significant upon further cooling and the perpendicular correlation length $\xi_\perp$ grows equal to the interchain distance $d_\perp$ as the system is cooled down to T^*. This is where the fluctuations cease to be 1D but rather 3D in nature (however this does not mean that there is long-range order). Since major part of coupling stems from Coulomb force, the neighboring chains tend to align with a phase difference of π. As the temperature is further decreased, both correlation lengths $\xi_{||}$ and $\xi_\perp$ diverge as $\propto 1/(T - T_{3D})^{\frac{1}{2}}$ [60] (see Figure 2.6) and the system undergoes a second-order phase transition to the 3D CDW state below T_{3D}.

If any additional fluctuations are neglected, the behavior of the phase transition is mean-field like. On the other hand, the short coherence lengths of CDW materials suggest that the critical Ginzburg-Landau fluctuations may be important in the vicinity of T_{3D}. The temperature region near the transition temperature where these fluctuations are important is given by [65]

$$\Delta T = \frac{k_B^2 T_{3D}}{\Delta C(\xi_{0||}\xi_{0\perp})^2}. \tag{2.23}$$

$\xi_{0||}$ and $\xi_{0\perp}$ are both zero temperature coherence lengths and ΔC is the measured specific heat anomaly at T_{3D}. Within ΔT near the transition temperature ($\Delta T \approx 20K$ in $K_{0.3}MoO_3$ for example) various thermodynamic quantities have a distinctly different temperature dependence than those given by the mean field approximation.

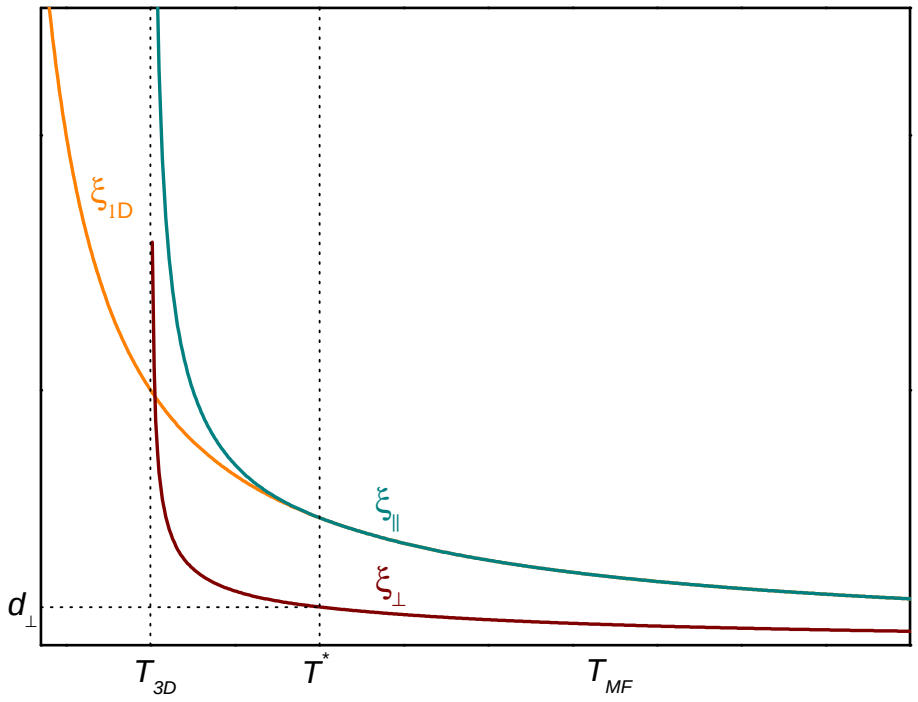

FIGURE 2.6: The temperature dependence of correlation lengths parallel ($\xi_{||}$) and perpendicular ($\xi_{\perp}$) to the chains. T_{MF} is the mean field transition temperature. The crossover from 1D to 3D fluctuations occurs at T^* when the correlation length perpendicular to the chains becomes equal to the distance between the chains $d_{\perp}$ (also indicated on the graph). At T_{3D} the material undergoes a second order phase transition where long range 3D order is established.

It has to be pointed out that in most materials the isotropic interchain coupling used in the above calculations is an oversimplification since the interchain coupling is usually different in the two crystallographic directions perpendicular to the chain direction. Consequently these theoretical predictions do not merit a more detailed comparison with experimental data. Nevertheless, the experiments confirm the gross picture presented above so it is a good enough approximation in many cases.

2.5 Collective excitations

The existence of a complex order parameter (Equation 2.15) in CDW materials hints that both phase and amplitude excitations of the order parameter can occur (beside from single particle excitations). Intuitively we can guess that the phase excitation at $q = 0$ is the translational motion of the CDW condensate, while the amplitude mode is the breathing mode of the charge density modulation.

A more rigorous approach within the time-dependend Ginzburg-Landau theory involves defining the free energy F of a one-dimensional chain in terms of the amplitude of the complex order parameter Δ

$$F = F(0) + n(\epsilon_F) \int dx \left[a|\Delta|^2 + b|\Delta|^4 + c \left| \frac{d\Delta}{dx} \right|^2 + d \left| \frac{d\Delta}{dt} \right|^2 \right], \tag{2.24}$$

where a, b, c and d are time independent constants that can be derived in terms of the microscopic description of the CDW ground state [60]. The first two terms describe the potential energy while the third and fourth terms in the free energy describe the energy associated with spatial variation and the kinetic energy due to temporal fluctuations, respectively. Since small fluctuations of the amplitude of the order parameter $\delta(x,t)$ and fluctuations of the phase $\phi(x,t)$ can be assumed, the order parameter can be written as

$$\Delta(x,t) = (|\Delta| + \delta(x,t))\, e^{\imath\phi(x,t)}. \tag{2.25}$$

Equations 2.24 and 2.24 can be used to write the Lagrangian and solve the equations of motion. A short calculation provides wave-like solutions where the dispersion relations for the amplitude and phase are given by (see Figure 2.7)

$$\omega_\phi = \left(\frac{c}{d}\right)^{\frac{1}{2}} q \tag{2.26}$$

and

$$\omega_A = \left(-\frac{2a}{d} + \frac{c}{d} q^2 \right)^{\frac{1}{2}}. \tag{2.27}$$

Since the phase excitation corresponds to translational motion of the CDW condensate in the $q = 0$ limit, it is not surprising that the phason frequency is zero in that limit. This is because translational motion in an incommensurable CDW material does not change the condensation energy of the condensate since the amplitude of the complex order parameter remains the same. However, commensurability effects and Coulomb interactions modify the temperature dependence and the dispersion relation of the phase mode (see Ref. [60]). Moreover, since CDW is pinned to impurities that act as a restoring force opposing translational motion, phase frequency always remains finite even at $q \to 0$.

The Coulomb interactions cause very different behavior of the phase mode in the low and high temperature limits, where both limits are defined by the number of thermally excited quasiparticles. At zero temperature, there are no thermally excited quasiparticles so long-range Coulomb interactions cause a gap in the phase mode spectrum for longitudinal excitations [72] and the longitudinal phase mode is optic-like [71, 73, 74]. This is simply because any CDW displacement relative to the underlying lattice causes

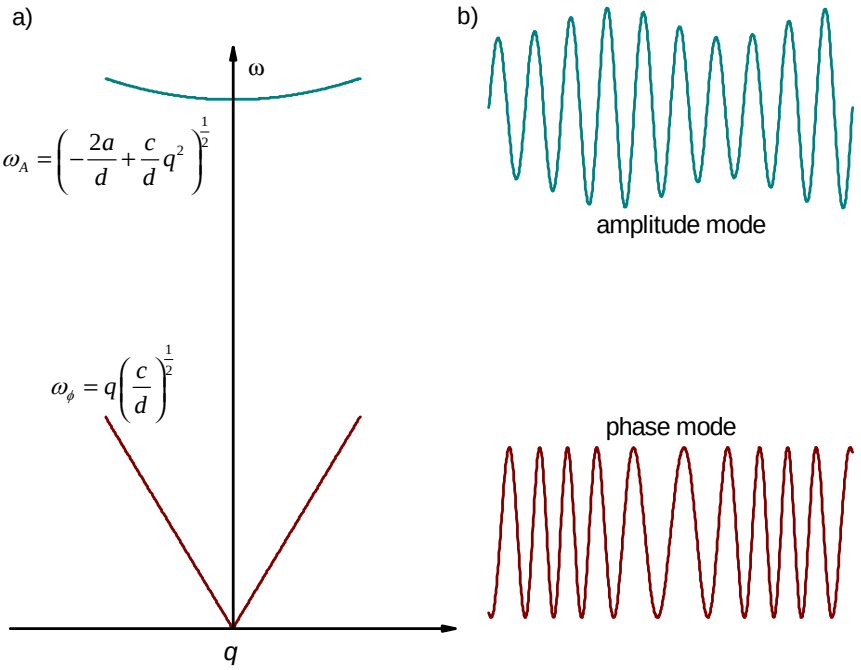

FIGURE 2.7: a) The dispersion relation of the phase and amplitude mode near $q = 0$. b) The phase and amplitude excitations with a finite q.

an electric field force opposing the displacement. Therefore the CDW moves only when the external field causing the displacement is high enough to overcome the opposing force and move the CDW as a rigid entity. At higher temperatures, the number of quasiparticles increases and they start screening the long range Coulomb interactions. When a finite external electric field is then applied, any longitudinal movement of the CDW is compensated by the quasiparticle current. This is why the CDW does not feel an opposing electric force and why the phonon mode dispersion relation is acoustic [73] in this limit.

On the other hand, the frequency of oscillations of the amplitude mode remains finite for all q. At $q = 0$ the frequency would correspond to the amplitude of the gap if the breathing of the CDW amplitude was not inherently coupled with ionic movement (this is the case for spin density waves where the amplitude mode frequency corresponds to the amplitude of the gap). This is because changing the amplitude of the gap corresponds to exciting electrons from the CDW ground state across the gap. The electron-phonon coupling leads to an amplitude mode frequency much smaller than $\Delta/\hbar$. One can also evaluate the amplitude mode frequency by estimating how much the amplitude excitation changes the condensation energy. The estimation yields

$$\omega_A^2(q = 0) = \lambda^{\frac{1}{2}}\omega_{2k_F}, \tag{2.28}$$

where ω_{2k_F} is the unrenormalized phonon frequency at $q = 2k_F$. Usually $\omega_{2k_F} \ll \Delta$ and $\lambda < 1$ so the amplitude mode frequency is well below the continuum of single particle excitations. In most CDW materials $\sqrt{\lambda} \approx 1$ so the unrenormalized phonon frequency at $q = 2k_F$ gives a good first estimate for the amplitude mode frequency even if the electron-phonon coupling is not known. The frequency of the temperature dependence of the amplitude mode can be calculated within the Ginzburg-Landau theory [65] and was found to drop to zero at the Peierls transition temperature with the following temperature dependence close to the transition temperature T_{CDW} [60]

$$\omega_A \approx \frac{1.55}{4} \lambda^{\frac{1}{2}} \omega_{2k_F} \left(1 - \frac{T}{T_{CDW}}\right)^{\frac{1}{4}}. \tag{2.29}$$

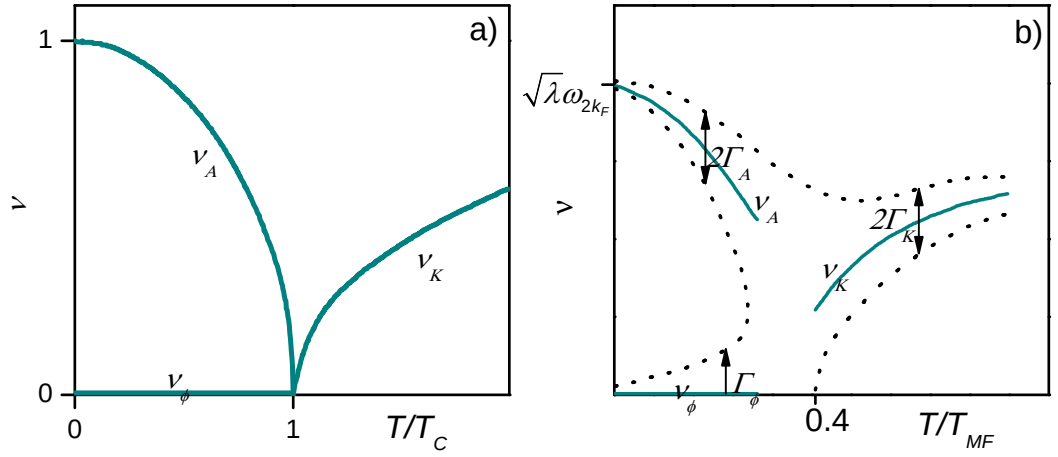

FIGURE 2.8: a) The mean-field temperature dependency of the frequency of the phase mode ν_ϕ, of the amplitude mode ν_A and of the Kohn anomaly ν_K for the $q = 2k_F$ wavevector. b) The schematic representation of the collective mode frequencies and their damping (full width at half maximum of the calculated peaks) numerically calculated for a Peierls chain in Ref. [75] with an experimental confirmation in Ref. [76].

Experimentally, the collective excitations can be measured using various techniques. Both the phase and amplitude mode dispersion relations have been measured using inelastic neutron scattering [76–79]. On the other hand, different optical methods must be used for the amplitude and phase modes. Since oscillations of the phase involve displacements of electronic charge with respect to ionic positions, this mode is optically active and has been measured by means of far-infrared spectroscopy [80, 81]. However, no charge displacement occurs for the amplitude mode so it is Raman active [54, 82]. Finally, CDW sliding, a special case of phase excitation, has been directly observed by NMR [83, 84].

The Newtonian dynamics of a one-dimensional Peierls chain has also been calculated in a wide temperature range using Monte Carlo - molecular dynamics simulations [75]. The results of that calculation are shown in Figure 2.8 b. The solution is defined below

the mean field temperature T_{MF}. When the temperature decreases, the frequency of the Kohn anomaly ν_K decreases while its damping increases which leads to an overdamped response near $0.4\,T_{MF}$. Approximately at $0.3\,T_{MF}$ the amplitude mode emerges at a finite frequency ν_A from the overdamped response. As the temperature decreases, the amplitude mode separates from the phase mode both due to the increase of the amplitude mode frequency and due to the decrease of damping of both modes. At $T = 0$ the amplitude mode frequency is fiven by the mean field theory (see Equation 2.28).

2.6 Strong electron-phonon coupling limit

Experimentally, the ratio between the value of the electronic gap and the transition temperature to a 3D CDW state T_{CDW} is found to be much larger than predicted by Equation 2.16. On one hand, this is usually ascribed to the renormalization of the transition temperature due to the weak interchain interactions and the large-amplitude 1D fluctuations above T_{CDW} [71]. On the other hand, Aubry et al. [85, 86] have proposed an alternative description in the context of strong-coupling theory. The ground state of an interacting electron-phonon system can not be perturbatively calculated from the metallic state when the electron-phonon coupling κ is above a critical value κ_c. This regime is characterized by pairwise localized electrons – bipolarons. This regime is very different as is the case in high T_c superconductors [87, 88], where bipolarons are isolated defects with negligible overlapping. In the case described in Ref. [86], bipolarons overlap and form a dense ensemble. In the $T \to 0$ limit, the bipolarons form an ordered state. Depending on the bipolaron kinetics, the ground state can be a commensurate structure, an incommensurate structure or even a bipolaron glass state. In the $\kappa \to \infty$ limit, bipolarons form a charge density wave. The normalized electronic eigenstate of the bipolaron is given by

$$\Psi(x) = \frac{\kappa}{2\sqrt{2}} \frac{1}{\cosh \frac{\kappa^2 x}{4}}. \tag{2.30}$$

The parameter κ is defined as

$$\kappa = \lambda \sqrt{\frac{2}{tM\omega_0^2}}, \tag{2.31}$$

where ω_0 and M are the constant frequencies and masses of identical oscillators located at each lattice site and t is the electronic exchange coupling between neighbouring sites.

In this picture, the Peierls gap $2\Delta(T = 0)$ corresponds to the bipolaron formation energy . The activated nature of the electrical conductivity in the whole temperature range is explained in terms of bipolaron hopping between sites. The Peierls transition temperature T_c^{3D} corresponds to the ordering temperature of the bipolaronic fluid. The bipolaron interaction energy determines the magnitude of $k_B T_c^{3D}$ which is why $k_B T_c^{3D}$ can be assumed to be much lower than the bipolaron formation energy $2\Delta(T = 0)$.

Chapter 3

Femtosecond pump-probe spectroscopy

In this chapter we describe the experimental technique, the light sources used and the means of detection of small signals. We also describe the analysis of the time resolved optical data used in the following chapters and discuss the heating effects that need to be taken into consideration when interpreting the data.

3.1 Femtosecond time-resolved optical spectroscopy: Experimental.

Time resolved optical spectroscopy involves measurement of a transient change of the optical transmission T or reflectivity R of a material under investigation on a femtosecond time scale. The technique is also referred to as the *pump-probe technique*. As the name suggests, the investigated material is excited by the first ultrashort pulse (*pump*) while the appropriately delayed second ultrashort pulse monitors the response in the material. The delay between the two pulses is achieved by translating a retroreflector that is placed in the path of one of the two beams (see Figure 3.1). The commercially available motorized translation stages that move the retroreflector have submicrometer steps so time delays as small as one femtosecond can be achieved between the two pulses. Therefore the time resolution of a pump-probe experiment is determined by the length of the laser pulse which usually ranges from 10 fs – 200 fs.

We can achieve a wide range of excitation intensities where the *pump* pulse energies in our setup span from 5 pJ – 5 μJ. The *pump* beam is usually focused on a $\sim$ 80 μm diameter so the fluences range from 100 nJ/cm^2 – 100 mJ/cm^2. The criterion for small

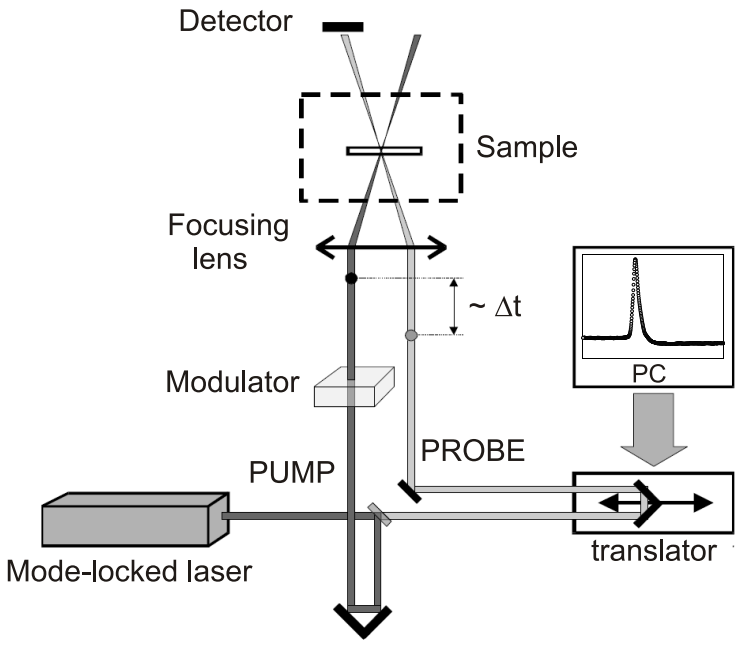

FIGURE 3.1: A typical pump-probe transmission setup. The only difference when measuring the photoinduced reflectivity is that the *probe* beam is reflected off the sample.

perturbation in a CDW material is to compare the number of photoexcited carriers (roughly the absorbed energy per unit cell divided by the gap energy) with the number of electrons in the CDW state ($\sim 2N(0)\Delta$, where 2Δ is the gap and $N(0)$ is the density of states at the Fermi energy). In this *small perturbation* regime one expects linear relations between the density of photoexcited quasiparticles Δn_{qp} and the measured change of reflectivity ΔR. This is a general assumption for most materials because small changes in reflectivity can be written as $\Delta R = \frac{\partial R}{\partial \sigma_1}\Delta\sigma_1 + \frac{\partial R}{\partial \sigma_2}\Delta\sigma_2$ whereas small changes in both σ_1 and σ_2 are linearly proportional to small changes in the number of quasiparticles Δn_{qp}. Therefore a linear relation should also be expected between ΔR and Δn_{qp}.

The *probe* beam, which is usually at the same wavelength as the *pump* beam[1] is usually significantly attenuated, typically by a factor 100 in comparison to the *pump* beam. This means that the additional photoexcitation by the *probe* beam can usually be neglected.

[1]The wavelengths of the two beams are not necessarily the same however they were the same in the experiments described in this work.

3.1.1 Light Sources

Since the essential component of any femtosecond time-resolved optical system is a stable source of femtosecond laser pulses, the basic information about the femtosecond lasers used in our experiments will be presented in this section. However the details are beyond the scope of this work and can be found elsewhere in the literature [89–92].

In the experiments described in this work two very similar laser systems were used. The first laser system (at the Jožef Stefan Institute) includes a mode-locked Ti-sapphire laser (Mira Seed laser oscillator by Coherent). It has a repetition rate of 88 MHz with energies of up to 10 nJ per pulse. It can be used as a light source for the pump-probe measurements or as a seed for a regenerative optical amplifier (RegA 9050 by Coherent). The regenerative amplifier has a variable repetition rate in the range of 9 kHz – 300 kHz at 6 μJ energy per pulse and 60 fs pulselength. The wavelength of these two lasers is $\approx$ 800 nm (1.55 eV) with $\approx$ 30 nm FWHM. The second laser system (at Universität Konstanz) is a newer version of the first one with a Micra oscillator and a RegA 9050 regenerative amplifier by Coherent. The parameters of the output of the two systems are very similar, however, being newer, the second laser system is more stable. The second laser system is also better in terms of pulselength since one can achieve 15 fs and 40 fs pulses with the Micra oscillator and Rega amplifier, respectively.

Stable mode locking in the oscillator is achieved by using the Kerr effect [89–92] in a Ti-Sapphire crystal [93]. The laser amplifier is a continuous wave (CW) pumped Ti-Sapphire regenerative amplifier with an acousto-optic modulator [94] used as a cavity dumper [95]. This way high repetition rate of amplified pulses can be reached (up to 300 kHz in our system).

3.1.1.1 Measuring Ultrafast Laser Pulses

Ultrafast laser pulses need to be characterized in the time and frequency domains. Since the pulses used in our experiments have a nearly Gaussian temporal profile with pulsewidth τ_p, the optical spectrum is well described by the optical peak wavelength λ and the bandwidth $\Delta\lambda$, defined as the full width at half maximum (FWHM).

$\Delta\lambda$ for sub-100 fs laser pulses is 10's of nm around the central wavelength of 800 nm and the spectrum can easily be measured with an optical spectrum analyzer that is usually based on a grating and a photodiode array.

We measured the pulselength using an autocorrelator. A schematic drawing of an autocorrelator is presented in Figure 3.2. In our experiments, the autocorrelator was a

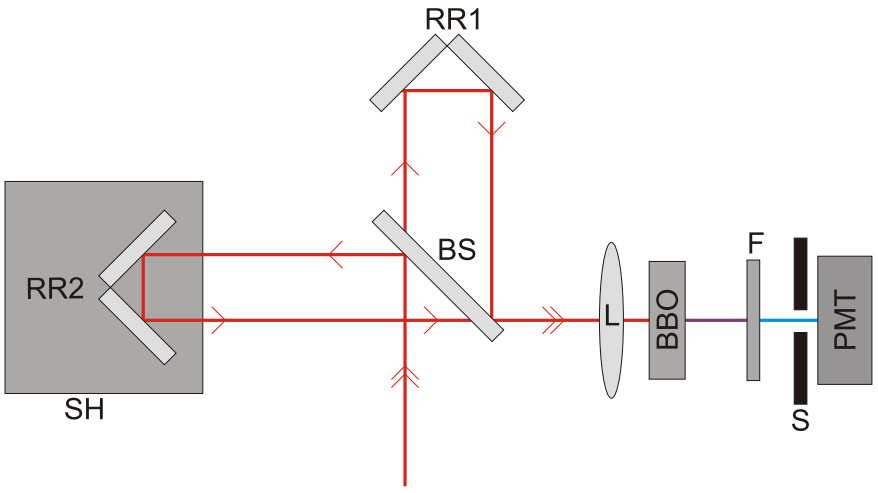

FIGURE 3.2: A schematic of the autocorrelator used to measure sub-100 fs pulses. The optical elements are RR1,RR2: retroreflectors; BS: 50/50 beamsplitter; L: focusing lens; BBO: BaB_2O_4 crystal used for second harmonic generation; F: filter used to eliminate the component at ω; S: an additional slit to block the light at 2ω generated individually by each of the two beams crossed in the BBO; PMT: photo-multiplier tube; SH: mechanical shaker.

Michelson interferometer with either a BaB_2O_4 (BBO) frequency doubling crystal or a photodiode that absorbs at $\omega \geq 2\omega_{1.5\,\mathrm{eV}}$. The incoming laser pulse at the center frequency ω is split in the two legs of the Michelson interferometer by a 50/50 beamsplitter. The two pulses are focused and overlapped on the BBO (or the photodiode) by using the lens. One of the pulses is delayed with respect to the other by changing the position of one of the retroreflectors mounted on a mechanical shaker. The BBO crystal must be oriented in a way to fulfill the phase matching condition [96] for second harmonic generation. When the time delay between the pulses is τ then the intensity of the of the created light at 2ω is proportional to the autocorrelation function of the pulse intensity $I_{2\omega}(\tau) \propto \int I_\omega(t+\tau) I_\omega(t) dt$. A filter is placed after the BBO to reject the light at frequency ω. An additional slit is also placed in front of the photomultiplier tube to reject any light at 2ω that was generated by individual beams.

By scanning the time delay τ with the mechanical shaker and measuring the current generated by the PMT (or the photodiode) using an oscilloscope one obtains the autocorrelation function. The FWHM of the autocorrelation function τ_{AC} is calibrated with the known change of length in one of the arms of the Michelson interferometer. To determine the actual pulselength, one needs to know the shape of the original pulse. We usually assume the Gaussian shape where $\tau_p = \tau_{AC}/\sqrt{2}$.

3.1.1.2 Laser beam characterization

Determining the energy per pulse and the size of the focused laser beam is very important when one performs quantitative measurements of the ultrafast optical response as a function of the fluence F. The energy per pulse is simply $\bar{P}/\nu$, where $\bar{P}$ is the average power of the laser beam and ν is the pulse repetition rate. The first of the two techniques[2] that we used to determine the diameter of the focused beam was placing a pinhole with a diameter $2r_{ph}$ in place of the sample. The average power of the laser beam is measured in front of the pinhole (P_{in}) and after the pinhole (P_{out}). Assuming that the beam has a Gaussian profile with power $P = P_0 \exp(-\frac{2r^2}{\rho^2})$, then we write the power before and after the pinhole as

$$P_{in} \propto \int_0^{r_{ph}} \exp\left(-\frac{2r^2}{\rho^2}\right) r dr = \frac{\rho^2}{4}\left(1 - \exp\left(-\frac{2r_{ph}^2}{\rho^2}\right)\right), \tag{3.1}$$

$$P_{out} \propto \int_0^{\infty} \exp\left(-\frac{2r^2}{\rho^2}\right) r dr = \frac{\rho^2}{4}. \tag{3.2}$$

The radius of the focused beam can then be expressed with the ratio P_{in}/P_{out} as

$$\rho = r_{ph}\sqrt{\frac{2}{\ln(1 - P_{in}/P_{out})}}. \tag{3.3}$$

The second technique that was used for measuring the dimension of the focused beam involved focusing the beam on a CCD sensor with known pixel size. The signal from the CCD was then fed to the computer where the diameter of the beam was calculated using the estimated spot size in pixels multiplied by pixel size.

To obtain the fluence F penetrating the sample we also accounted for the light reflected from the cryostat window (8%) and the part reflected from the sample.

3.1.2 Lock-in detection

The lock-in detection [97, 98] is a well established method of extracting the signal from the laser noise in a typical pump-probe experiment. The power spectrum of laser intensity noise is known to be of $1/\nu$, where ν is the frequency. The noise amplitude in audio range is quite high but is negligible at frequencies above 100 kHz.

[2]Both techniques yielded similar result.

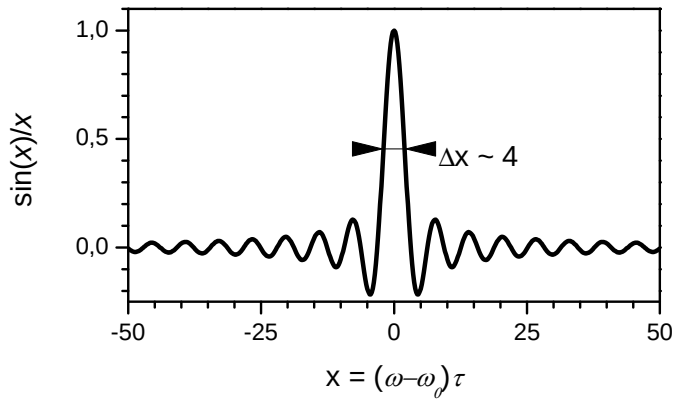

FIGURE 3.3: The frequency window of a lock-in amplifier. The width of the function Δx is also marked.

The noise is severely reduced by modulating the signal at a frequency where the noise is low and using a narrow band amplifier whose maximum gain frequency is equal to the modulation frequency. Such a narrow band amplifier is called a lock-in amplifier [99].

The lock-in detection works on a fairly simple principle [98]. The signal $S(\omega)$ and a reference signal $S_{ref}(\omega) = \cos(\omega_0 t - \varphi)$ are fed to the amplifier where they are multiplied and integrated over an arbitrarily chosen τ, $\int_0^\tau S(\omega)S_{ref}(\omega)dt$. The result is the input signal $S(\omega)$ in a narrow frequency window $\frac{\sin(\omega-\omega_0)\tau}{(\omega-\omega_0)\tau}$ whose width is determined by the integration time τ (see Figure 3.3).

In the experiments performed at Universität Konstanz the *pump* laser beam was modulated. The choice of modulation frequency depends on the laser repetition rate with the modulation frequency usually being ~ 2 orders of magnitude smaller than the laser repetition rate. Therefore when an oscillator laser system with typical repetition rate of 88 MHz is used (the separation between two adjacent pulses is 12.8 ns), the *pump* beam is modulated at modulation frequency $\omega_M \sim 200$ kHz using an acousto optic modulator [94]. On the other hand, when a regenerative amplifier with a typical repetition rate of 250 kHz is used, the modulation is achieved using a mechanical chopper operating at $\omega_M \sim 1$ kHz. The reflected *probe* beam is detected by means of a photodiode and the signal is sent to the lock-in amplifier which is phase locked to the frequency of the acousto optic modulator (or chopper). The lock-in amplifier discards all frequency components of the signal that are not close to ω_M and in phase with the modulation of the *pump* beam. Therefore it detects the modulation of the *probe* beam intensity that was caused by the *pump* pulse. By changing the integration time constant τ of the lock-in amplifier, one determines the width of the frequency window, consequently lowering the noise by integrating longer. With a typical integration constant of 1 s in our experiments, the effective frequency width of the amplification window is ~ 4 Hz. This enables us to

measure signals that are as small as 10^{-6}. It should also be noted that the signal is normalized with the DC signal amplitude on the photodiode in order to eliminate any signal artifacts due to long term fluctuation of the laser power.

The output of the lock-in amplifier consists of two signals where the first one is in phase with the modulation ω_M while the second one is out of phase ($\varphi = \pi/2$) with respect to the first one. The in-phase signal gives the time-resolved signal together with the photoinduced offset due to the long lived contribution to the photoinduced signal with the typical time-scale from nanoseconds to microseconds. The out-of-phase signal picks up all the dynamics that cannot follow the modulations with the dynamics corresponding to the modulation frequency (10 μs for 100 KHz modulation and 1 ms for 1 kHz modulation). Normally, the out-of-phase signal bears no relevant information because it describes very slow dynamics that can be measured by means of other experimental techniques.

3.1.3 Experimental setup

In this section we describe two different pump-probe setups. In the first experimental setup (at the Jožef Stefan Institute), schematically presented in Figure 3.4, we used a typical pump-probe setup where each point in time of the $\Delta R/R$ transient is acquired separately: when the translator moves into the computer controlled position, determining the time delay, the intensity of reflected light is measured on the photodiode and the signal is sent to the lock-in amplifier where the modulated part of the signal is amplified (see section 3.1.2). This is then repeated for every single point to obtain the transient signal.

The pump beam is modulated either by an acousto-optic modulator (AOM) or with a mechanical chopper. The modulation in both cases is 100%. When an AOM is used, the pulses significantly broaden since the AOM consists of a 5 cm highly dispersive flint glass. Therefore the pulses need to be pre-chirped by means of a folded two prism setup with negative group velocity dispersion in order to achieve the shortest pulsewidth at the sample. In order to achieve the same pulsewidth in the *probe* channel, a 5 cm long element of the same material as the AOM needs to be placed in the probe beam to account for the pre-chirp[3]. The beam is split into two using a beamsplitter that reflects x% of light in the *probe* channel, while the majority of light ($(1-x)$%) is transmitted and serves as *pump*. A $\lambda/2$ waveplate is places in each of the two beams, so that the polarization of each beam can be arbitrarily chosen. Both beams are focused on the

[3]When a mechanical chopper is used to modulate the *pump* beam, there is no additional pulse broadening so pre-chirping can be omitted. This option is realized in the other experimental setup shown in Figure 3.5.

same spot on the sample and the overlap is monitored using a CCD camera. The focal length of the two lenses is usually chosen so that the focused probe beam on the sample is roughly twice smaller than the focused pump beam. This ensures roughly the same pump-caused perturbation of the whole sample that is being probed. The intensity of the reflected (transmitted) *probe* is detected by a photodiode. In order to reject the scattered light from the pump beam, we place a pin-hole in front of the photodiode. Additionally, all the experiments are performed with the pump and probe polarizations crossed, so a polarizing cube (marked as A in Figure 3.4) rejects the scattered pump light. The retroreflector is mounted on a computer driven translator with a DC-motor with a 0.06 μm step. Therefore, the temporal resolution of our experiments is limited by the pulsewidth of the laser and is approximately 60 fs.

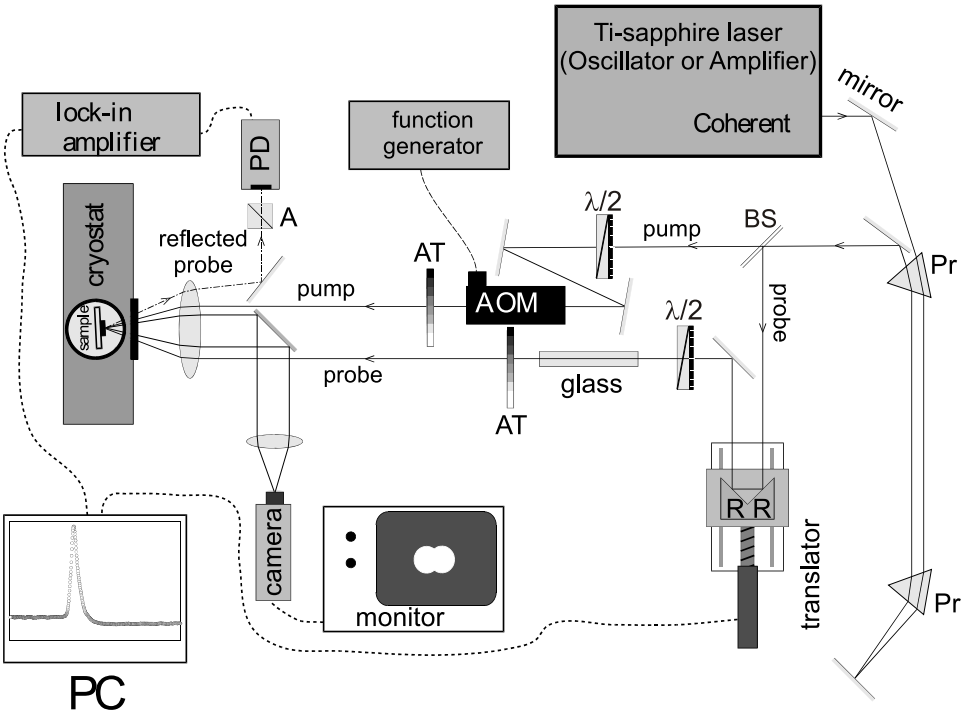

FIGURE 3.4: A schematic of the experimental setup in Ljubljana. Code: Pr: Brewster prism; BS: 4% reflecting glass plate; RR: retroreflector; AT: attenuator; A: analyzer (cube polarizer); PD: photodiode.

In the second experimental setup (used in the laboratory in Konstanz, Germany), shown schematically in Figure 3.5, the time delay between the pulses is achieved using a retroreflector mounted on a shaker that oscillates with $\sim$ 20 Hz – similarly as in the autocorrelator setup. The technique is also referred to as the *fast-scanning* technique. We used a commercially available translation shaker (ScanDelay 50 by APE) with an output signal that corresponded to the position of the translation stage. The shaker and *probe* photodiode signal are then recorded using an oscilloscope and combined to retrieve the

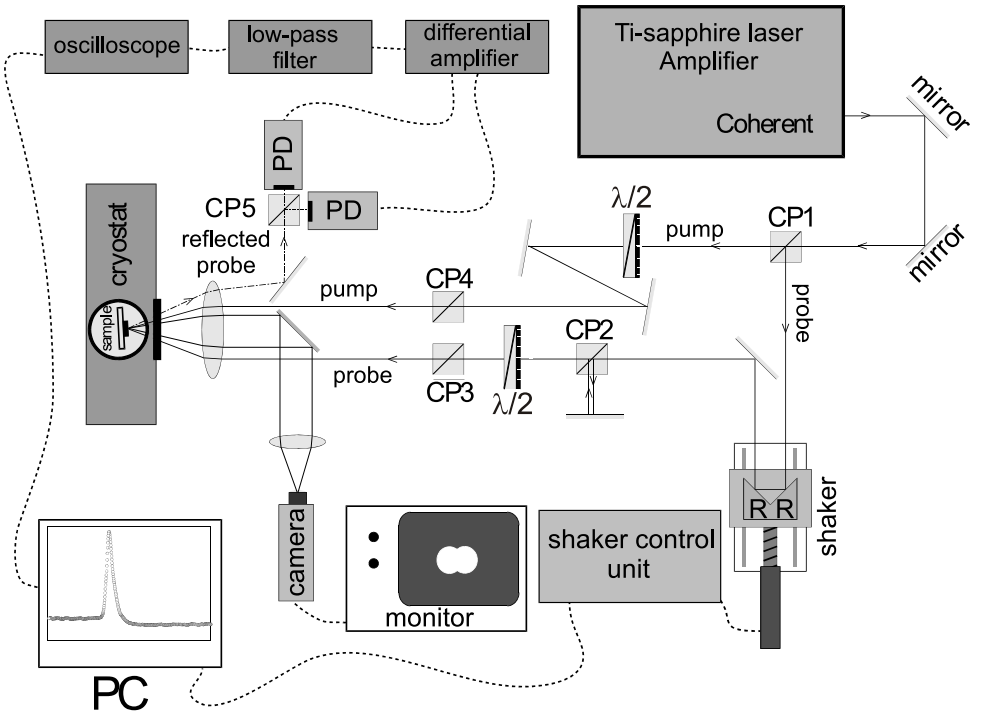

FIGURE 3.5: A schematic of the experimental setup in Konstanz. Code: CP1-CP5: cube polarizers; RR: retroreflector; PD: photodiode.

transient $\Delta R/R$ signal. The main advantage of this type of setup is the speed of data acquisition.

Figure 3.5 shows that the beam is split into the *pump* and *probe* channels (s and p polarization) using the cube polarizer CP1, that can be rotated to vary the intensity ratio of the two channels. The *probe* pulses are reflected to the reflector placed on the shaker that oscillates with ~ 20 Hz and a maximum displacement corresponding to a 50 ps delay. A $\lambda/2$ plate is placed in each of the two beams to control the polarizations of the two beams[4]. The cube polarizer CP2 is adjusted to split the *probe* beam into two cross-polarized and equally intense *probe* beams. The non-delayed *probe* pulses always reach the sample before the pump pulses so that channel is used as a reference that is subtracted from the delayed *probe* channel that monitors the photoinduced changes in reflectivity. The delayed *probe* channel must be reflected back to the polarizing cube PC2 at a 180° angle to ensure that the two channels are alligned and focused on the same spot on the sample. The cube polarizers WP3 and WP4 are used to control the intensities of the *pump* and *probe* channels. The beams are focused on the sample similarly as in the first experimental setup - so that the diameter of the focused *probe* is approximately twice smaller than the diameter of the focused *pump* beam. The *probe*

[4]The polarization of the beams reaching the sample is controlled by the $\lambda/2$ plates and the cube polarizers CP1-CP4.

reflected from the sample is split back into the delayed and undelayed *probe* pulses (s and p polarization) that are detected by the two photodiodes. The two signals are subtracted using a differential amplifier and sent to a low-pass filter that rejects the leftover high frequency contribution to the signal causes by individual laser pulses. The filtered signal containing the transient $\Delta R/R$ is then recorded by a PC controlled oscilloscope. The temporal resolution is again limited by the pulsewidth of the laser and is approximately 60 fs.

3.1.4 Heating Effects

Illumination of the sample by a laser beam introduces heating of the sample[5], which is an often discussed problem in literature [17, 100–104]. To understand the heating one needs to consider mechanisms on different timescales.

The photoexcitation of electron-hole pairs is followed by electron-electron thermalization taking place within femtoseconds. The electronic energy relaxation is determined by the electron-phonon relaxation processes, estimated to be tens of femtoseconds in metals [105]. Therefore on a 100 fs – 1 ps timescale after photoexcitation, the electrons and the lattice in the illuminated part of the sample can be considered to be at the same elevated temperature compared to the rest of the sample. Further relaxation is determined by the heat diffusion out of the illuminated spot that has a $1/\sqrt{t}$ decay [101]. However, the heat does not diffuse completely before the next pulse is absorbed which causes a temperature increase pile-up. The magnitude of this effect is the same as the heating of a CW laser with the same average power so we talk about *steady-state heating*. On the other hand, the time-dependent temperature increase caused by single pulses is called *transient heating*. The two effects will be treated separately below.

In both cases the laser beam is considered to be a TEM_{00} Gaussian beam travelling in the z direction and hitting the solid at $z = 0$. The center of the Gaussian beam is chosen as the origin of the other two coordinates for simplicity. In general, when attempting to find the solution to the problem of laser heating of solids without phase changes, one seeks solutions to the heat conduction equation, usually given as

$$\nabla \cdot \vec{j}(\vec{r}, t) + \rho_s c_s \frac{\partial T(\vec{r}, t)}{\partial t} = A(\vec{r}, t), \tag{3.4}$$

where $T(\vec{r}, t)$ is the temperature, $\vec{j}(\vec{r}, t)$ is the heat flow per unit area, ρ_s is the density and c_s is the specific heat of the solid. $A(\vec{r}, t)$ is the energy per unit volume and per unit time that is generated in the solid due to laser illumination. Equation 3.4 is a statement

[5] The increase of temperature refers to the increase of the lattice temperature.

of the law of conservation of energy in differential form. In order to solve it, one needs the relation between the heat flux $\vec{j}(\vec{r},t)$ and the temperature $T(\vec{r},t)$. This relation, also known as Fourier's law, is given by

$$\vec{j}(\vec{r},t) = -\underline{\kappa}\nabla T(\vec{r},t), \tag{3.5}$$

where $\underline{\kappa}$ is the thermal conductivity tensor. In these experiments the laser beam transverses approximately in the direction of one of the eigenvectors of the orthorhombic crystal so the heat conduction differential equation can be rewritten as

$$\rho_s c_s \frac{\partial T(\vec{r},t)}{\partial t} = \sum_i \kappa_i \frac{\partial^2 T(\vec{r},t)}{\partial x_i^2} + A(\vec{r},t) \tag{3.6}$$

where κ_i are the thermal conductivities in the a, b and c directions.

Since the temperature rise is of the order of several K or tens of K, the thermal radiation loss can be neglected. This simplifies the boundary condition to

$$\frac{\partial T(\vec{r},t)}{\partial z}_{z=0} = 0 \tag{3.7}$$

Since the thickness of the substrate or single crystal ($\sim$ mm) is typically much larger than the absorption length ($\sim$ 50 nm) the target can be considered to be a semi-infinite solid along the z axis. This yields the additional boundary condition

$$T(z \to \infty) = T_\infty, \tag{3.8}$$

where T_∞ is the temperature of the cold finger of the cryostat.

3.1.4.1 Steady State Heating

When calculating the increase of temperature due to a CW laser one looks for the equilibrium solution of Equation 3.6, therefore $\frac{\partial T(\vec{r},t)}{\partial t} = 0$. For a TEM_{00} laser mode, the generated energy per unit volume and per unit time is approximated by

$$A(x',y',z') = \frac{4(1-R)P_0\alpha}{\pi d^2} \exp\left[-\frac{2\left(x'^2+y'^2\right)}{d^2}\right] \exp[-\alpha z']. \tag{3.9}$$

P_0 is the average power of the *pump* beam[6], d is the diameter of the illuminated spot, α is the absorption coefficient and R is the reflectivity at the laser wavelength.

Equation 3.6 can be solved using the appropriate Green's function for the boundary condition 3.7. In this case the Green's function for the infinite solid [103] is taken and the method of images is applied to obtain

$$\begin{aligned} G\left(\vec{r'},\vec{r}\right) =& \frac{1}{4\pi\sqrt{\kappa_y\kappa_z(x-x')^2+\kappa_x\kappa_z(y-y')^2+\kappa_x\kappa_y(z-z')^2}} \\ &+\frac{1}{4\pi\sqrt{\kappa_y\kappa_z(x-x')^2+\kappa_x\kappa_z(y-y')^2+\kappa_x\kappa_y(z+z')^2}} \end{aligned} \tag{3.10}$$

Using Equations 3.9 and 3.10 the temperature rise can be calculated

$$\Delta T(x,y,z) = \int_0^\infty dz' \int_{-\infty}^{\infty} dx' \int_{-\infty}^{\infty} dy' G\left(\vec{r'},\vec{r}\right) A\left(\vec{r'}\right). \tag{3.11}$$

Due to the cylindrical geometry of the problem the variables should be changed to

$$\begin{aligned} r_x &= \frac{1}{P_0}\sqrt{\kappa_y\kappa_z}(x-x') = \rho\cos\phi, \\ r_y &= \frac{1}{P_0}\sqrt{\kappa_x\kappa_z}(y-y') = \rho\sin\phi, \\ r_{z\pm} &= \frac{1}{P_0}\sqrt{\kappa_x\kappa_y}(z\pm z') = \tilde{z}_\pm. \end{aligned} \tag{3.12}$$

The integral 3.11 can be simplified using the newly defined variables 3.12. The calculated temperature rise is

$$\begin{aligned} \Delta T(x,y,z) = \frac{\alpha(1-R)}{2\pi^2 d^2 k_x k_y k_z} \int_0^{2\pi} d\phi \int_0^\infty \rho\, d\rho\, e^{-\left(\frac{\sqrt{2}x}{d}-\frac{-\sqrt{2}\rho\cos\phi}{k_x d}\right)^2-\left(\frac{\sqrt{2}y}{d}-\frac{\sqrt{2}\rho\sin\phi}{k_y d}\right)^2} \\ \cdot\left(e^{\alpha z}\int_{k_z z}^{\infty}\frac{e^{-\frac{\alpha\tilde{z}}{k_z}}}{\sqrt{\rho^2+\tilde{z}^2}}d\tilde{z} + e^{-\alpha z}\int_{-\infty}^{k_z z}\frac{e^{\frac{\alpha\tilde{z}}{k_z}}}{\sqrt{\rho^2+\tilde{z}^2}}d\tilde{z}\right), \end{aligned} \tag{3.13}$$

[6]The average power of the probe beam is usually at least two orders of magnitude smaller than the average power of the *pump* beam so the *probe* contribution to heating can be neglected.

where $k_x = \frac{1}{P_0}\sqrt{\kappa_y \kappa_z}$, $k_y = \frac{1}{P_0}\sqrt{\kappa_x \kappa_z}$ and $k_z = \frac{1}{P_0}\sqrt{\kappa_x \kappa_y}$. For example, we can calculate the temperature increase of a laser illuminated blue bronze crystal when it is heated by a Gaussian beam with $d = 240$ μm and $P_0 = 1$ mW travelling along the [201] direction. The values for thermal conductivities are obtained from the literature [106] and are $\kappa_{[201]} = 0.54$ W/(Km), $\kappa_{[102]} = 2.7$ W/(Km) and $\kappa_{[010]} = 6.2$ W/(Km) at 160 K. The main directions are along the chains ([010]), perpendicular to the chains ([102]) and perpendicular to the planes ([201]) and they respectively correspond to $\hat{x}$, $\hat{y}$ and $\hat{z}$ directions in our coordinate system. We measured the two final parameters needed for this calculation and we obtained $R = 0.25$ and $\alpha = \frac{1}{85}$ nm^{-1}. The temperature increase at the center of the beam using the above parameters in Equation 3.13 is $\Delta T \approx 1K$. The lateral profile of the temperature increase is plotted in Figure 3.6.

It should also be mentioned that the modeling is based on the assumption that there is a good thermal contact between the sample and the cold finger of the cryostat. In our experiments, the samples were attached on the cold finger made of copper using G.E. varnish (Oxford Instruments) - known for its high thermal conductivity at low temperatures. Since the materials in the focus of our studies also have well defined transition temperatures with sharp features in the ultrafast signal, we were always able to estimate the heating which leads us to believe that the thermal contacts were good in all cases.

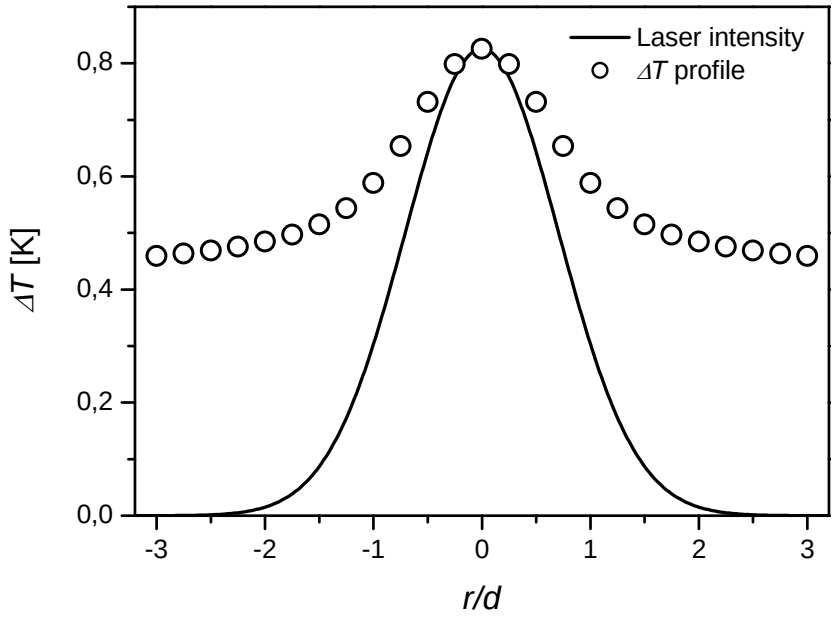

FIGURE 3.6: The calculated lateral profile (circles) of the photoinduced temperature increase ΔT in the illuminated area of $K_{0.3}MoO_3$ single crystal using Equation 3.13. The laser parameters are $d = 240$ μm, $P_0 = 1$ mW. The spatial profile of a normalized Gaussian beam intensity is shown for comparison (solid line).

3.1.4.2 Transient Heating

The second type of heating effect is transient heating where one needs to consider the heat buildup due to a single pulse that relaxes as $1/\sqrt{t}$. Of course, the temperature of the system can only be well defined after the initial relaxation of the system which takes place on a 10 ps – 50 ps time-scale. After this initial relaxation, the transient increase of temperature ΔT can be estimated if one considers the energy ΔW to be absorbed in a small illuminated volume V of a solid with density ρ_s and specific heat $c_s(T)$. In that case the estimate for the maximum increase of temperature is obtained from

$$\Delta W = \int_{T}^{T+\Delta T} \rho_s V c_s(T) dT. \tag{3.14}$$

For example, we can calculate the transient heating in a $K_{0.3}MoO_3$ crystal when it is illuminated by a laser beam with the diameter $d = 240$ μm, repetition rate $\nu = 25$ kHz and wavelength $\lambda = 800$ nm. The specific heat values are available in the literature [57], while the density can be calculated from the formula unit and the unit cell parameters[7] [56] and is $\rho_s = 1900$ kg/m^3. The illuminated volume is approximately $\delta_0 \pi (d/2)^2$, where $\delta_0 \approx 85$ nm is the absorption length for $\lambda = 800$ nm. The absorbed energy $\Delta W \approx (1 - R) W_p$ is obtained from the reflectivity R of the sample and the single pulse energy $W_p = P_0/\nu$, where P_0 is the average laser power and ν is the laser repetition rate. Using all the parameters in Equation 3.14 and solving it by method of bisection, we calculate the temperature increase and display the results in Figure 3.7. Panel a) in Figure 3.7 shows the temperature increase when the sample at initial temperature $T = 4$ K is heated by a laser with different fluences. Panel b) in Figure 3.7 shows the temperature increase when the initial temperature is varied and the excitation fluence is fixed ($F = 40$ μJ/cm^2).

The problem can also be treated in more detail where both the temporal and spatial properties of the pulse are taken into account and used in the expression for the net absorbed energy per unit volume and per unit time $A\left(\vec{r'}, t'\right)$ to solve Equation 3.6. When a pulse with Gaussian lateral (TEM_{00}) and temporal profile with a pulse width τ is considered then $A\left(\vec{r'}, t'\right)$ is expressed as

$$A\left(\vec{r'}, t'\right) = \frac{4(1-R)P_0\alpha}{\pi d^2} \exp\left[-\frac{2\left(x'^2 + y'^2\right)}{d^2}\right] \exp[-\alpha z'] \exp\left[-\frac{2t'^2}{\tau^2}\right]. \tag{3.15}$$

[7] Each unit cell contains $K_3Mo_{10}O_{30}$.

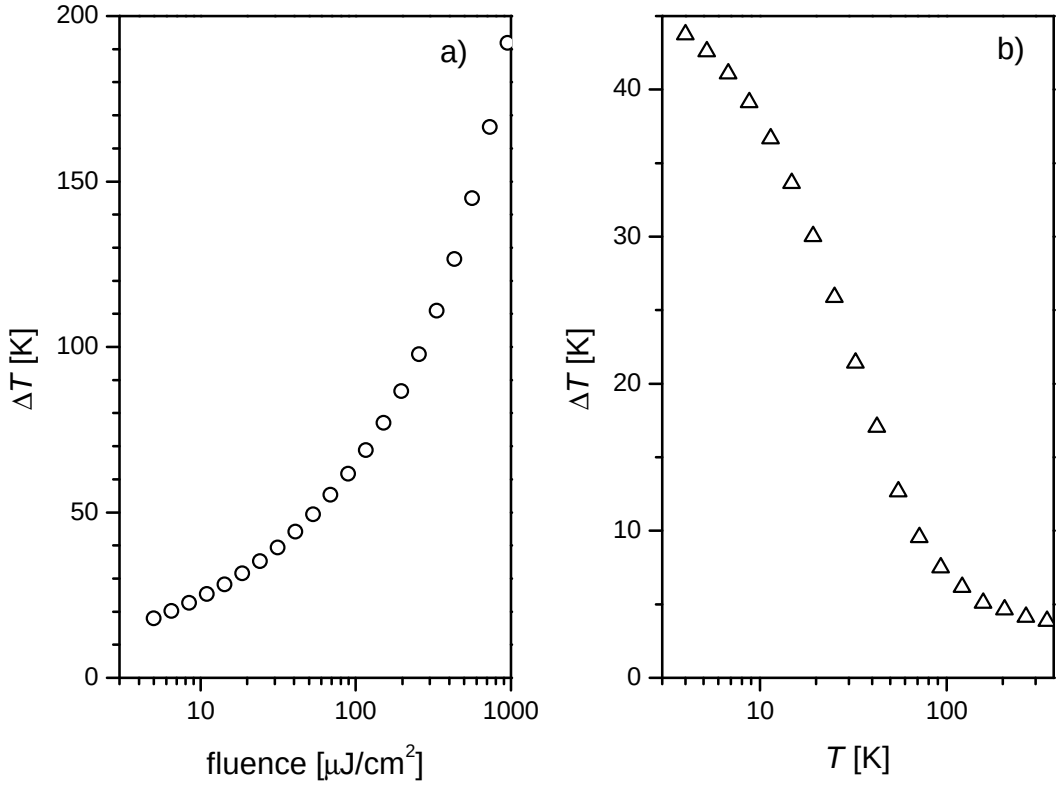

FIGURE 3.7: The transient heating in a $K0.3MoO_3$ crystal, calculated using Equation 3.14. Panel a) shows the calculated temperature increase at initial temperature $T = 4$ K at different laser fluences. Panel b) shows the calculated temperature increase at a fixed laser fluence ($F = 40$ μJ/cm^2) for different initial temperatures.

The appropriate Green's function that corresponds to the boundary condition 3.7 is again obtained by taking the Green's function for the infinite solid [103, 107] and applying the method of images.

$$\begin{aligned} G\left(\vec{r'}, t', \vec{r}, t\right) = & \frac{1}{8\sqrt{d_x d_y d_z \pi^3 (t-t')^3}} \\ & \cdot \exp\left[-\frac{1}{4(t-t')}\left(\frac{(x-x')^2}{d_x} + \frac{(y-y')^2}{d_y}\right)\right] \\ & \cdot \left(\exp\left[-\frac{(z-z')^2}{4d_z(t-t')}\right] + \exp\left[-\frac{(z+z')^2}{4d_z(t-t')}\right]\right). \end{aligned} \tag{3.16}$$

Here $d_i = \kappa_i/\rho_s c_s$ are the thermal diffusivities in the principal directions. The temperature rise is calculated by solving

$$\Delta T\left(\vec{r}, t\right) = \int_{-\infty}^{t} dt' \iiint_{z'>0} d\vec{r'} \frac{G\left(\vec{r'}, t', \vec{r}, t\right) A\left(\vec{r'}, t'\right)}{\rho_s c_s}. \tag{3.17}$$

The lateral part of Equation 3.17 can be solved to obtain the rise in temperature.

$$\Delta T\left(\vec{r},t\right)=\frac{P_0\alpha(1-R)}{4\pi\rho_s c_s}\exp(-\alpha z)\cdot\int_{-\infty}^{t}dt'\frac{\exp\left[-\frac{2t'^2}{\tau^2}+\alpha^2 d_z(t-t')-\frac{x^2}{4(t-t')d_x+d^2}-\frac{y^2}{4(t-t')d_y+d^2}\right]}{\sqrt{4(t-t')d_x+d^2}+\sqrt{4(t-t')d_y+d^2}}\cdot\left(1+\mathrm{erf}\left[\frac{2z-4\alpha d_z(t-t')}{4\sqrt{(t-t')d_z}}\right]+e^{2\alpha z}\left(1-\mathrm{erf}\left[\frac{2z+4\alpha d_z(t-t')}{4\sqrt{(t-t')d_z}}\right]\right)\right),\tag{3.18}$$

where $\mathrm{erf}(x)=\int_0^x\exp(-t^2)dt$.

3.2 Data Analysis

In these experiments the temperature and intensity dependence of the photoinduced reflectivity (or transmission) is measured. The data is then analyzed in terms of amplitudes and relaxation times of the different components of the signal. The oscillatory part of the signal is usually analyzed separately using FFT analysis. We plot a typical photoinduced $\Delta R/R$ signal on $K_{0.3}MoO_3$ in Figure 3.8 (red circles). The signal is zero when the *pump* beam is blocked (solid purple line), however if the laser repetition rate is high enough, even when the *pump* beam is unblocked, there is a non-zero long lived component present, seen as a signal at negative time delays. There are two exponentially decaying signals with amplitudes with decay times of approximately $\tau_1 \approx 200$ fs and $\tau_2 \approx 5$ ps, respectively. There is also a very long lived signal component that appears as a step function within our time window. Finally, the signal contains an oscillatory contribution, which is also plotted separately as red triangles.

The magnitudes of the amplitude and the relaxation time of the two exponential components of the signal on the time scales of 200 and 5 ps can be resolved relatively well. On the other hand, the magnitude of the slowest component due to single *pump* pulse can not be directly measured because it does not relax in the time between two successive *pump* pulses (12.8 ns at 88 MHz repetition rate). This results in the signal pile-up which is indicated in Figure 3.8. In the following analysis the amplitude of the signal A_4 is taken as the magnitude of the single *pump* pulse contribution to the slowest component, and A_0 as the pile-up of the slowest component.

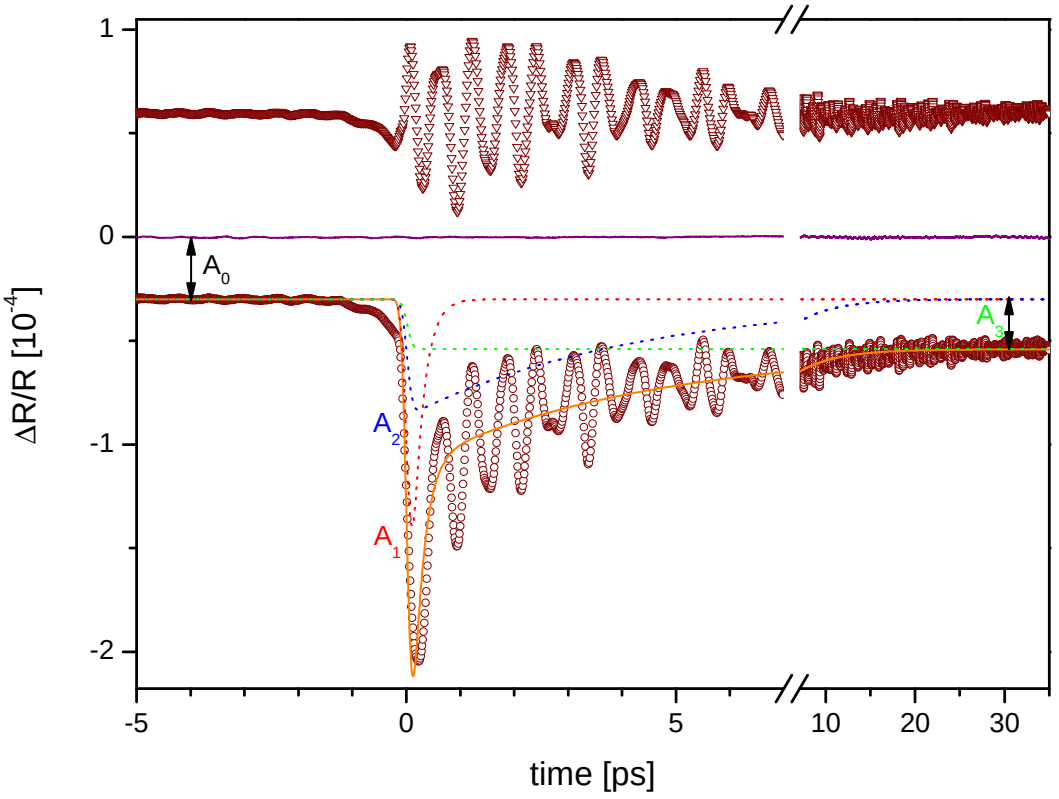

FIGURE 3.8: A typical photoindiced transient signal $\Delta R/R$ on $K_{0.3}MoO_3$ (red circles) and a typical signal when the *pump* beam is blocked (solid purple line) are plotted for comparison. A_0 is the offset between the two signals caused by signal pile-up. The solid orange line is the three exponent fit function $\tilde{A}(t)$ of the signal and the red triangles show the residual oscillatory signal when the fit is subtracted from the signal. The red, blue and green dotted lines show the three respective components with amplitudes A_1-A_3 of the fitting function.

By comparing the amplitudes A_0 and A_4 we estimate the timescale of the slowest component to be $\tau_4 \approx$ 1-10 ns, therefore it can be considered as a constant in the range of several 10 ps after photoexcitation and fitted by a step function with a finite rise time. The two fast components, on the other hand, have been found to be fairly well reproduced by a sum of two exponentially decaying functions with characteristic relaxation times that vary with temperature and *pump* intensity. The fit used in Figure 3.8 (orange solid line) is the sum of the three components that are depicted as the red, blue and green dotted lines.

In the case of single exponential decay, the signal component in the photoinduced change of reflection is a solution of

$$\begin{aligned} \frac{\partial A(t)}{\partial t} &= -\frac{A(t)}{\tau_R} + g(t), \\ A(t) &\equiv \frac{\Delta R}{R}. \end{aligned} \tag{3.19}$$

Here τ_R is the relaxation time and $g(t) = B\exp(2t^2/\tau_p^2)$ represents the temporal profile of the intensity of a Gaussian pulse with pulsewidth τ_p. Due to the finite pulsewidth of the *probe* pulse, the measured $\tilde{A}(t)$ is a convolution of $A(t)$ and $g(t)$. However, this affects only the rise time of the signal, so $\tilde{A}(t)$ can be approximated with the solution of the differential equation 3.19 with the effective rise-time σ

$$\tilde{A}(t) \simeq A_R \exp\left[-\frac{t}{\tau_R}\right]\left(1 - \mathrm{erf}\left[\frac{-4\tau_R t + \sigma^2}{2\sqrt{2}\sigma\tau_R}\right]\right). \tag{3.20}$$

Here A_R is the amplitude of the transient with relaxation time τ_R and $\mathrm{erf}(x) = \int_0^x \exp(-t^2)dt$. In the case that the intrinsic rise-time of the photoinduced signal was much faster than the pulsewidth, the effective rise-time would be $\sigma \approx \sqrt{2}\tau_p$. However, this is only the minimum rise-time expected in pump-probe measurements.

It should also be noted that the pump-probe experiments are usually performed with the pump and probe polarizations crossed - otherwise additional terms can contrubute to the signal close to the zero time delay between the *pump* and *probe* beams. These terms that are usually called *coherent artifacts* [108] arise from coherent interactions between the pump and probe beams. The interference between the two beams creates a grating in the sample which can diffract light and contribute to the signal. All of the measurements described in the thesis were performed in the crossed polarization so this will not be further discussed.

3.2.1 Nonlinear Regime

Since the $\Delta R/R$ signal is proportional to the number of excited quasiparticles, it saturates at high *pump* fluences when all the electron-hole pairs from the CDW condensate are excited across the gap. The model presented in this Section [28] addresses such a high fluence regime and accounts for geometrical aspects due to the finite absorption length and the transverse beam profiles of the *pump* and *probe* beams.

The sample penetration depth has to be accounted for twice in the probe beam (for entering and exiting the sample) which leads to the following relative photoinduced change in reflectivity

$$\frac{\Delta R}{R} \propto \int_0^\infty \int_0^\infty \exp\left(-2\frac{z}{\delta_0}\right) \exp\left(-2\frac{r^2}{\rho_{pr}^2}\right) n_{qp}(r,z) r\, dr\, dz. \tag{3.21}$$

Here δ_0 is the optical penetration depth and $2\rho_{pr}$ is the probe beam diameter on the sample. The reflectivity change is taken to be linearly proportional to the density of excited quasiparticles n_{qp} which is taken to be approximately linear with excitation fluence up to the threshold fluence F_s where the entire CDW condensate is melted. When $F > F_s$, all the electron-hole pairs are excited and n_{qp} saturates to n_s

$$n_{qp} \approx \begin{cases} \frac{F(r,z)}{F_s} n_s, & \text{if } F(r,z) < F_s \\ n_s, & \text{if } F(r,z) > F_s \end{cases} \tag{3.22}$$

The light fluence penetrating the sample is $F_0 = (1-R)F_{pu}$ where F_{pu} is the laser fluence on the sample surface. The fluence evolution within the sample is described by

$$F(r,z) = F_0 \exp\left(-\frac{z}{\delta_0}\right) \exp\left(-2\frac{r^2}{\rho_{pu}^2}\right). \tag{3.23}$$

If it is assumed that $\Delta R/R$ does not change with F in the normal state, the integral 3.21 can be calculated separately over the volume where $F(r,z)$ is smaller than F_s and separately over the volume where F_s is exceeded. Introducing the effective radius $\frac{1}{\rho_{eff}^2} = \frac{1}{\rho_{pu}^2} + \frac{1}{\rho_{pr}^2}$ the integral can be written as

$$\begin{aligned} &\frac{F_0}{F_s} n_s \int_0^\infty \exp\left[-\frac{3z}{\delta_0}\right] \left(\int_0^\infty \exp\left[-\frac{2r^2}{\rho_{eff}^2}\right] \Theta\left[1 - \frac{F(r,z)}{F_s}\right] r\, dr \right) dz \\ &+ n_s \int_0^\infty \exp\left[-\frac{2z}{\delta_0}\right] \left(\int_0^\infty \exp\left[-\frac{-2r^2}{\rho_{pr}^2}\right] \Theta\left[\frac{F(r,z)}{F_s} - 1\right] r\, dr \right) dz, \end{aligned} \tag{3.24}$$

where $\Theta(x)$ is the Heaviside step function. The behavior of the integral depends on the ratio F_0/F_s. The integral can be written in dimensionless form if it is normalized with its saturated value:

$$\frac{\Delta R_s}{R} \propto n_s \int_0^\infty \int_0^\infty \exp\left(-2\frac{z}{\delta_0}\right) \exp\left(-2\frac{r^2}{\rho_{pr}^2}\right) r\, dr\, dz = n_s \frac{\rho_{pr}^2 \delta_0}{8}. \tag{3.25}$$

When $F_0 \leq F_s$ then the measured reflectivity change is linearly proportional to fluence:

$$\frac{\Delta R}{\Delta R_s} = \frac{2F_0\rho_{eff}^2}{3F_s\rho_{pr}^2} = \frac{2}{3}\frac{1}{f(1+\bar{\rho}^{-2})}, \tag{3.26}$$

whereas for $F_0 > F_s$

$$\frac{\Delta R}{\Delta R_s} = \left(1 - f^2 + \frac{2\left(f\bar{\rho}^2 - f^2\right)}{\bar{\rho}^2 - 2} + \frac{\frac{6f\bar{\rho}^2}{1+\bar{\rho}^{-2}} - 2f^2\bar{\rho}^2}{6 - 3\bar{\rho}^2}\right), \tag{3.27}$$

where $\bar{\rho} = \rho_{pu}/\rho_{pr}$ and $f = F_s/F_0$. The saturation fluence F_s can be simply determined from Equation 3.26. When $F = F_s$, $\Delta R/R$ reaches $\frac{2\rho_{eff}^2}{3\rho_{pr}^2}$ of the saturation value $\Delta R_s/R$.

Sometimes the penetration depths of the two beams are different - due to the anisotropy of the material or due to different wavelengths of the two beams. In that case the fluence evolution within the sample is

$$F(r,z) = F_0 \exp\left(-\frac{z}{\delta_{pu}}\right) \exp\left(-2\frac{r^2}{\rho_{pu}^2}\right), \tag{3.28}$$

where δ_{pu} and δ_{pr} are the penetration depths of the *pump* and *probe* beams, respectively. For $F_0 \leq F_s$ the measured reflectivity change is linearly proportional to fluence and can be expressed as

$$\frac{\Delta R}{\Delta R_s} = \frac{F_0}{F_s}\frac{\rho_{eff}^2}{\rho_{pr}^2}\frac{2\delta_{pu}}{2\delta_{pu} + \delta_{pr}}. \tag{3.29}$$

3.3 Displacive Excitation of Coherent Phonons

In pump-probe experiments on a number of different conducting and semiconducting materials oscillations have been observed in photoinduced reflectivity with frequencies corresponding to the optical phonon modes of materials. In this section, we discuss the mechanism proposed for describing oscillatory components in several semiconductors and semimetals, where only A_1 symmetry Raman-active modes were observed, even though modes of comparable strength with different symmetries also occur in Raman spectra of these materials. The model was named displacive excitation of coherent phonons (DECP) [109] due to obvious reasons explained later in this section.

DECP [109] was shown to be one of the limiting cases of the more general impulsive stimulated Raman mechanism [110]. In DECP, after being excited by the *pump* laser pulse, the electronic system comes to a quasi-equilibrium in a time short compared to

the oscillation period of the lattice. This quasi-equilibrium is described by the density of the photoinduced carriers $n_p(t)$. Equilibrium positions of ions in the perturbed state are different then in the initial state so ions find themselves displaced from the new equilibrium positions and start to oscillate. This gives rise to a change in reflectivity which oscillates with the characteristic lattice vibration frequency.

The basis of DECP is the postulation that the origin of the oscillations is a change in the quasi-equilibrium A_1 coordinate $Q_0(t)$ ($Q_0(t < 0) = 0$ is the state before the photoexcitation). The A_1 modes are the so called "breathing modes", where the ionic displacements do not change the symmetry. The equilibrium value of A_1 displacements is determined by minimizing the free energy of the system. Therefore, the equilibrium positions of the nuclei should be a function of temperature and electronic distribution.

Photoexcitation can cause either increased electron temperature $\Delta T(t)$ or interband transitions leaving $n_p(t)$ electrons per unit volume in the excited bands. Both, the increase in the electronic temperature and the increase of the occupation number of states in bands above E_F may lead to a change in the quasi-equilibrium A_1 ionic coordinate. This happens on a timescale which is short compared to the equilibration time of an ionic system, thereby coherently exciting the A_1 vibrational mode. Even though it is not clear which of the two sources is dominant, both lead to a similar result. Therefore, for the sake of simplicity, in the following derivation $n_p(t)$ is assumed to be the main source. The rate of change of $n_p(t)$ is described by

$$\frac{dn_p(t)}{dt} = \rho P(t) - \beta n_p(t), \tag{3.30}$$

where the first term on the right describes the rate of generation of the carriers in the excited band which is assumed to be proportional to the *pump* pulse temporal profile and ρ is the proportionality constant. The second term describes the relaxation of electrons back to the ground state. When the perturbation is small, it is reasonable to assume that the dependence between the A_1 equilibrium coordinate and $n_p(t)$ is linear. Therefore

$$Q_0(t) = \kappa n_p(t), \tag{3.31}$$

where κ is the proportionality constant and $Q_0(t < 0) = 0$. The equation governing the time dependence of the coordinate $Q\,(t)$ is then

$$\ddot{Q}\,(t) + 2\gamma\dot{Q}\,(t) + \omega^2\,(Q(t) - Q_0(t)) = 0, \tag{3.32}$$

where ω is the eigenmode frequency and γ is its damping constant. Both the measurements and Equation 3.30 indicate that the photoinduced carrier density relaxes exponentially so the A_1 equilibrium position function can be written as a simple exponential decay[8] $Q_0(t) = Q_0(t=0)e^{-t/\tau_1}$. In that case the solution of Eq. 3.32 is a damped oscillator with a renormalized frequency $\tilde{\omega} = \sqrt{\omega^2 - \gamma^2}$

$$Q(t) \propto \cos(\tilde{\omega}t) - \frac{1/\tau_1 - \gamma}{\tilde{\omega}} \sin(\tilde{\omega}t), \tag{3.33}$$

with the phase of the oscillation given by

$$\varphi = \arg\left(1 - \imath\frac{1/\tau_1 - \gamma}{\tilde{\omega}}\right). \tag{3.34}$$

3.3.1 Critical Discussion about DECP

The simple DECP solution given by Equation 3.33 is only obtained when the laser pulse can be approximated by a delta function in comparison with the electron relaxation. However, our experimental results show that the rise and relaxation time are of the same order of magnitude (100 – 200 fs) so we tried to obtain a more general solution.

The function $P(t)$ describing the laser pulse in Equation 3.30 is generally described fairly well with a Gaussian function

$$P(t) = P_0 \exp\left(-\frac{t^2}{2\sigma^2}\right), \tag{3.35}$$

where 2σ is the temporal width of the pulse and P_0 is proportional to the laser fluence. Equations 3.30 and 3.35 can be analytically solved to obtain the number of excited quasiparticles

$$n_p(t) = n_p^0\left(1 - \mathrm{erf}\left[\frac{\beta\sigma^2 - t}{\sqrt{2}\sigma}\right]\right)\exp(-\beta t), \tag{3.36}$$

where n_p^0 is a parameter proportional to the laser fluence. This function behaves like a normal exponential function when $t \gg \beta\sigma^2$, so since in our case $\frac{1}{\beta} \approx \sigma$, Equations 3.33 and 3.34 are good approximations when $t \gg \sigma$. Since the typical phonon decay time is $\sim$ 10 ps while $\sigma \approx 60$ fs, Equations 3.33 and 3.34 are not valid only on the sub-picosecond time scale. To test this, we solved Equations 3.32 and 3.36 numerically

[8] Analytically, this is only the case when the function $P(t)$ in Equation 3.30 is a delta function, which is a good approximation when the laser pulse is much shorter than the electron relaxation time.

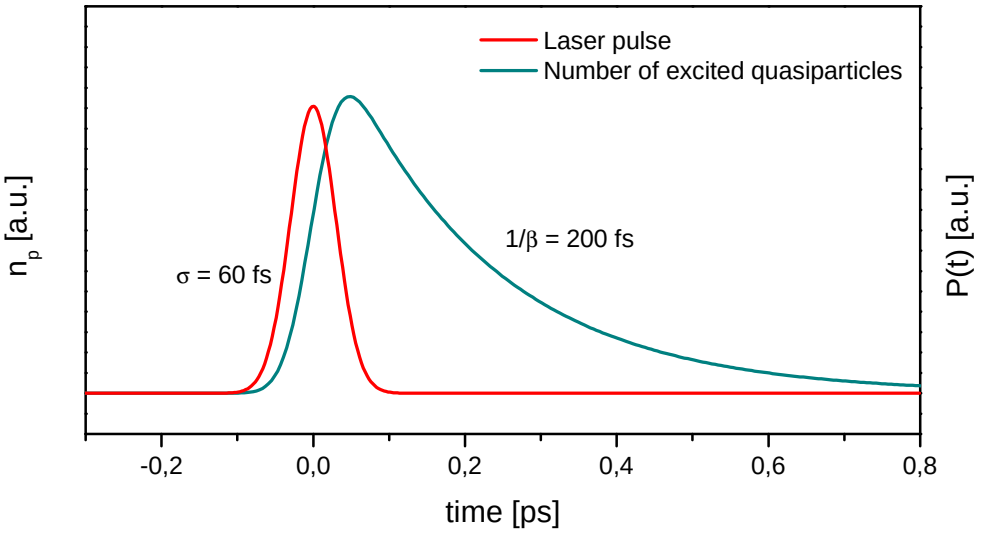

FIGURE 3.9: The red line depicts a typical laser pulse with $\sigma = 60fs$ (see Equation 3.35) which excites quasiparticles across the gap (blue line) according to Equation 3.36.

(since no simple analytical solutions exist). The numerical solution obtained this way is qualitatively similar to the experimentally obtained data for the blue bronze at low temperatures so we compared the experimentally obtained data, the numerical solution and a typical fit using a sum of several exponential functions[9] and a damped oscillator. We present the comparison in Figure 3.10.

The orange line in Figure 3.10 displays a sum of a numerical DECP solution, an exponentially decaying function ($\tau_2 \approx 10$ ps) and a step function describing heating whereas the blue line displays a sum of two exponentially decaying functions ($\tau_1 \approx 200$ fs, $\tau_2 \approx 10ps$) and a step function, which is a typical fitting function in this case [23]. It is clear that both curves overlap when $t > 1$ ps and that both describe the qualitative behavior of the experimentally obtained data. The numerical DECP solution is evidently a worse fit in the subpicosecond range (see the inset of Figure 3.10) so additional terms are needed to describe the experimental data. One can also see that the phase of the oscillations of all the curves already matches at the first minimum so it can be concluded that Equation 3.34 is always a good approximation.

Even without this analysis one can speculate that within the frameworks of DECP the change of reflectivity has two contributions in the subpicosecond range. The first contribution is the change of reflectivity caused by the optically excited quasiparticles (described by Equation 3.36), while the second contribution is caused by ionic motion. Our analysis seems to indicate that the second contribution is the prevailing one in this case. As a final step, we also fit the data with a sum of the numerical DECP solution

[9]The rise time is determined by Equation 3.36.

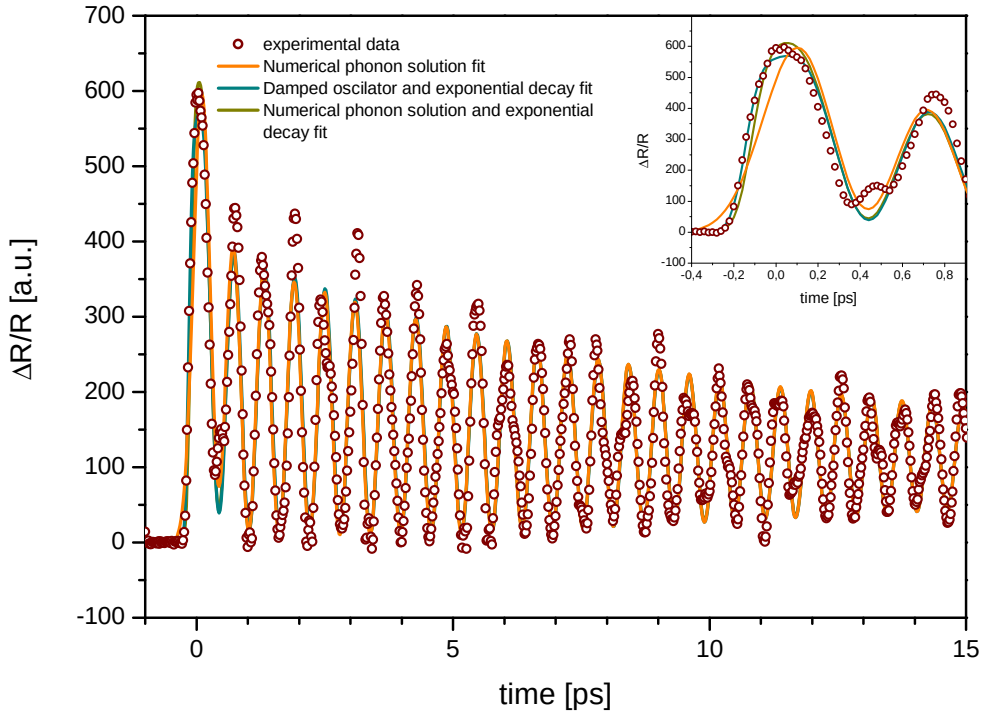

FIGURE 3.10: The comparison between the experimental data (open circles) with the numerical solution of Equations 3.32 and 3.36 (orange line) and a fit using a sum of an exponential function (see Equation 3.36) and a damped oscillator. The only difference between the two fitting functions occurs when $t < 1$ ps, where the sum of an exponential function and a damped oscillator provides a better fit (see the inset)

and an exponentially decaying term with a matching[10] $\tau_1 = 1/\beta$ (see Equation 3.36) which is plotted as a yellow line in Figure 3.10 and we obtain a very good fit.

One must of course also be aware that the main contribution to the disagreement of the data and all the fitting curves are strong additional phonon modes. However, the daunting task of incorporating them into this simple model is beyond the scope of this analysis.

[10]Therefore only one fitting parameter was added instead of two.

Chapter 4

Ultrafast Relaxation Phenomena in $K_{0.3}MoO_3$

4.1 The structure of $A_{0.3}MoO_3$

Molybdenum oxides $A_{0.3}MoO_3$, where A is a monovalent metal like K, Rb, or Tl, are also called blue bronzes due to their shiny blue appearance. These oxides are well known for their interesting electronic properties arising from their one-dimensional (1D) chain structures [60, 80]. Figure 4.1 shows the schematic structure of $K_{0.3}MoO_3$, which crystallizes in a monoclinic unit cell with room temperature lattice parameters [56, 111] $a = (18.249 \pm 0.010)$ Å, $b = (7.560 \pm 0.005)$ Å, $c = 9.855 \pm 0.006$ Å and $\beta = 117°32'$. The structure contains rigid units comprised of clusters of ten distorted MoO_6 octahedra, sharing corners along the monoclinic b-axis. Due to this corner sharing electrons have an easy path along the chain direction. The chains also share corners along the [102] direction and form infinite slabs separated by the potassium cations. The cleavage plane is defined by the [102] and [010] directions. There are 4 CDW chains per unit cell and the CDW wavelength is close to $\frac{4}{3}b$. At room temperature $K_{0.3}MoO_3$ is a highly anisotropic one dimensional conductor with conductivity ratios $\sigma_b : \sigma_{2a-c} : \sigma_{2a+c} = 30 : 1 : 0.05$. This enables one to treat $K_{0.3}MoO_3$ as a quasi-one-dimensional metal. The Peierls transition into the CDW state occurs at $T_c^{3D} = 183$ K [60].

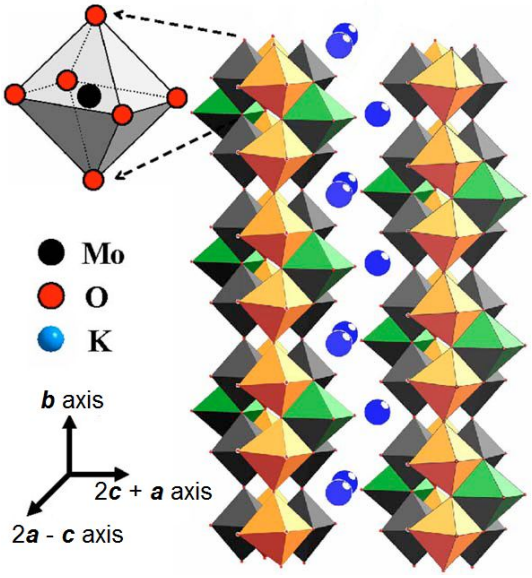

FIGURE 4.1: The structure of transition metal oxides consist of chains of MO_6 octahedra along the crystallographic b direction that share corners.

4.2 Low Perturbation Regime

4.2.1 Introduction

Our femtosecond time-resolved optical measurements on $K_{0.3}MoO_3$ and $Rb_{0.3}MoO_3$ were motivated by the major progress that has been made in the last couple of years in theoretical understanding of the relaxation phenomena in systems with a narrow gap in the density of states. In particular, it was shown that the Rothwarf-Taylor (RT) model (see Appendix A) captures the main underlying physics of the relaxation processes in superconductors [24, 34] as well as in heavy electron systems [112].

The first ultrafast optical measurements on $K_{0.3}MoO_3$ seemingly confirmed that dynamics of CDW materials could be described by the same bottleneck model [23]. The temperature dependence of both the amplitude and the relaxation time of the photoexcited transient reflectivity near the transition temperature fit the theoretical prediction well (see Equations (6) and (25) in Ref. [36]). On the other hand, the low temperature predictions of the RT model were not tested due to sample heating. In particular, there is an important prediction given by Equations A.16 and A.20 that states that at very low temperatures and excitation intensities the relaxation time should diverge with decreasing excitation intensity for both weak and strong bottleneck regimes. Therefore, we have performed detailed temperature and excitation intensity dependent measurements in order to test the RT model validity for blue bronze and to determine whether the

assignment of various relaxation processes made in Ref. [23] holds or an alternative model is needed.

4.2.2 Experimental results

In the experiments described in this Section, we used 60 fs laser pulses at 1.55 eV (λ = 800 nm) from a commercial Ti:saphire oscillator with repetition rate of 80 MHz as a source of both photoexcitation (*pump*) and *probe* pulse trains (see Section 3.1.3 for more detail). The *probe* pulse train was delayed with respect to the *pump* pulse train using a delay stage and small changes in R were recorded using the lock-in detection technique (see Section 3.1.2). The experiments were performed on single crystals of $K_{0.3}MoO_3$ and $Rb_{0.3}MoO_3$ with the *probe* polarization along the chain direction while *pump* beam was polarized along [102] direction. The direction of the *probe* polarization was chosen to maximize the incoherent response signal [23] while the *pump* polarization was perpendicular to that direction in order to minimize the signal noise caused by the scattering of the *pump* beam[1]. The samples were mounted in an optical cryostat and the temperature was varied between 4 and 300 K using liquid helium as a cooling agent. The temperatures were measured at the cold finger of the cryostat. Dynamics was studied in the range of excitation fluences between $F \approx 0.01$ μJ/cm^2 $-$ 1 μJ/cm^2. The reduced pulse duration, much improved S/N ratio and longer range of the time-delay studied enabled us to determine the relaxation timescales with much higher precision compared to the earlier report [23].

Figure 4.2 shows the induced reflectivity transients in $K_{0.3}MoO_3$ normalized to the excitation fluence recorded at 4 K. It clearly shows that the relaxation dynamics does not depend on excitation fluence over a large range in excitation fluence. In fact, measurements utilizing a regenerative amplifier showed that dynamics is F-independent up to several 10 μJ/cm^2 where strongly nonlinear regime is reached leading to photoinduced semiconductor-metal phase transition[2] [29]. The fact that the dynamics is independent of excitation fluence over such wide range of excitation fluence is clearly at odds with the RT model, which predicts that in both weak and strong bottleneck regime at low temperatures the relaxation rate should increase with excitation fluence [34] (see Equations A.16 and A.20).

Moreover, we have also performed temperature dependent measurements in the low excitation fluence limit, where the RT model predicts slowing down of relaxation upon cooling (see Equations A.16 and A.20). We measured the reflectivity transients in the

[1] There is always some scattered *pump* beam light from the sample that reaches the detector which can be problematic when using the lock-in detection technique.

[2] These results are presented in Section 4.3.

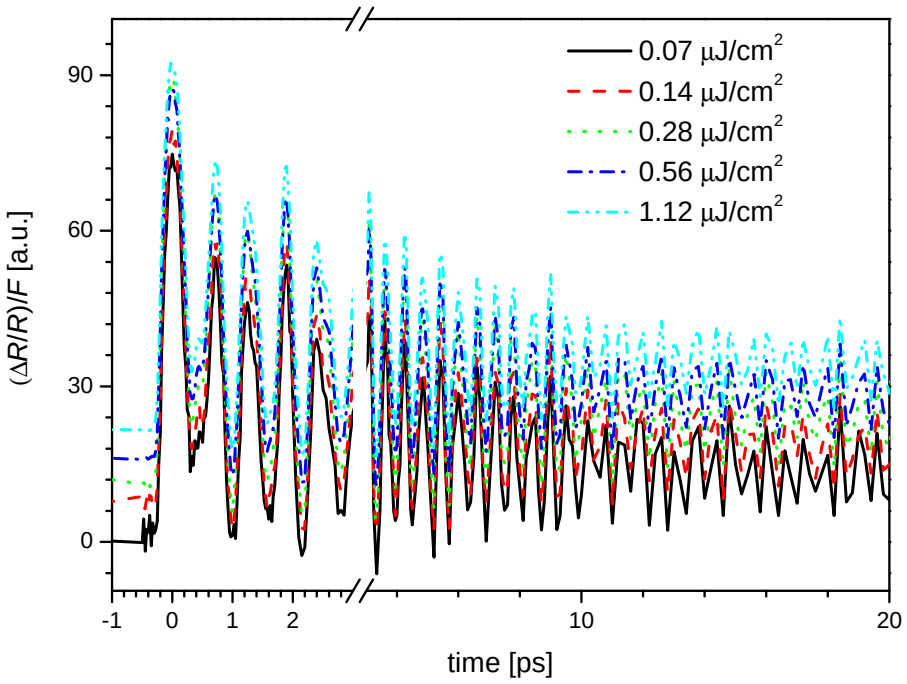

FIGURE 4.2: Normalized reflectivity transients at different excitation fluences measured at 4 K overlap almost perfectly. Data are shifted vertically for clarity.

temperature range from 4 K to room temperature with the emphasis on the measurements below 50 K, where there were no data reported previously due to heating [23]. The data above the transition temperature can be well modeled by a single exponential decay. The data below the transition temperature fit well to a sum of two exponential functions and a damped oscillatory part

$$S(t) = A_1(t)e^{-t/\tau_1} + A_2(t)e^{-t/\tau_2} + A_{osc}e^{-\beta t}\sin(\omega t - \phi). \tag{4.1}$$

We plot the two distinct relaxation times τ_1 and τ_2 in Figure 4.3a. The data show that both relaxation times are roughly constant at temperatures below $T \approx 70$ K. Above this temperature τ_1 increases, showing a quasi-divergence as T_c^{3D} is approached while τ_2 gradually decreases. It is noteworthy that above $T \approx 70$ K τ_2 and the amplitude mode decay time γ^{-1} have nearly the same temperature dependence up to T_c^{3D}, as shown in Figure 4.3b. The fact that τ_1 is temperature and pump intensity independent below ≈ 70 K is also in disagreement with the prediction of the RT model given by Equations A.16 and A.20.

We plot the two distinct amplitudes A_1 and A_2 (see Equation 4.1) in Figure 4.4. Both amplitudes decrease with increasing temperature up to ≈ 30 K. A_1 is roughly constant above 30 K up to ≈ 120 K, then it starts decreasing when approaching the transition temperature T_c^{3D}. A_2 is roughly constant up to ≈ 80 K, has a local maximum around

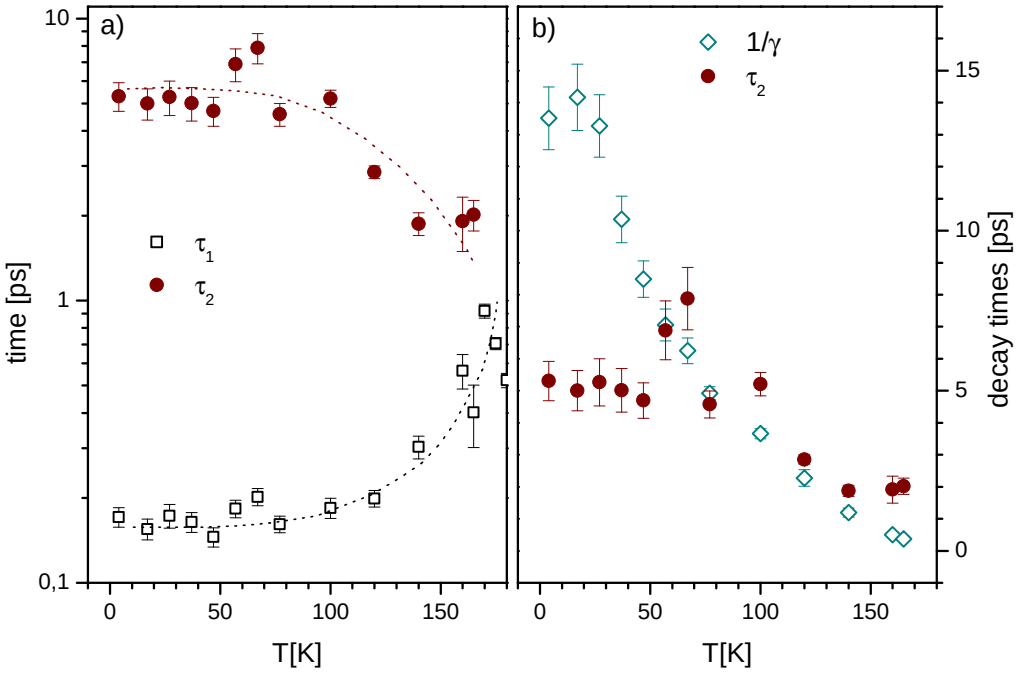

FIGURE 4.3: Panel a) shows the temperature dependence of the two distinctive relaxation times obtained from the fit. The dotted lines are guides to the eye. Panel b) shows the longer relaxation time and the AM decay time obtained from the fit on the same graph.

≈ 120 K, then it follows the behavior of the amplitude A_1 and drops towards zero when approaching the transition temperature T_c^{3D}. Both components are easily distinguished at low temperatures due to the very different time-scales. On the other hand, the time scales become comparable near the transition temperature (see Figure 4.3) so the distinction becomes more difficult and may even distort the temperature dependence information[3].

The main oscillatory component in the induced reflectivity transient with frequency of about 1.7 THz is due to coherently excited amplitude mode. As a result of an improved S/N ratio and shorter pulse duration compared to earlier report, [23] we were in addition to its frequency and damping able to resolve also the temperature dependence of its phase, ϕ. As shown in Figure 4.5, ϕ has a pronounced temperature dependence.

Since $K(Rb)_{0.3}MoO_3$ is opaque, the simplest model that explains the coherent phonon (or amplitudon) generation is the *displacive excitation of coherent phonons* model (DECP) [109], which is explained in more detail in Section 3.3. In DECP, the phase of the coherently generated phonon is determined by Equation 3.34, which predicts that the phase φ is determined by the electron relaxation rate, the phonon frequency and its damping. We have therefore used equation 3.34 and calculated the phase from the

[3]This is likely the reason why the temperature dependence of A_1 shows some deviation from the behavior presented in the first report [23].

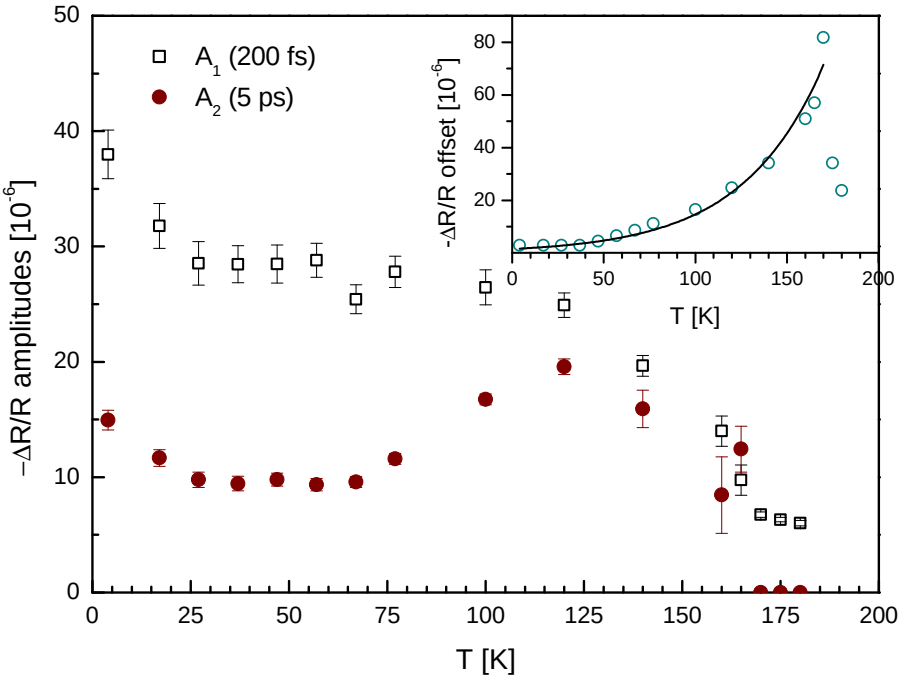

FIGURE 4.4: The temperature dependence of the amplitudes of both exponentially relaxing components of the transient signal show a decrease near the transition temperature. The inset figure shows the temperature dependence of the long-lived signal pile-up. It displays a maximum at the transition temperature and exponential behavior below it (solid line).

parameters (τ_1, γ, ω) obtained from fitting the T-dependent data and compared the results with the measured phase. The data match remarkably well as we show in Fig. 4.5. Since both γ and τ_1 show a strong T-dependence above $T \approx 70$ K (see Fig. 4.3), we wanted to check which is the dominant term governing the temperature dependence of φ. Comparison of the calculated phase with τ_1 fixed at its low temperature value of 200 fs shows that the T-dependence of γ is not enough to account for the $\varphi(T)$ variation. This, together with anomalous slowing down of the fast relaxation with $\tau_1 \propto 1/\Delta(T)$, lend further support to the assignment of the initial relaxation dynamics to the electronic order parameter recovery.

In the second set of experiments we have studied the induced reflectivity dynamics as a function of applied electric field along the chain direction. For this, we made two electrical contacts on the surface of each of the samples using silver paste. After cooling the samples, we used a voltage source to measure the I-V characteristics which showed similar behavior as commonly observed [113]. We measured the photoinduced reflectivity transients between the contacts at several temperatures below T_c^{3D}. Within experimental uncertainty no change in the relaxation dynamics was observed on the applied electric field up to the second threshold field, where pronounced sample heating was observed. Since the penetration depth of the 800 nm light is small (85 nm), one could expect that a large portion of the current flows deep in the bulk without being

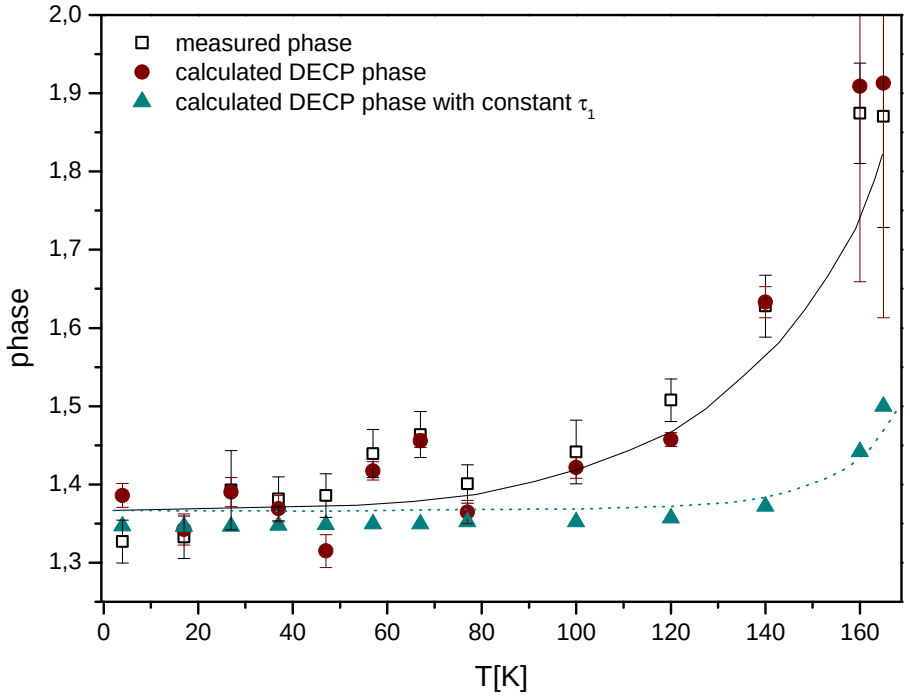

FIGURE 4.5: Temperature dependence of the phase of the coherently excited AM, ϕ (black squares), compared to ϕ calculated using the DECP model (red circles) with the driving force $g(t)$ governed by the build-up and subsequent decay of the photoinduced QP population. We show that $\phi(T)$ is governed by the T-dependence of the decay of the QP population τ_1(the green triangles show the prediction of the DECP model for ϕ if τ_1 is constant ($\tau_1 = 0.2$ ps). The solid and dotted lines are displayed as guides to the eye.

affected by the laser illumination. However, the large resistivity of $K_{0.3}MoO_3$ in the [201] direction and the photoinduced transport measurements by Ogawa et al. [114] suggest that the current contribution near the surface is not negligible. While the effect of the applied electric field on the relaxation of the phase mode is unclear, the fact that no change in the relaxation dynamics on temperature (up to 100K), excitation fluence (over 3 orders in magnitude) and the applied electric field is observed seems to rule out the (tentative) assignment [23] of the 10 ps component to the phase mode.

Finally, given the much improved signal to noise ratio in our experimental set-up with respect to the initial report [23], we were able to observe a number of additional phonon modes via the Fourier transform of our real-time data. After fitting out the incoherent part of the response, we performed FFT and obtained very sharp phonon lines in both materials - see Figure 4.6. The mode frequencies agree well with the phonon lines observed in Raman experiments [82]. In general, the frequencies of the modes observed in $Rb_{0.3}MoO_3$ are slightly lower than the corresponding modes in $K_{0.3}MoO_3$which agrees with slightly larger lattice constants in $Rb_{0.3}MoO_3$.

Let us now discuss the implications of these measurements. In the model [36] used in

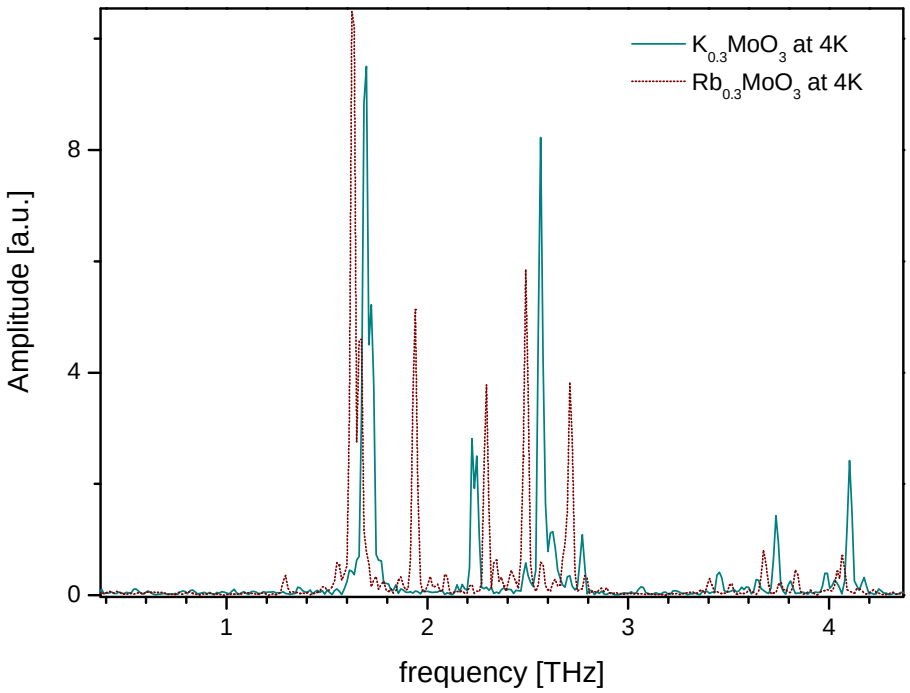

FIGURE 4.6: The sharp phonon spectra of $K_{0.3}MoO_3$ (black solid line) and $Rb_{0.3}MoO_3$ (red dashed line) measured at 4 K. Numerous phonon lines are in agreement with Raman data [82]. The strongest modes near 1.7 THz correspond to the amplitude mode of the two compounds.

the original paper [23], the assumption was made that after excitation across the CDW gap, the excited QP and phonons reach thermalization on a fast timescale ($t \geq 10$ fs). This causes a bottleneck in the relaxation of QP which is especially effective near the transition temperature T_c^{3D} and causes a divergence of the QP relaxation time near T_c^{3D}. This model was later adopted by different authors for explaining the divergence of the QP relaxation time in various CDW systems[23, 39, 42]. Effectively, this is the RT scenario in the strong bottleneck regime which is described in more detail in Appendix A.1. This regime can be described briefly in the following manner. If the electron gap 2Δ is of the order of the phonon cut-off frequency, then the excited QPs can relax across the electronic gap by emitting optical phonons with $\nu > 2\Delta$. These phonons can then either be reabsorbed by creating two QPs or they can decay (via diffusion out of the probed volume or by anharmonic decay). In the strong bottleneck regime, the phonon anharmonic decay is much slower than the QP relaxation across the gap, so the QP relaxation is governed by the phonon decay time. Near the transition temperature, the electronic gap closes, effectively decreasing the number of available $\nu < 2\Delta$ phonons, thereby increasing the decay time. This leads to the intuitive conclusion that in the bottleneck regime when approaching the transition temperature from below, the QP relaxation time diverges, which is observed in different CDW materials [23, 39, 42]. However the RT physics also predicts that in the strong bottleneck regime the QP relaxation time should diverge with decreasing excitation intensities at low temperatures

(see Equation A.16). In our measurements we do not observe any divergence of relaxation times at low temperatures even when the excitation intensity is decreased by several orders of magnitude, which speaks against the strong bottleneck regime in $K_{0.3}MoO_3$.

In principle, the system could also be in the weak bottleneck regime at low temperatures. In the weak bottleneck regime, the decay of optical phonons with $\nu > 2\Delta$ happens on a time scale which is faster than the QP relaxation so the QP effectively experience bi-molecular relaxation. In the case of bi-molecular relaxation, the QP relaxation time is again expected to be strongly F dependent at low temperatures (see Equation A.20), in contrast with the result of our measurements.

4.3 High perturbation regime

4.3.1 Introduction

In superconductors (SC), it has been known for decades that an intense laser pulse can non-thermally destroy the SC ground state [115]. The energy required to destroy SC should, in case all the absorbed optical energy is kept in the electronic subsystem during the process of SC suppression, be equal to the condensation energy (energy difference between the free energy of the SC and normal states at T = 0 K). In recent experiments on MgB_2 [116, 117] and the high-T_c SC $La_{2-x}Sr_xCu_2O_4$ [28] it has been shown, however, that the absorbed optical energy required to suppress SC is substantially higher than the thermodynamically measured condensation energy [28]. This discrepancy was accounted for by considering in detail all energy relaxation pathways on the timescale when SC suppression is achieved. From this analysis it follows that on this timescale a quasi-equilibrium between the density of quasiparticles and high frequency phonons is achieved with most of the absorbed energy density being stored in the phonon subsystem [28, 116, 117].

Charge density wave systems present another broken symmetry ground state. Here upon cooling through the CDW transition temperature the translational symmetry is broken [60] (also see Chapter 2). While real-time studies of photoexcited quasiparticle and collective mode dynamics in CDW compounds have been quite extensive in the weak and moderate perturbation regime [10, 23, 24, 40, 118], systematic studies in the high perturbation regime, where the energy of the optical excitation pulse is enough to drive the phase transition from the CDW ground state to the normal metallic state [41, 43], were still lacking.

In this Section we present the first systematic study of carrier and collective mode dynamics in the high perturbation regime in $K_{0.3}MoO_3$. Systematic temperature and excitation density dependent measurements of the PI reflectivity changes reveal that the phase transition from the ground CDW state to the normal metallic state can be achieved on the femtosecond timescale. From the energy conservation law it follows that the phase transition is non-thermal in origin; i.e. the phase transition is not a result of a simple heating of the sample to above the critical temperature. The absorbed energy density required to optically induce the phase transition is found to be comparable to the electronic energy difference upon CDW condensation. These results give new insight in the ultrafast processes governing the relaxation dynamics in low dimensional CDW systems. In particular, the results suggest that on the timescale shorter than the period of the characteristic lattice vibrations (≈ 0.6 ps in $K_{0.3}MoO_3$, which is the inverse frequency of the AM [23, 119]) the charge density modulation is suppressed while the lattice remains unperturbed keeping the 2 k_F modulation.

4.3.2 Experimental results

We studied the excitation intensity and temperature dependence of the PI reflectivity dynamics in single crystals of blue bronze $K_{0.3}MoO_3$ using a degenerate optical pump-probe technique. We used a commercial Ti:Sapphire amplifier producing 6 μJ, 50 fs laser pulses at $\lambda = 800$ nm (photon energy of 1.55 eV) at a variable repetition rate between 9 and 250 kHz (see Section 3.1.3 for more details). The laser was used as a source of both excitation and probe pulses. Samples were mounted in an optical helium flow cryostat, with both excitation and probe beam entering the sample at near normal incidence. Due to the strong anisotropy of the induced changes in reflectivity with respect to light polarization [23], the probe laser beam was polarized along the chain [010] direction, while the excitation beam was polarized along the perpendicular [102] direction [60]. To ensure a homogeneous excitation profile, the diameter of the pump beam at the sample position was twice the diameter of the probe beam. To determine the photoexcitation density at the position of the sample with high precision we used a beam profiler. We fitted the beam profile with a Gaussian, and the excitation fluences, F, used throughout the Section correspond to the maximum fluence at the center of the beam. Low thermal conductivity in $K_{0.3}MoO_3$ [57] can lead to a pronounced increase of the equilibrium temperature in the probed volume, proportional to the average laser power. Therefore, the high excitation experiments were performed at a low repetition rate (10-30 kHz), where at $F = 1$ mJ/cm^2 the temperature increase is $\lesssim 10$ K.

Figure 4.7 presents the induced reflectivity transients taken at 4 K at several excitation densities. At low excitation densities the data show the same behavior as previously

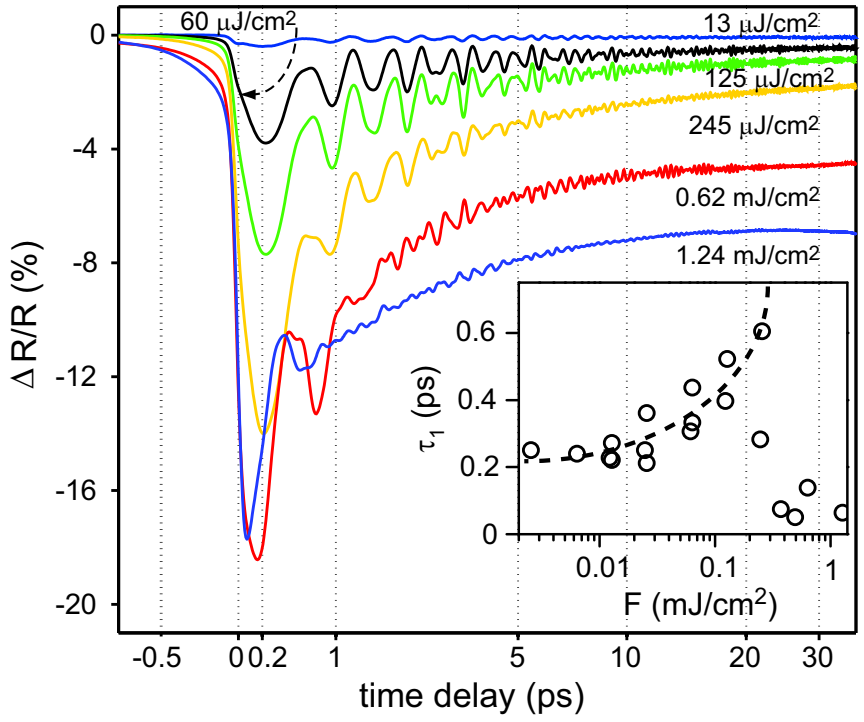

FIGURE 4.7: PI reflectivity changes in $K_{0.3}MoO_3$ at 4 K following photoexcitation with 50 fs optical pulses at different excitation fluences. For presentation purposes the x axis is logarithmic with zero time delay shifted to 1.5 ps prior to logarithmation. Inset: the $F-$dependence of the initial decay time τ_1 determined by fitting the data as described in the previous Section. $\tau_1(F)$ displays critical behavior near the threshold fluence of $\approx 200\ \mu J/cm^2$ (dashed line is a guide to the eye).

reported [23] and described in Section 4.2. The decay dynamics of the (incoherent) electronic response show a bi-exponential decay with timescales $\tau_1 \approx 0.3$ ps and $\tau_2 \approx 7$ ps. The former one, showing critical slowing down upon approaching T_c^{3D}, was attributed to the recovery of the CDW gap, while the second one was initially tentatively attributed to an overdamped phase mode [23]. Recent detailed studies of the dynamics as a function of F and applied external electric field however suggest that this longer timescale more likely presents the second stage of the CDW recovery [35]. On top of the incoherent transient an oscillatory (coherent) signal is observed whose Fourier transform, obtained by Fast Fourier Transform (FFT) analysis, shows several frequency components which can be attributed to the coherently excited AM (the strongest mode at 1.68 THz) and several other phonon modes [23, 35, 41].

While the PI transient is linear in F over several orders of magnitude (also See Section 4.2), we observe pronounced changes upon increasing the excitation intensity into the 100 $\mu J/cm^2$ range. The electronic component shows clear saturation at $F \gtrsim 200\ \mu J/cm^2$ with a maximum induced change in reflectivity approaching 18 % [4]. One is tempted to ascribe

[4]Similar saturation behavior was observed also in Ref. [41]. There saturation is seen at higher fluences, which can be ascribed to the different experimental configuration used.

this saturation behavior in reflectivity change to the PI suppression of the CDW order, where this difference in reflectivity corresponds to the change in reflectivity between the normal metallic and the CDW state. Since no measurement of the temperature dependence of reflectivity at optical frequencies is reported to date, we have performed thermomodulation measurements to determine the magnitude and sign of change in equilibrium reflectivity upon increasing the temperature to above T_c^{3D}. We measured the reflectivity difference between CDW and metallic state at 1.55 eV (800 nm) by heating the sample to above the phase transition using a CW laser. The data show that the reflectivity at 800 nm indeed decreases upon increasing the temperature. The change in reflectivity of ~ 10 % was observed upon heating from 160 K to just above T_c^{3D}. At temperatures above T_c^{3D} the corresponding change in equilibrium reflectivity was less than 1 %. Therefore the observed reflectivity change and its saturation behavior upon increasing the excitation fluence are consistent with the PI CDW-M phase transition.

From the rise-time of the reflectivity transient it also follows that this transition happens on the 100 fs timescale after photoexcitation (rise-time is becoming shorter upon increasing F). The initial decay time, τ_1, shows a pronounced increase near the threshold fluence, followed by a rapid drop as shown in inset to Figure 4.7 (the secondary decay time τ_2 shows only a slight decrease upon increasing F). This critical slowing down of relaxation below the threshold for the CDW melting shows similar behavior as in the weak perturbation limit upon increasing the temperature towards T_c^{3D} as shown in Figure 4.3.

Additional support to the assignment of the saturation behavior to the PI CDW-M transition comes from the study of the oscillatory response, shown in Figure 4.8. Here clear suppression of the AM, which presents a fingerprint of the CDW state, is observed at comparable fluences. Figure 4.8 shows the 2 dimensional surface plot of the FFT spectrum of the oscillatory signal as a function of excitation intensity over several orders of magnitude. Several sharp lines are observed, the strongest being that of the AM at about 1.68 THz (56 cm^{-1}). The two second strongest modes at 2.25 THz (74 cm^{-1}) and 2.55 THz (85 cm^{-1}) correspond to zone-folding modes [76, 82]. Several weaker phonons in the 3-5 THz range are also observed as in Raman [82], as well as the weak side modes in the vicinity of the AM and the two zone-folding modes.

While Figure 4.8 clearly shows strong suppression and increased damping of the AM above $F \approx 200$ $\mu\mathrm{J/cm}^2$, suppression of other phonons follow at the excitation densities that are about one order of magnitude higher in F. More information about the nature of the PI CDW-M phase transition can be gained by looking at the evolution of the FFT spectrum with time at different F, which can be obtained by performing the Wigner transform. In this technique one performs FFT in a limited time window at a certain

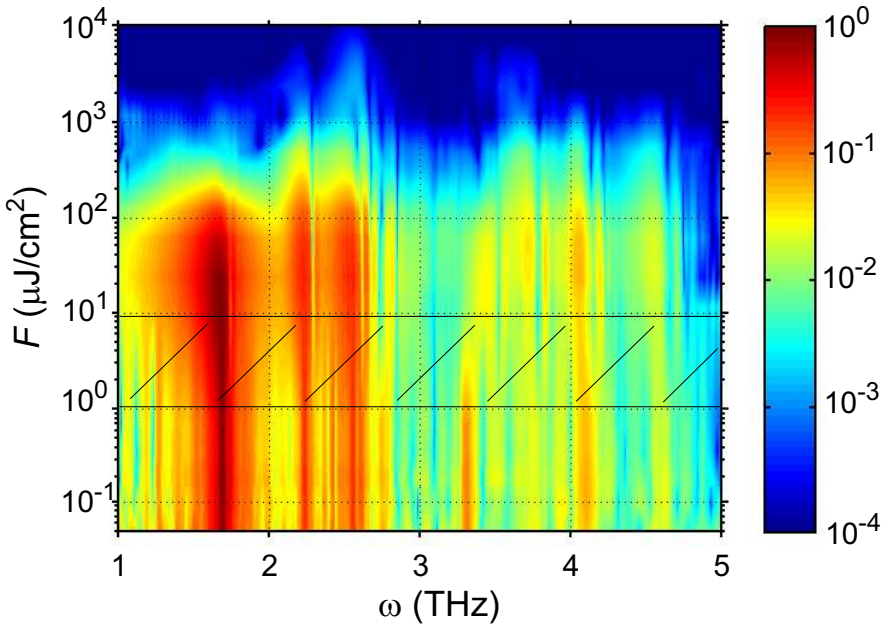

FIGURE 4.8: F-dependence of the Fourier transform of the oscillatory signal at 4 K. The data were, prior to FFT analysis (time window of 50 ps), normalized to F for clarity. The area between 1.1 and 9 μJ/cm^2 is obtained by interpolation between the low F data recorded with the Ti:sapphire oscillator and the data recorded with the amplified system. Color coding represents the FFT amplitude. Strong suppression of the AM ($\approx$ 1.68 THz) is observed at $F \approx 200$ μJ/cm^2, while the other modes vanish at fluences that are about one order of magnitude higher.

time point. Choosing an appropriate integration window is very important since a short (long) integration window means good (poor) time resolution but poor (good) frequency resolution. The spectra for four different fluences are presented in Figure 4.9. Here one clearly sees that the AM vanishes at $F \gtrsim 300$ μJ/cm^2 while the two zone-folding modes persist up to $F \gtrsim 2.5$ mJ/cm^2 finally disappearing above $F \gtrsim 3$ mJ/cm^2. The fact that high frequency modes survive above the threshold fluence for the PI CDW-M phase transition suggests that on a short timescale time following the PI CDW-M transition and subsequent recovery on the sub-ps timescale (inset to Figure 4.7) the lattice remains largely unperturbed. In other words, photoexcitation with a 50 fs optical pulse of $F > F_{sat}$ induces melting of the electronic density modulation, which partially recovers on the sub-ps timescale, while the lattice is - on this timescale - uncoupled from the electron subsystem and retains its $2k_F$ modulation. Only in the second step of relaxation, which proceeds on the 10 ps timescale, the CDW can be described with a single order parameter where electrons adiabatically follow the lattice.

We have studied the F-dependence of the amplitude of the electronic signal at different temperatures below T_c^{3D} and we present the results in Figure 4.10. Upon increasing the temperature, saturation appears at decreasing values of F. In order to determine

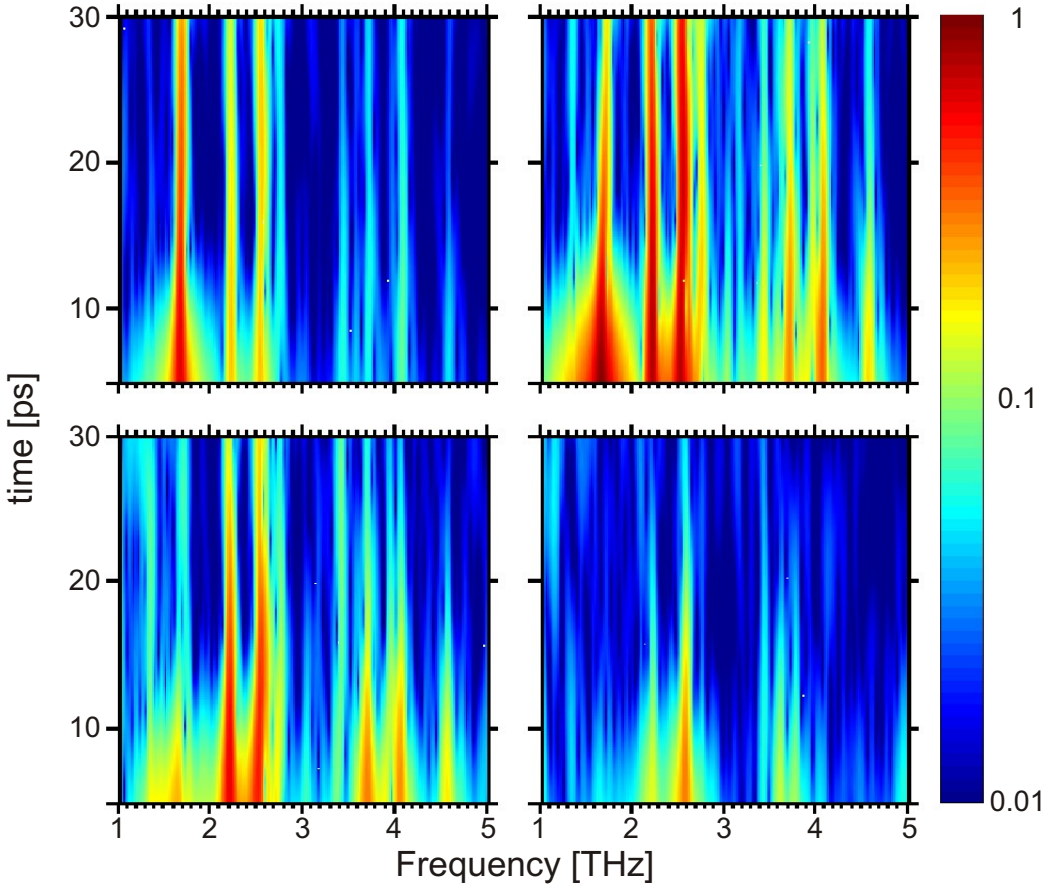

FIGURE 4.9: The time evolution of the FFT spectrum at 4K recorded at $F = 12$ μJ/cm^2, 130 μJ/cm^2, 0.38 mJ/cm^2 and 2.5 mJ/cm^2 (panels a-f). The plots are obtained by time-windowed FFT analysis with a 10 ps Gaussian time window. The AM is strongly suppressed at $F \geq 200$ μJ/cm^2, while the high frequency modes are present up to $F \approx 3$ mJ/cm^2.

the temperature dependence of the saturation fluence, F_{sat}, we fit the data with the simple saturation model, which is described in detail in Section 3.2.1. The temperature dependence of F_{sat}, together with the corresponding absorbed energy density per unit cell volume[5], E_{sat}, is presented in Figure 4.10b. To find whether the CDW melting is a result of a simple pulsed heating or is it non-thermal in origin we calculated the expected temperature rise ΔT which corresponds to E_{sat}, using $E_{sat} = \int_{T_0}^{T_0+\Delta T} c_p(T)dT$. Here c_p is the total specific heat [57]. At $T_0 = 4$ K and $E_{sat} \approx 60$ meV/u.c.v. we obtain $\Delta T \lesssim 40$ K, while at higher T_0 this value is considerably smaller ($\Delta T \lesssim 3$ K at 172 K and $E_{sat} \approx 20$ meV/u.c.v.). In fact, the absorbed energy density required to heat $K_{0.3}MoO_3$ from 4K to its phase transition $T_c^{3D} = 183$K is about 600 meV/u.c.v., an order of magnitude higher than E_{sat}. It follows that the PI CDW-M phase transition is non-thermally driven.

[5]Absorbed energy density is calculated using published values [81] of the dielectric constant at 1.55 eV.

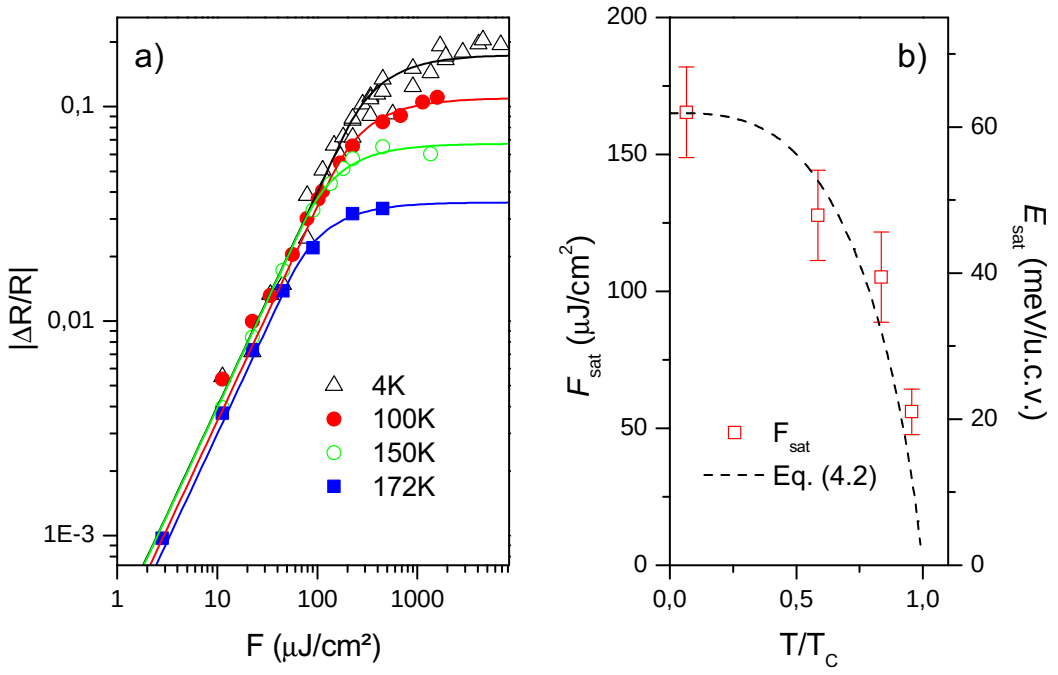

FIGURE 4.10: a) F-dependence of the PI reflectivity maximum at several temperatures below T_c^{3D}. The solid lines are fits with the simple saturation model [28]. b) Saturation fluences extracted from a) and the corresponding absorbed energy densities in meV per unit cell volume. The dashed line represents the calculated T-dependence of E_{sat} given by Eq.(1), where BCS T-dependence of Δ was used.

Observation of coherently excited zone-folded modes at fluences up to one order of magnitude higher than F_{sat} suggests, that on the sub-ps timescale after photoexcitation, the electrons are nearly uncoupled from the lattice. In this case E_{sat} should be compared to the energy gain of the electronic subsystem upon CDW condensation, E_{el}. To estimate E_{el} we used the mean-field expression in the weak coupling limit, given by Equation 2.20

$$E_{el} = -n(\epsilon_F)\Delta^2 \left(\frac{1}{2} + \log \frac{2\epsilon_F}{\Delta} \right). \tag{4.2}$$

Here $n(\epsilon_F)$ is the normal state density of states at the Fermi energy, ϵ_F, and Δ is the value of the CDW gap. Using $\Delta = 60$ meV, $\epsilon_F = 0.24 - 0.39$ eV and $n(\epsilon_F) = 4 - 6$ eV^{-1}/u.c.v. [60, 120] we obtain $E_{el}(4\text{K}) = 37 - 66$ meV/u.c.v.. This value is in excellent agreement with $E_{sat}(4\text{K}) \approx 60$ meV/u.c.v., giving further support to the argument that during PI CDW melting the electronic order parameter is decoupled from the lattice on the sub-ps timescale. At $F \gtrsim 3$ mJ/cm^2, which corresponds to the absorbed energy density of 1 eV/u.c.v., other modes are also completely suppressed. This energy density is in good agreement with the calculated energy density required to heat up the excited volume to above T_c^{3D}. In this regime, recovery proceeds on a much longer timescale which is determined by heat diffusion out of the excited volume. The temperature dependence

of E_{sat}, shown in Fig. 4b, shows good agreement with the expected T-dependence of E_{el}. The dashed line in Fig. 4b shows $E_{el}(T)$ calculated from Eq.(1), where the BCS T-dependence of Δ was used [60].

By using the fast scanning technique, we were able to significantly improve the signal to noise ratio (compared to the measurements in the low perturbation regime). This enabled us to monitor the evolution od the oscillatory response in great detail even several hundreds of picoseconds after excitation. After subtracting the exponential part of the signal, we performed a Fast Fourier Analysis on the remaining oscillatory signal and we show the result in Figure 4.11 together with a Raman spectrum for comparison [82].

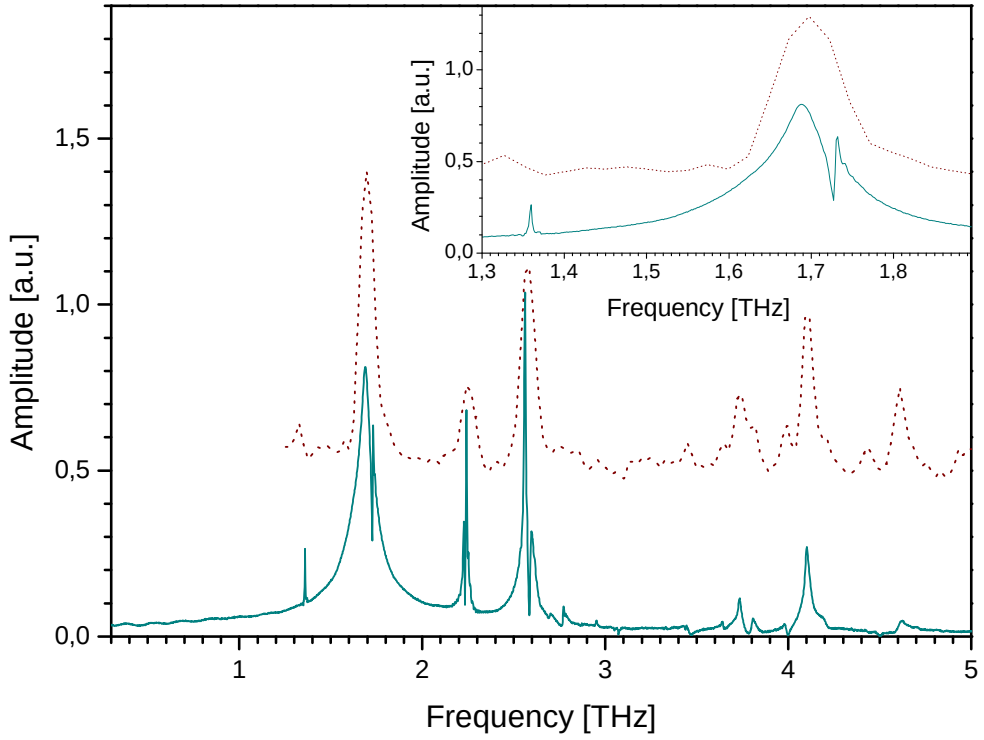

FIGURE 4.11: This figure shows a comparison of the high resolution FFT obtained by our method (solid line) and a Raman spectrum [82] (dotted line) of a $K_{0.3}MoO_3$ crystal. The spectra are offset for clarity. The inset shows a blowup of the data close to the amplitude mode frequency.

As has been shown previously [23, 41], there is good agreement between the Raman spectrum and the FFT spectrum of the oscillatory part of the signal. It is worth mentioning that the frequency resolution of our method is roughly one order of magnitude better than the frequency resolution of the Raman measurement (see Figure 4.11) Of special interest to us are the the amplitude mode at 1.68 Thz and the two zone folding modes at 2.24 THz and 2.56 THz [76, 82] because they are the fingerprints of the CDW. Our measurements show for the first time that all of these modes are split. While all the

zone folding modes have similar linewidths, the two modes at 1.68 THz clearly show very different damping at first glance. To analyse this behavior in more detail, we calculated the time evolution of the oscillatory response (see Figures 4.12 and 4.13).

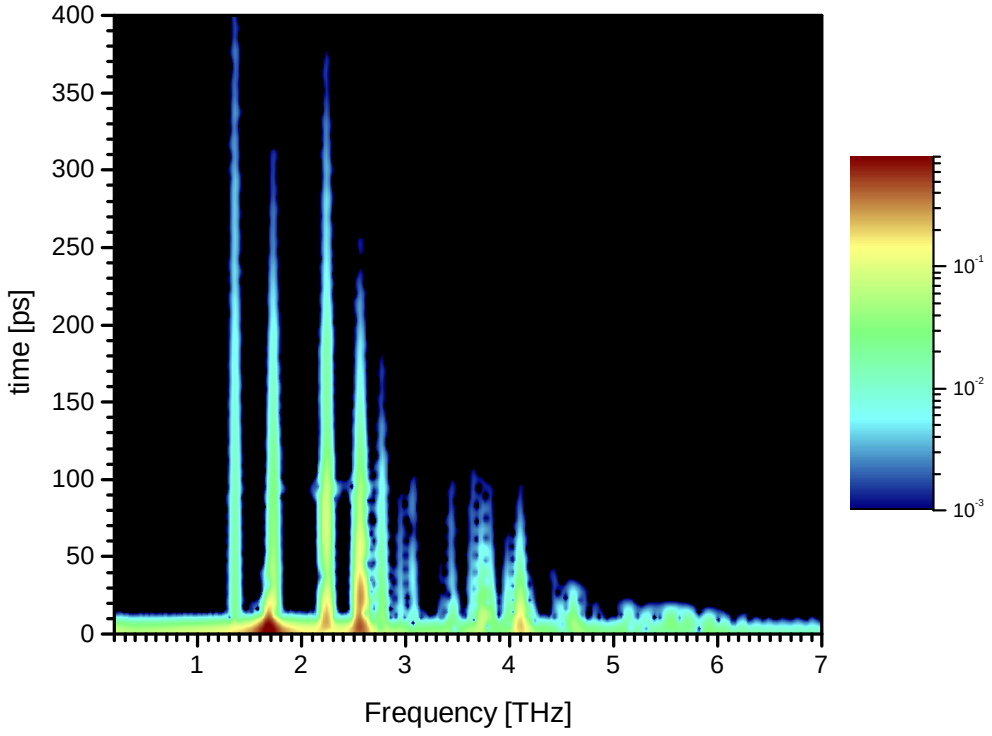

FIGURE 4.12: This figure shows how the FFT spectrum of the oscillatory response evolves 400 ps after the excitation pulse. The FFT spectra were obtained using a moving Gaussian FFT window. The full width at half maximum of the Gaussian window was 10 ps.

In Figure 4.12 we plot the time evolution of the FFT spectrum that was obtained by integrating the data with a 10 ps Gauss window. One can easily see that the amplitude mode and both zone folding modes are clearly visible even more than 200 ps after excitation. Due to the short integration window the peaks are no longer split, however a beating effect is observable in the zone folding modes. To estimate the evolution of the modes quantitatively, one can plot the time evolution of their amplitude (see Figure 4.13).

In Figure 4.13 we plot the time evolution of the amplitudes of the amplitude mode (Figure 4.13a) and the two zone folding modes (Figures 4.13a and 4.13b). The data are plotted on a semi-logarithmic scale to emphasize their exponential behavior. In an effort to exclude any artifacts due to the integrating procedure, we performed the FFT with different time windows (2.5 ps and 5 ps) but one can see that the data match very well. The temporal dependence of the amplitude of the amplitude mode in Figure

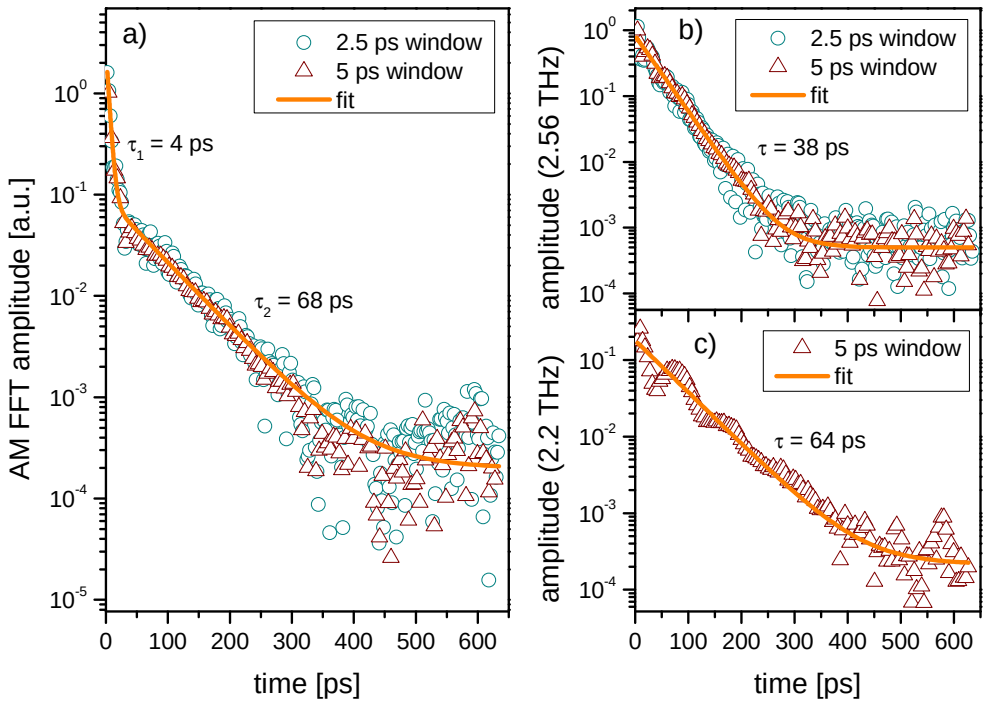

FIGURE 4.13: The temporal evolution of the amplitudes of three different peaks obtained from the Wigner transform (see Figure 4.12). The frequencies are chosen to analyze the behavior of the amplitude mode and two zone-folding modes. The beating effect observable in all amplitudes indicates that each of the peaks describes two modes with similar frequencies. The amplitude of the AM peak can be fitted with a double exponential indicating that the two modes have very different damping. The amplitudes of the two zone-folding modes can be fitted with a single exponential indicating that the damping of the double modes is similar.

4.13a clearly displays two distinctive decay times. By fitting the data with a double exponential function (solid line in Figure 4.13a) we find the two decay times to be 4 ps and 68 ps, which corresponds to the line widths of the two modes shown in Figure 4.11. The decay times of the amplitudes of the 2.2 THz and 2.5 THz zone-folding modes show single exponential decay behavior with decay times of 64 ps and 38 ps, respectively. This is the expected result since the linewidths of the split zone folded modes shown in Figure 4.11 are similar. The zone folding modes also clearly display beating with the characteristic time that corresponds to the inverse of the difference of the frequencies of the split modes.

To further elucidate the phonon behavior, we plot the temperature evolution of the FFT spectrum in Figure 4.14. One can see that substantial softening when approaching the transition temperature is only observable in the amplitude mode at 1.68 THz. Figure 4.14b is a blowup of the spectrum around the amplitude mode where one can clearly see another narrow mode on top of the amplitude mode (also see the inset in Figure 4.11). When looking at the FFT spectrum at a single temperature (Figure 4.11), one is tempted to somehow ascribe the narrow mode to the amplitude mode due to very similar

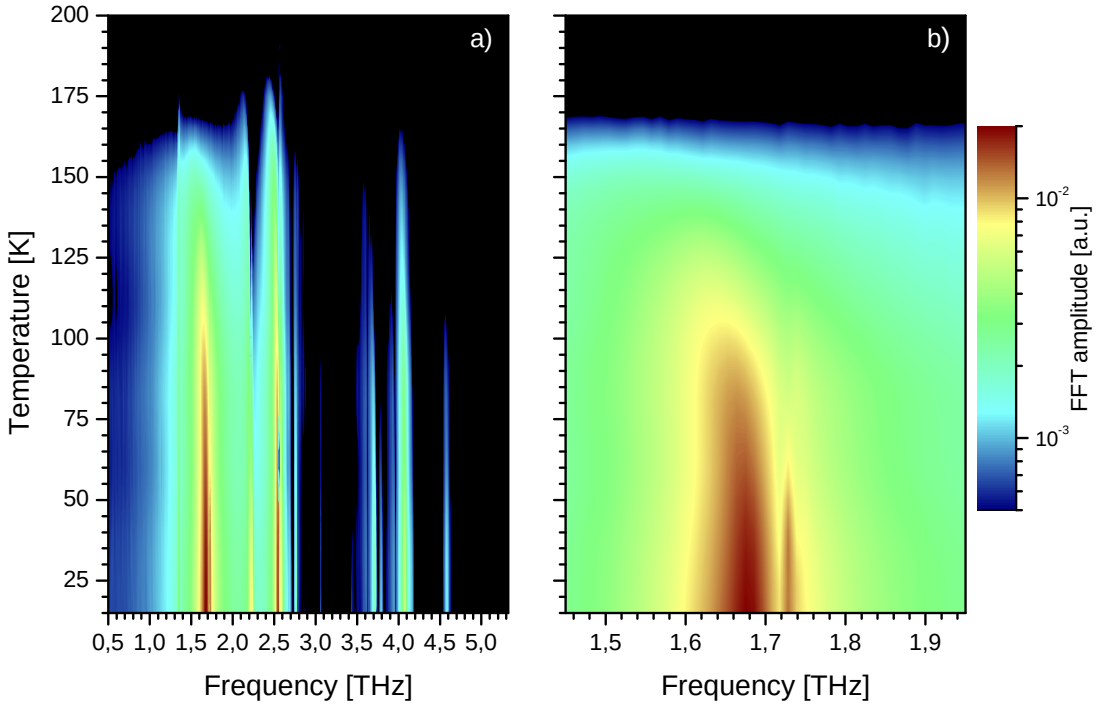

FIGURE 4.14: The temperature dependence of the FFT spectrum on two different frequency ranges. b) is a blowup of a) near the amplitude mode showing two distinct modes. The stronger mode at $\nu_1 = 1.68$ THz softens considerably when approaching the transition temperature while the frequency of the weaker mode at $\nu_2 = 1.73$ THz slightly increases.

frequency (e.g to the surface AM mode). However if that was true one would also expect observable softening of that mode with increasing temperature which is clearly not seen in Figure 4.14b.

4.4 Thin Films

4.4.1 Introduction

In this Section we will start with the motivation for growing thin films and continue with our advances in growth and characterization of thin films of $K_{0.3}MoO_3$.

Thin films have proven to be much better suited for certain *pump-probe* techniques than crystals of the same material. The advantages of thin films over crystals include a relatively large sample surface with low surface roughness, small PI steady state heating[6]

[6]In the first approximation ΔT is proportional to the inverse of the thermal conductivity of the substrate which is usually chosen to offer much better thermal conductivity than the measured sample.

and the possibility to measure in transmission. For configuration example, when the *terahertz pump-probe* technique is used, the sample under investigation is perturbed with an IR pulse and probed with a THz pulse. The *terahertz pump-probe* measurements are significantly simpler in transmission mode, a large surface area of a sample is needed due to the large wavelength of the THz radiation and we have also discovered in our preliminary measurements that sample heating can be substantial. Therefore, thin films clearly present a better alternative than crystals for this technique. The main motivation for using this method lies in the fact that the frequency of the infrared active phase mode (see Section 2.5 for more details about the phase mode) in $K_{0.3}MoO_3$ lies in the low THz frequency range ($\nu \approx 0.3$ THz [76]) making a THz *probe* susceptible to directly detect it[7]. Another technique, where thin films are needed due to small penetration depth of electrons, is *ultrafast electron diffraction* (UED), which has been used to follow the temporal evolution of laser induced melting in thin metal films [7, 121] on a ps time-scale [122]. The method harbors great promise for resolving the fastest chemical processes with atomic level detail, however it suffers from relatively poor temporal resolution of several 100s fs due to the propagation dynamics of an electron pulse [9]. Free standing films are required for UED so ideally the films would be deposited on a substrate that could later be removed. For example, if one could deposit films on salt (NaCl), the substrate could be dissolved without damaging the film, so a free standing film would be obtained.

Another reason that makes thin films compelling in general is that when the coherence length of the electrons is of the order of the system size or smaller, deviations from the bulk behavior sometimes occur. Classical theories can no longer adequately describe such systems, and the wave-like nature of the electrons has to be taken into account. The study of such electron systems with dimensions between roughly 10 nm and 10 μm is called mesoscopic physics. For instance, the Aharonov-Bohm effect [123] is a well known example which can be demonstrated in small metallic rings placed in a magnetic field [124]. If the ring circumference is smaller than the coherence length of the electron phase, electron-wave interference causes oscillations of the magnetoresistance that can be experimentally verified. The first such experiment on a CDW material was reported in 1997 [125]. An irregular array of small columnar defects was created in a $NbSe_3$ crystal by irradiation with high energy ions. Electrical transport measurements on this geometry showed a periodic oscillation of the magnetoresistance which the authors ascribed to an Aharonov-Bohm like quantum interference effect. The authors also suggested that the half flux periodicity $h/2e$ of the oscillation may be a sign of macroscopic tunneling of the CDW. An alternative theoretical explanation has also been proposed where the observed periodicity arises from ensemble averaging properties [126].

[7] So far we were unable to detect the phase mode directly using IR wavelength.

Several different characteristic lengths can be defined in CDW systems (see Section 2.4), however only the correlation and coherence lengths parallel to the chain direction are usually considered for finite size samples because the characteristic lengths are usually at least one order of magnitude smaller in the transverse directions. The correlation length l_ϕ denotes the distance over which the CDW phase is coherent, in other words the average domain size. It depends strongly on the impurity concentration (CDW pinning potential) of a particular crystal. X-ray studies on $K_{0.3}MoO_3$ have shown that l_ϕ can be as large as several micrometers [127]. The coherence length ξ determines the typical distance over which the amplitude of the CDW modulation can be changed. Within the frameworks of the BCS theory, ξ is given by

$$\xi(T) = \frac{\hbar v_F}{\pi \Delta(T)}, \tag{4.3}$$

where v_F is the Fermi velocity and $\Delta(T)$ is the Peierls gap. Using the values from the literature for v_F and $\Delta(0)$ in $K_{0.3}MoO_3$ [60], $\xi(0) \approx 1$ nm. Near the transition temperature, $\xi(T)$ diverges.

4.4.2 Growing Thin Films

We have used pulsed laser deposition (PLD) for the growth of $K_{0.3}MoO_3$ thin films. The technique can be used to grow thin films of several types of materials, including semiconductors, ferroelectrics and high-T_c superconductors [128]. All depositions were performed onto substrates of (510)$SrTiO_3$ (STO) and (1-102)Al_2O_3 (sapphire). A schematic drawing of a PLD setup is presented in Figure 4.15. A laser pulse ablates material off a polycrystalline target material creating a plasma plume. The particles contained within the plasma plume are deposited on the substrate. The stoichiometry and morphology of the deposited film strongly depends on the thermodynamic conditions during film growth. The most important parameters include the substrate temperature, the oxygen pressure in the chamber and the deposition rate.

$K_{0.3}MoO_3$ films can only be grown in a small range of various growth parameters [129]. The temperature window is roughly between 350°C and 500° and the oxygen pressure is approximately 0.1 mbar. The grown films are found to be granular. We have obtained grain sizes of up to ≈ 1 μm whereas the grain sizes reported in literature are as large as 10 μm with chain direction along the substrate plane [129, 130]. The largest grains are grown at high temperatures and low repetition rates.

After the films were deposited, we used several techniques to characterize their quality. Our first benchmark was to use a UV-vis spectrometer to measure the transmission

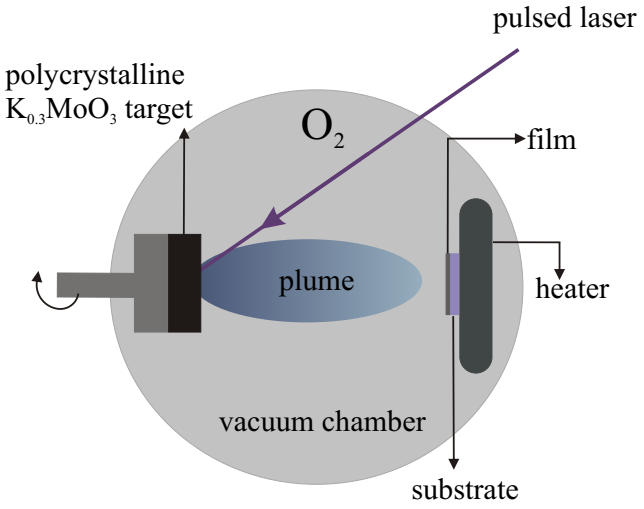

FIGURE 4.15: The schematic of the pulsed laser deposition setup. The target and the substrate are placed into a vacuum chamber where oxygen pressure can be suitably controlled. A pulsed KrF excimer laser (model COMPexPro 205 from Lambda Physics Coherent) is used to create plasma plume by ablating material off a rotating polycrystalline target. Film growth is caused when the plasma plume deposits the particles on a substrate which is mounted on a heater block opposite the target.

spectra of the films (see Figure 4.16), which was performed immediately after film deposition. We compared the measured data with the spectra calculated for various films thicknesses (see Figure 4.16). In calculation, we used ϵ_1 and ϵ_2 obtained by Kramers-Kronig analysis [131] of the published data of $R(\omega)$ [54]. We extrapolated the reflectivity data in the low and high frequency regime using Hagen-Rubens and $1/\omega^4$ dependency [131], respectively. There was good qualitative agreement between the calculated and measured spectra (see Figure 4.16) and we were also able to estimate the thickness of films to be approximately 100 nm – 200 nm from the absolute value of transmission.

In the second stage of characterization, the films were further analyzed using the atomic force microscopy (AFM) (see Figure 4.17), low angle X-ray diffraction (XRD) (see Figure 4.18) and by measuring their DC resistivity (see Figure 4.19). Let us begin with the summary of the AFM measurement which was performed with a commercially available atomic force microscope (Nanoscope Dimension DI3100 with Nanoscope IV controller from Veeco Instruments) at the Jožef Stefan Institute. The measured surface of a film on sapphire (see Figure 4.17a) shows partial ordering of the elongated grains in two preferential directions on the surface. The average roughness of the film was below ≈ 50 nm with several large grains with dimensions of up to 100 nm. We have observed that the grains are larger and more common on the film edge than in the middle of the film. The AFM image of a thin film on STO is presented in Figure 4.17b. There was no

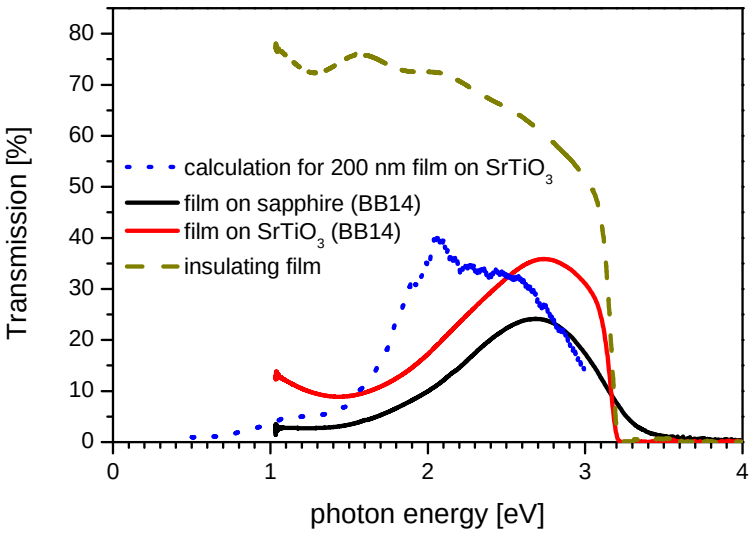

FIGURE 4.16: Transmission spectra of $K_{0.3}MoO_3$ films on STO and sapphire substrates measured at room temperature are plotted together with a calculated transmission spectrum for a 200 nm film on STO substrate (dotted line) and an insulating film that was grown at a too high substrate temperature.

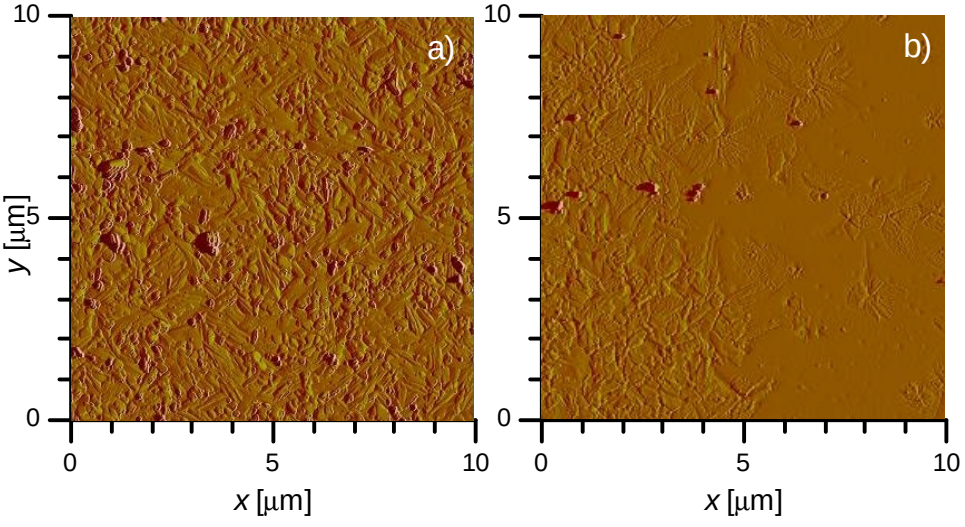

FIGURE 4.17: The AFM image of a $K_{0.3}MoO_3$ film on sapphire (a) shows partial ordering of the elongated grains in two preferential directions on the surface. The average surface roughness is below $\approx$ 50 nm with several large grains with dimensions of up to 100 nm. The AFM image of a $K_{0.3}MoO_3$ film on STO (b) shows no ordering on the surface. The film surface roughness is less than $\approx$ 10 nm.

ordering on the surface. The film surface roughness is less than ≈ 10 nm with several isolated ≈ 50 nm high grains.

The low angle XRD investigations were performed at the Research Center for Advanced Materials at University of Pitesti by Sorin Moga, Denis Negrea and Catalin Ducu. The data acquisitions were carried out with a Rigaku Ultima IV diffractometer at room temperature. For the thin films analysis, we used a vertical powder goniometer in parallel beam geometry (with cross beam optics) and a multipurpose thin film attachment. The Peak/Background ratio was improved by a flat graphite monochromator. The incident Cu-K_α radiation, $\lambda = 1.54178$ Å was used. The typical experimental conditions were: 40 kV, 30 mA, 2 s for each step, angular range $2\theta = 70°$–$420°$ and angular step $0.050°$. In order to maximize the X-Ray path length on the sample surface, the incidence angle was kept constant at $\alpha = 10°$. The results are presented in Figure 4.18. A comparison with the spectrum obtained on a crystalline powder sample reveals varying results on different films with 3 qualitatively different outcomes marked with different colors in Figure 4.18. a) There was good matching between the film and powder spectrum (see Figure 4.18a), meaning that there was no preferable direction for crystal growth on the substrate surface. b) There was no matching of any of the peaks (see Figure 4.18b) which was observed on the samples that were already ruled out due to being very transparent (other films were visibly dark). c) There was limited matching between the film and crystal spectrum (see Figure 4.18c and 4.18d), which can be expected for epitaxial growth of films. This was also the most common result for the films that were determined to consist of $K_{0.3}MoO_3$ using other characterization techniques.

The transport measurements were performed at the Jožef Stefan Institute using a two contact technique and a Keithley 238 multimeter. The temperature dependency of the resistivity of a crystal and two films on different substrates is presented in Figure 4.19. Since the measurement was performed with only two contacts, the metallic behavior of the crystal above T_c^{3D} is not observed however the kink at the transition temperature is clearly visible. A qualitatively similar behavior is observed on the film grown on sapphire although the transition temperature is not as clearly defined as in the crystal. One can also notice the much higher absolute value of the film resistivity which can be attributed to the small film thickness. The film on STO shows no anomalous behavior in resistivity in the temperature range from 60 K – 300 K and seems to be a relatively good electrical insulator. Both films were shown to form CDW domains below 183 K using femtosecond spectroscopy (the details are described in the next section) which leads us to conclude that by measuring the transport measurements of thin films one can show that a CDW is formed, however if the result is negative, additional characterization is needed.

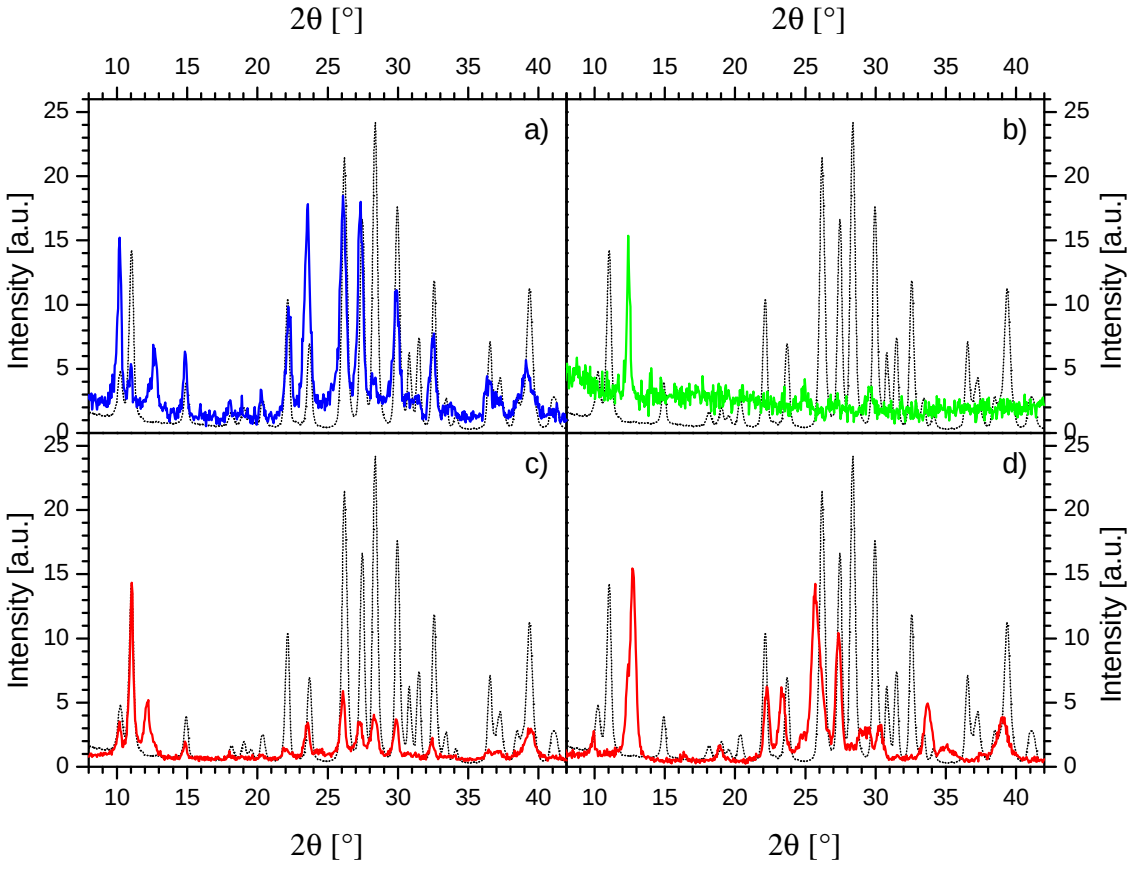

FIGURE 4.18: Several spectra of $K_{0.3}MoO_3$ films obtained by low angle XRD (solid line) are compared to the spectrum of a crystalline powder obtained by the same method (dotted line).

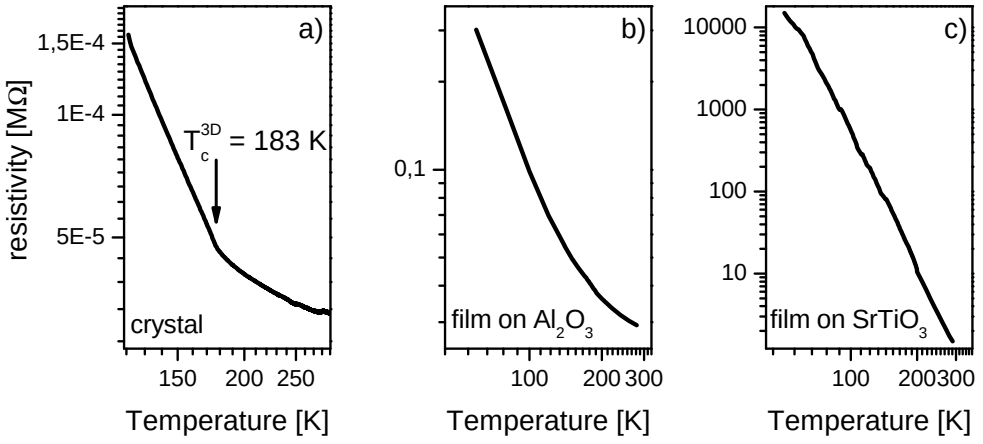

FIGURE 4.19: Transport measurements on a $K_{0.3}MoO_3$ crystal (a) are compared to the transport measurements on $K_{0.3}MoO_3$ films on Al_2O_3 (b) and $SrTiO_3$ (c) substrates. The measurements were performed using a two contact method so the metallic behavior in crystal is not observed above T_c^{3D}.

The results of these characterization investigations were not entirely conclusive since the results of different methods on a single film did not always yield the same result. However we concluded that there were enough good indications that we successfully managed to produce thin films containing $K_{0.3}MoO_3$, so the decision was made to further examine several best quality films[8] using *femtosecond pump-probe spectroscopy*.

4.4.3 Femtosecond Spectroscopy on Thin Films

The data presented in this section have been measured at the Konstanz University using the fast scanning technique that is described in detail in Section 3.1.3. We used 40 fs laser pulses at 1.55 eV (λ = 800 nm) from a regenerative amplifier with a repetition rate of 250 kHz as a source of both photoexcitation (*pump*) and *probe* pulse trains (see Section 3.1.3). The experiments were performed on four different thin films of $K_{0.3}MoO_3$. The *pump* and *probe* were cross-polarized. Polarization dependent measurements on all films showed that the PI signal was unchanged for different *probe* polarizations. The *pump* and *probe* beams were focused onto the sample with diameters of $d_{pump} = (90 \pm 4)$ μm and $d_{probe} = (45 \pm 2)$ μm. The samples were mounted in an optical cryostat and the temperature was varied between 4 and 300 K using liquid helium as a cooling agent. The temperatures were measured at the cold finger of the cryostat.

The PI signal in all the investigated films is qualitatively similar so only the data obtained on one $K_{0.3}MoO_3$ film on Al_2O_3 substrate will be presented here. We plot the temperature dependence of the PI reflectivity change as a function of temperature and time after photoexcitation in Figure 4.20a. The $\Delta R/R$ relaxation of thin films and bulk looks qualitatively similar (see Figures 4.2 and 4.7), however a) the diminished amplitude and increased damping of the oscillatory signal in thin films is very apparent and b) the amplitude of the electronic part of $\Delta R/R$ is about one order of magnitude lower than in the crystal (see Figures 4.7 and 4.20a) even though the films are optically thick.

The non-oscillatory part of the data was found to fit well to a sum of three exponential functions with well separated decay times in the whole temperature range.

$$S(t) = A_1(t)e^{-t/\tau_1} + A_2(t)e^{-t/\tau_2} + A_3(t)e^{-t/\tau_3} \tag{4.4}$$

The largest decay time τ_3 is of the order of 400 ps and since the whole time-window of measurement was only 100 ps, τ_3 was fixed to a constant value of $\tau_3 = 400$ ps. We plot the temperature dependence of the signal amplitudes A_1, A_2, A_3 and the two relaxation times τ_1, τ_2 in Figure 4.21. The relaxation time τ_2 shows similar temperature behavior

[8] We investigated films on both substrates.

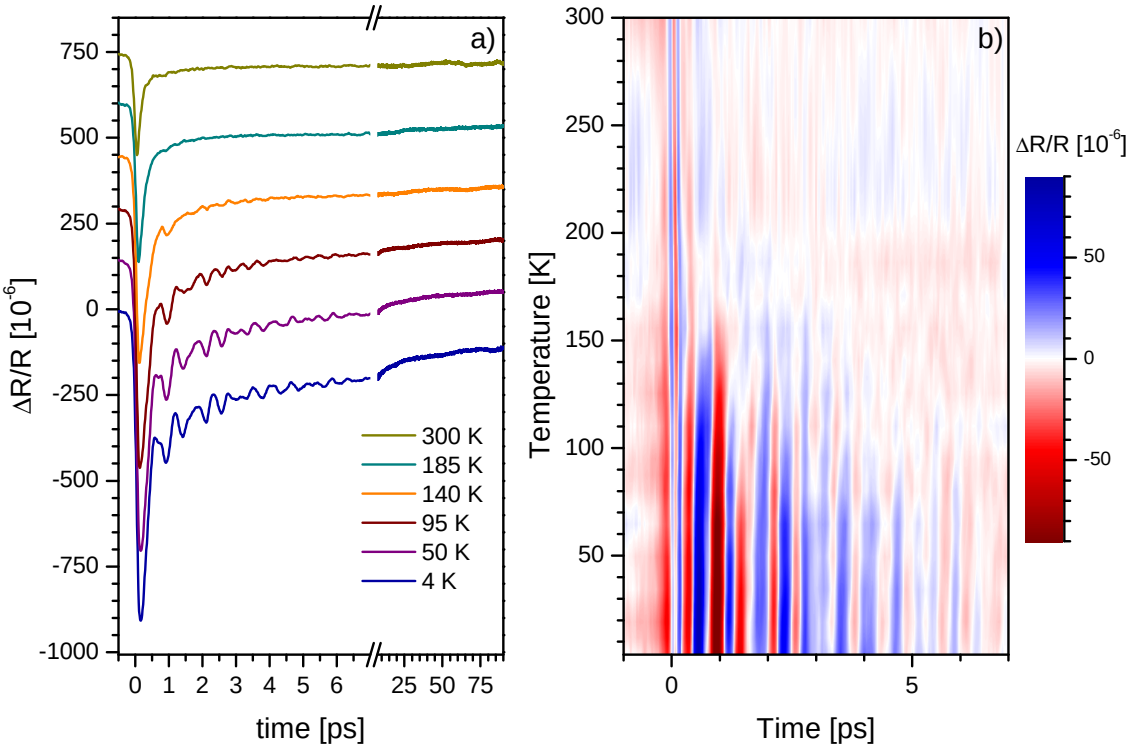

FIGURE 4.20: a) PI reflectivity changes in a $K_{0.3}MoO_3$ film on Al_2O_3 substrate as a function of temperature and time after photoexcitation. Here the *pump* pulse train with average power $P = 1$ mW and repetition rate $\nu = 250$ kHz was focused to $2\rho_{pump} = (90 \pm 4)$ μm corresponding to excitation fluence $F = 40$ μJ/cm^2. b) Oscillatory part of the PI $\Delta R/R$ as a function of temperature.

as in the crystal as it decreases with increasing temperature, however the anomalous slowing down near $T \approx 70$ K is not observed in the film (compare Figures 4.3 and 4.21b). The fast relaxation time τ_1 attributed to the relaxation of the QP across the gap increases by $\approx 10\%$ with increasing temperature as the transition temperature is approached from below. This is in contrast with the temperature dependence of τ_1 in the bulk where the relaxation time τ_1 increases by one order of magnitude from 4 K to the transition temperature T_c^{3D} (see Figure 4.3 and Ref. [23]). In short, there is no strong divergence in τ_1 at T_c^{3D} in films. Above the transition temperature, τ_1 abruptly decreases to approximately half of the low temperature value, which is in good accordance with the temperature behavior of τ_1 in crystal [23]. A very similar quenching of τ_1 divergence due to topology change has also been observed in $NbSe_3$ [39] which is a CDW material that crystallizes in whisker and ring crystals (see Figure 1.2). Shimatake et al. [39] offered an explanation of the τ_1 quenching in small ring crystals in terms of enhanced phase fluctuations in the closed-loop topology. Obviously, the same explanation can not be applied in the case of $K_{0.3}MoO_3$ films, however it does raise questions about how

finite size of CDW crystals affects the QP dynamics.

It was already mentioned that two characteristic lengths, the correlation and coherence length in the chain direction, should be considered and compared to grain sizes when investigating finite size effects in CDW films. Let us first consider low temperatures. The coherence length is $\xi \approx 1$ nm (see Equation 4.3), whereas the correlation length l_ϕ can be of the order of 1 μm in a crystal without any defects [127], therefore only the correlation length is of interest at low temperatures. Small grains act very much like a crystal with impurities, because in one case the CDW is pinned by domain walls and in the other case by impurities. It is obvious that stronger pinning affects the phase mode because CDW sliding is more difficult. However we can not offer a model to explain different dynamics of the electronic signal due to smaller correlation length. At temperatures near T_c^{3D} the correlation length strongly decreases and can not account for any mesoscopic effects. On the other hand, the coherence length is inversely proportional to the CDW gap so it strongly increases near T_c^{3D}. However since it is only of the order of 1 nm at low temperatures, one can expect the coherence length to only increase to several 10s of nm near T_c^{3D}, which is not even close to the size of the grains.

The residual oscillatory signal obtained as the difference between the raw data and the fit defined by Equation 4.4 is shown in Figure 4.20b. One can see that there is an oscillatory signal that vanishes as the transition temperature is approached from below. There is another strongly damped oscillatory signal that is present in the whole temperature range 30 K – 300 K . FFT analysis was performed in order to better evaluate the oscillatory signal. The spectra obtained below and above T_c^{3D} are plotted together with a spectrum obtained at 4 K in a crystal in Figure 4.22. The first and foremost observation is that there is good agreement between the low temperature spectra on film and crystal, as six strongest modes are observed in both film and crystal. One can also observe that the modes in the film are highly asymmetric and strongly damped. We attribute this to the finite grain size and inhomogeneity of the films, acting much like impurities in a crystal. We will test this hypothesis in future experiments by systematically introducing impurities into single crystals using irradiation and measuring the PI relaxation dynamics as a function of impurities concentration. The damping constant γ of the AM was obtained from the FFT spectra and its inverse value is plotted in Figure 4.21b. As has already been observed in the crystal (see Figure 4.3), it displays the same temperature dependence as the relaxation time τ_2. The only difference is that in film, both τ_2 and $1/\gamma$ follow the same temperature dependence in the whole temperature range 4 K – 180 K, whereas in the crystal this only happens when $T \geq 60$ K (see Figure 4.3). All the FFT spectra are plotted as a function of temperature in Figure 4.23, where one can see that the temperature dependency of the FFT measured on films and crystal are also very similar.

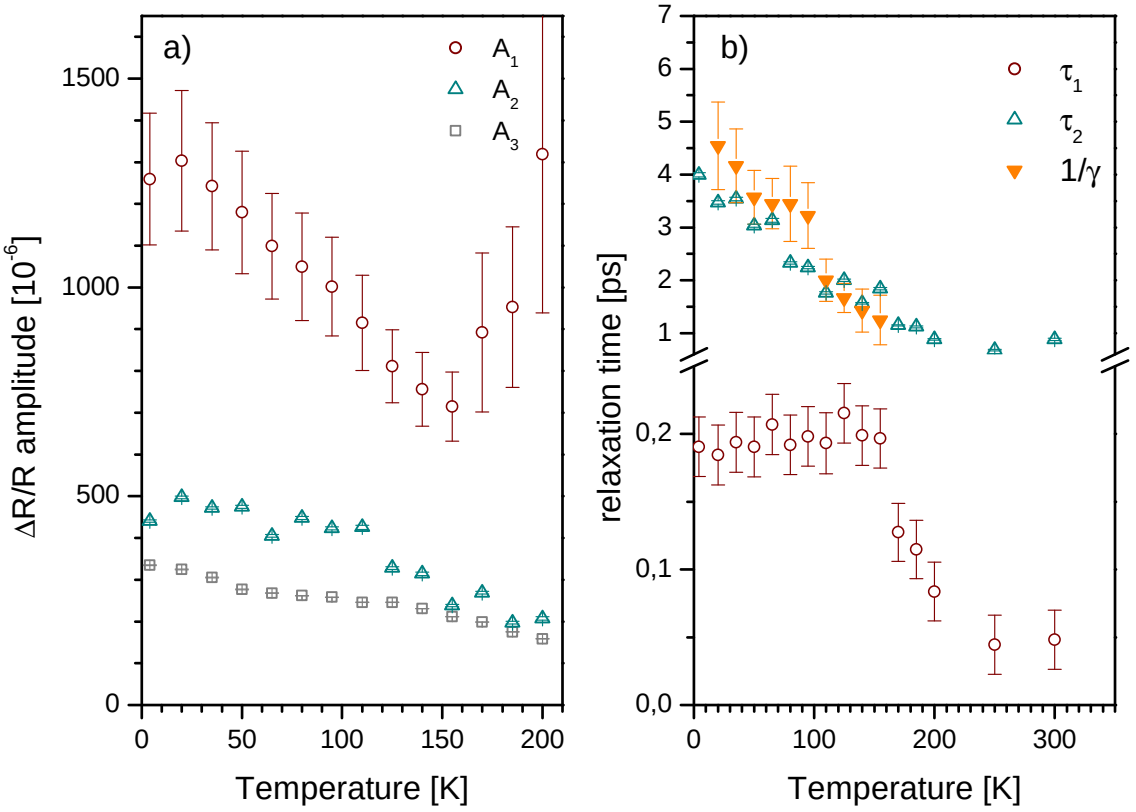

FIGURE 4.21: The temperature dependence of the PI signal amplitudes (a) and relaxation times (b) in $K_{0.3}MoO_3$ film on Al_2O_3 substrate. The relaxation time τ_3 is fixed to 400 ps. The decay time $1/\gamma$ of the AM is also plotted (full symbols) since it displays the same temperature dependence as τ_2.

In the second set of experiments we investigated the excitation fluence dependency of the PI signal at $T = 10K$. We plot the normalized $\frac{\Delta R/R}{F}$ transients as a function of excitation fluence F in Figure 4.24. The QP dynamics displays a visible change once the fluence is increased above $F \approx 300$ μJ/cm^2, which is equivalent to the fluence causing a dramatic change of the QP dynamics in single crystals (see Figure 4.7). The FFT spectrum of the oscillatory part of the signal is plotted in Figure 4.25. It also reveals a very similar picture as in the case of single crystals, where the AM is strongly quenched while the zone-folding modes persist even after the CDW condensate has been melted (see Figure 4.9).

The excitation fluence dependence of the amplitude A_1 of the 200 fs signal is presented in Figure 4.26a. For fluences $F \approx 300$ μJ/cm^2 – 1000 μJ/cm^2, A_1 increases linearly with F. We observed a signal with a similar amplitude and linear excitation fluence dependence above the transition temperature T_c^{3D} in crystal. It is therefore reasonable to assume that this linearly dependent component can be subtracted to obtain the saturation signal caused by CDW melting. The parameters of the linearly dependent signal are obtained by fitting the data above $F \approx 300$ μJ/cm^2 with a line (solid line in

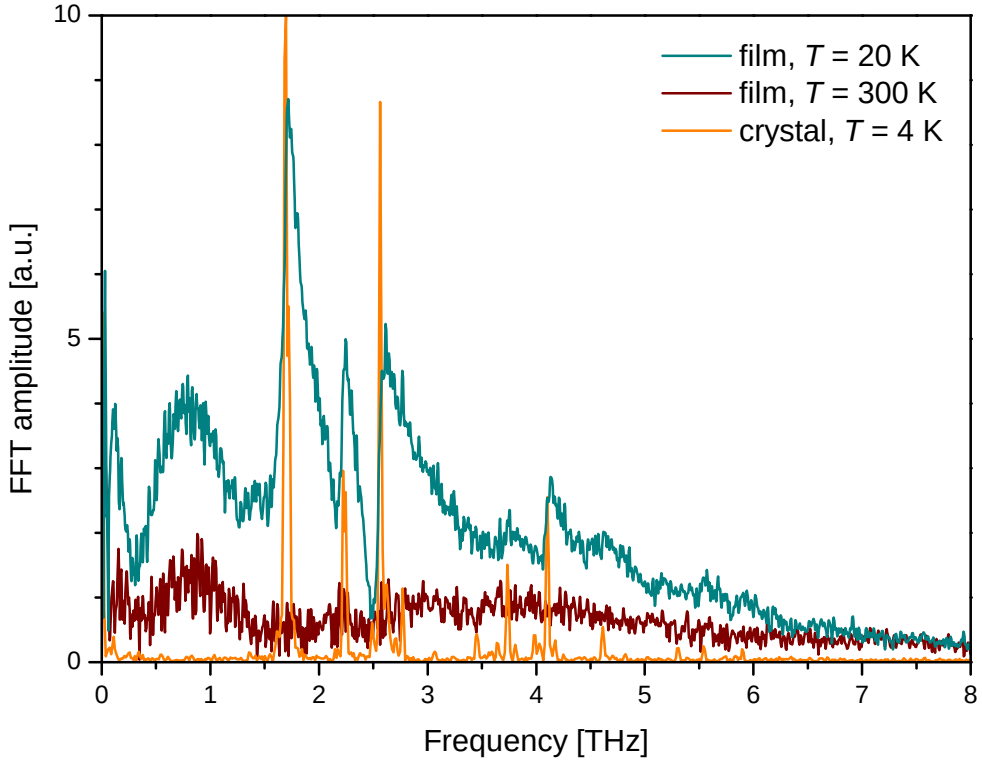

FIGURE 4.22: A comparison between the FFT spectra measured in a $K_{0.3}MoO_3$ crystal and film on Al_2O_3 substrate (below and above the transition temperature).

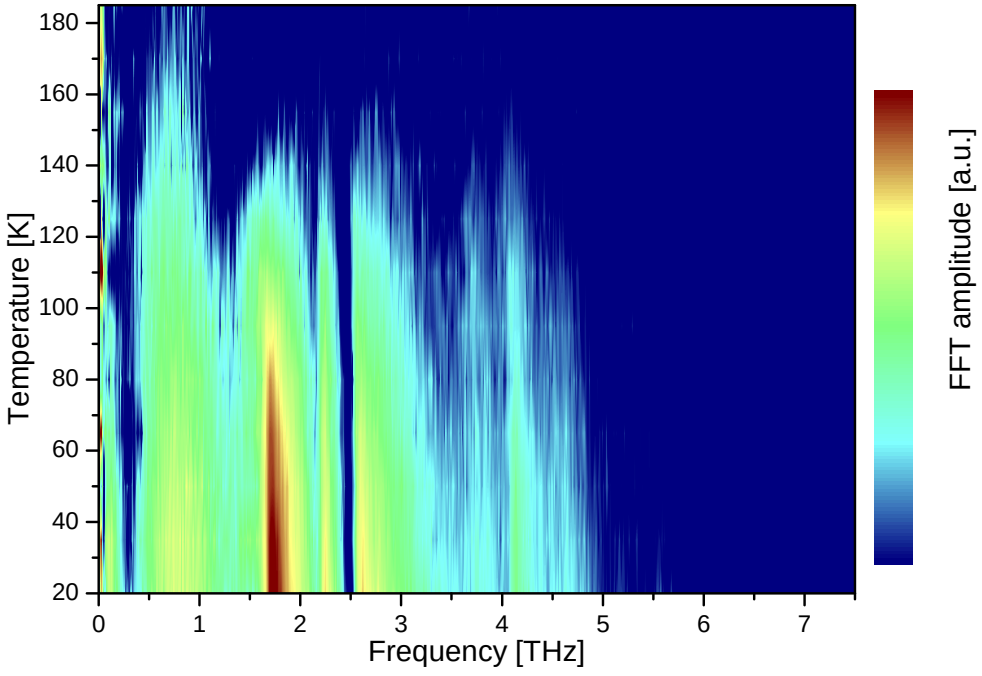

FIGURE 4.23: The temperature dependence of the FFT spectrum of the PI signal in a $K_{0.3}MoO_3$ film on Al_2O_3 substrate.

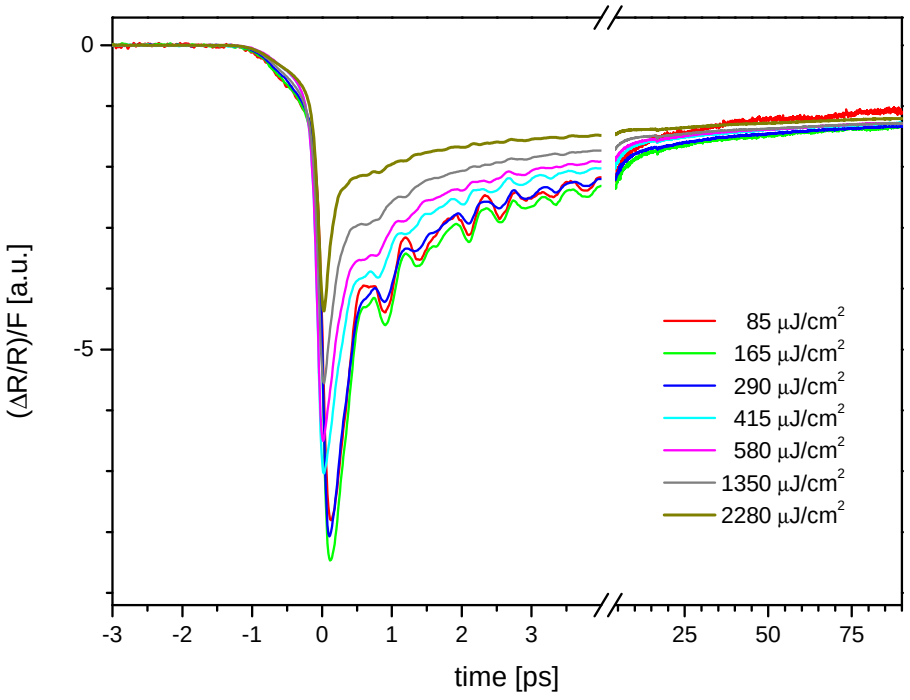

FIGURE 4.24: PI changes of reflectivity in a $K_{0.3}MoO_3$ film as a function of excitation fluence. Note that the transients have been normalized with the excitation fluence.

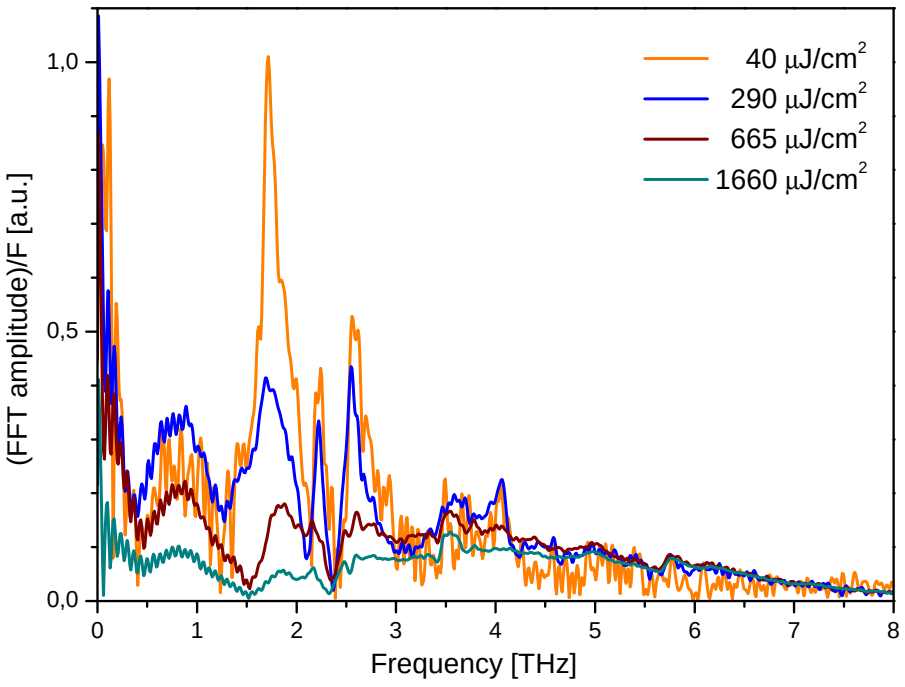

FIGURE 4.25: FFT spectra normalized to F in a $K_{0.3}MoO_3$ film as a function of excitation fluence.

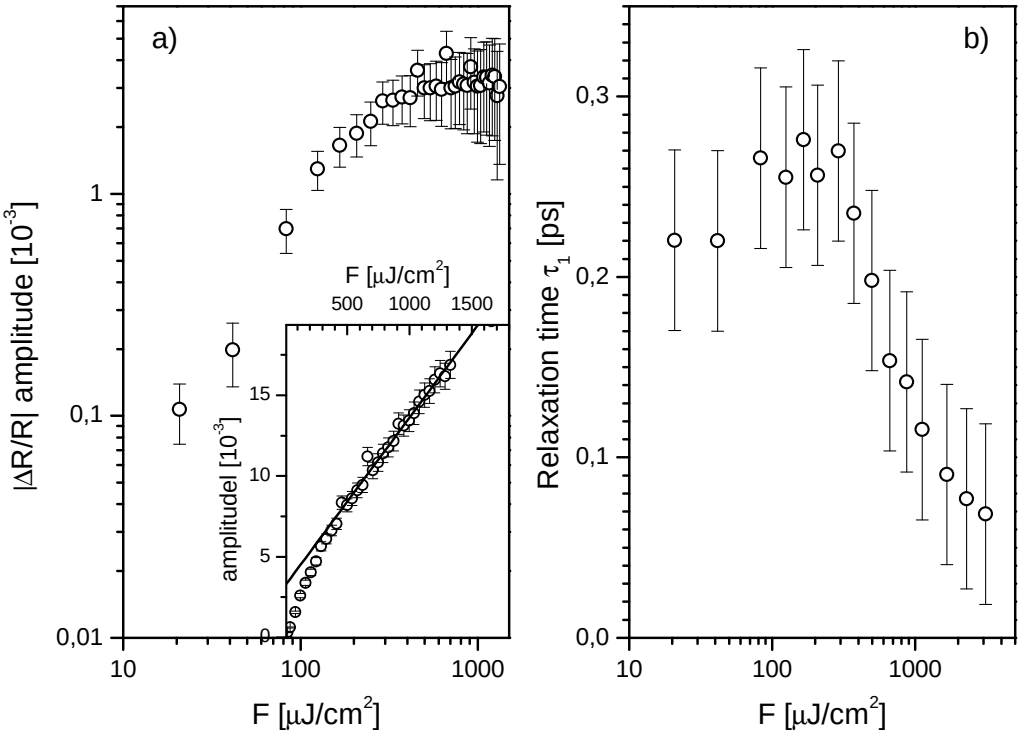

FIGURE 4.26: a) The excitation intensity dependence of the PI signal amplitude A_1 in a $K_{0.3}MoO_3$ film on Al_2O_3 substrate is shown in the inset. The linear part of the signal (solid line) is subtracted and the result is shown in the main graph. b) The intensity dependence of the relaxation time in a $K_{0.3}MoO_3$ film on Al_2O_3 substrate.

the inset of Figure 4.26a). This line can then be subtracted from the amplitude values to obtain an undistorted saturation curve shown in 4.26a. The absolute value of the amplitude in film is approximately one order of magnitude smaller than in crystal but the shape of the saturation curve in film is qualitatively very similar to the one obtained in the crystal (see Figure 4.10a).

Using pump and probe diameters $d_{pump} = (90 \pm 4)$ μm and $d_{probe} = (45 \pm 2)$ μm in Equation 3.26, we obtain $\frac{\Delta R(F=F_s)}{\Delta R_s} \approx 0.53 \pm 0.10$, which can be used on the data to estimate $F_s \approx (160 \pm 50)$ μJ/cm^2. This value is nearly identical to F_s in crystal (see Figure 4.10b).

The excitation fluence dependency of relaxation time τ_1, presented in Figure 4.26b, sheds some more light about the similarities of the CDW melting in film and crystal. The relaxation time τ_1 increases up to $F \approx 300$ μJ/cm^2, then starts diminishing strongly when $F \geq 200$ μJ/cm^2. A very similar behavior with the same characteristic fluence was observed in the crystal (see the inset of Figure 4.7), albeit with a larger divergence in τ_1 near the transition temperature.

4.4.4 Discussion

We have observed that the amplitude of the electronic signal as a function of the excitation intensity consists of two different signal components, where one is linear with excitation fluence and the other matches the saturation dependence of the electronic signal in $K_{0.3}MoO_3$ perfectly. This fact, together with the strongly diminished amplitude of the electronic signal in film indicates that only part of the film is in the CDW state.

This leads to the obvious assumption that the film consists of metallic and CDW state domains, which is also consistent with the measured phonon modes, which show diminished amplitude and stronger damping compared to their bulk counterparts.

We were not able to extract much more information about the CDW domains, however we have observed that the electronic dynamics is very similar in a film and crystal and even more importantly, the electronic condensation energies of a film and crystal match perfectly. This offers support that the CDW domains are large enough that no extraordinary finite size effects are observed. The upper limit of their size is determined by the grain size and is therefore approximately 1 μm.

4.5 Conclusions

From the measurements over a wide temperature and excitation fluence range in single crystals of $K(Rb)_{0.3}MoO_3$ it follows that the mechanism governing the recovery of the order parameter needs to be revisited. While the initial experiments suggested that in CDW system recovery dynamics follows similar processes as in superconductors, the complete absence of excitation intensity dependence in relaxation dynamics suggests that this is not the case. This fact, together with extremely short time scale of initial order parameter recovery, and the observation that the energy required to drive the semiconductor–metal phase transition in $K_{0.3}MoO_3$ is comparable to the electronic energy gain due to appearance of the CDW order [29] (see Section 4.3), suggests that on the sub picosecond timescale the electronic subsystem is decoupled from the lattice. Finally, the complete absence of F and applied electric field dependence of the second relaxation process (with τ_2) suggests that this process is not related to the dynamics of the phase mode. More likely, this second relaxation process is related to the second stage of the order parameter relaxation. The two different time-scales may stem from the experimental observation that the two subsystems (i.e. electrons and lattice) that interact to define the order parameter, are decoupled on very short time-scales. This would mean that on very short time-scales (shorter than the period of the AM) after

photoexcitation we can not describe the system with a single (equilibrium) complex order parameter, leading to relaxation dynamics on different time scales. The details of this process are so far unknown since we do not have a microscopic model to describe it.

From the measurements in the high perturbation regime, we conclude that in $K_{0.3}MoO_3$ the photoinduced CDW-M phase transition is non-thermal and takes place on the 100 fs timescale. The good agreement between measured E_{sat} and calculated E_{el}, the observation of the order parameter recovery on the sub-ps timescale, and the observation of zone-folded phonons high above E_{sat} suggest that during the process of melting and sub-ps recovery of the electronic modulation the lattice remains nearly frozen. This has an important implication for understanding the ultrafast relaxation processes in systems with reduced dimensionality, in particular for the systems with strong electron-phonon interactions that lead to phenomena like charge density modulation. The initial reconstruction of the CDW state is found in all systems studied thus far to proceed on the sub-ps timescale [10, 23, 24, 40, 41, 43]. Importantly, this timescale is one to two orders of magnitude faster than in the high-T_c superconductors [28], and is indeed close to the typical timescale for electron-phonon thermalization. The formation of the CDW requires freezing of a phonon and our results do imply that the lattice remains frozen in its modulated state on the sub-ps timescale after perturbation. Therefore, the extremely fast order parameter recovery in this entire class of low-dimensional materials [10, 23, 24, 40, 41, 43] could be a consequence of the fact that on the short timescale after photoexcitation the lattice remains in its unperturbed state. Thereby, the retaining $2k_F$ modulation presents a strong potential well driving ultrafast reformation of the charge density modulation. Clearly, further theoretical studies as well as studies of the ultrafast structural dynamics are required to shed additional light on these fascinating phenomena.

It is clear from the measurements on thin films that we have manufactured a series of thin films of $K_{0.3}MoO_3$. Femtosecond pump-probe spectroscopy has proven to be the most reliable characterization tool in determining the presence of the CDW formation in films. Judging by the dynamics, one could conclude that there is no drastic difference between the physics of $K_{0.3}MoO_3$ in bulk or in films. The main difference between the bulk and thin films was one order of magnitude smaller amplitude of the PI electronic signal together with smaller amplitude and stronger damping of all phonons. This can be attributed to two different phases of the material. The domain sizes are so far unknown so a future study, where the data on films would be compared to a series of systematically irradiated $K_{0.3}MoO_3$ crystals could shed more light on this problem. This is because irradiation introduces impurities in the crystal so domain size can be systematically decreased.

Chapter 5

Ultrafast Relaxation Phenomena in $(TaSe_4)_2I$

5.1 The structure of $(TaSe_4)_2I$

$(TaSe_4)_2I$ is a quasi one dimensional metal that belongs to the class of $(MX_4)_xY$ compounds (M = Ta, Nb; X = S, Se, Te; Y = I, Br, Cl; $x = 2, 3, \frac{10}{3}$) [132]. As is shown in Figure 5.1, the crystal structure consists of an arrangement of strongly bonded $(TaSe_4)_\infty$ chains parallel to the tetragonal c-axis which are separated by strands of iodine atoms. Ta atoms and Se_4 in each chain alternate. Se_4 follows a nearly regular screw arrangement along the c-axis with an angle of approximately 45° between consecutive rectangles. The crystallographic group at room temperature is $I422$ with lattice parameters $a = 9.531$ Å and $c = 12.824$ Å [132]. The body-centered unit cell contains two adjacent chains with four $(TaSe_4)$ units in each chain (see Figure 5.1).

Consecutive Ta atoms along a chain occupy two alternating and slightly non equivalent sites [132]. These two sites formally correspond to Ta^{4+} and Ta^{5+} valence states with one conduction electron per formula unit, assuming an I^- state for the iodine atoms. This is confirmed by the Hall effect [134] and thermopower measurements [135]. Band-structure calculations [136] also confirm this picture while also suggesting a single quarter filled d_{z^2} electronic band at the Fermi level. The strong structural anisotropy is also followed by strong anisotropy in conductivity between the directions parallel and perpendicular to the chains ($\sigma_{||}/\sigma_\perp \approx 500$) [137].

The diffraction and resistivity data show that the Peierls transition temperature is $T_c^{3D} \approx$ 260 K [138, 139]. The non-linear electrical response below T_c^{3D} is characteristic for a CDW ground state [138, 139]. The formation of an incommensurate modulation

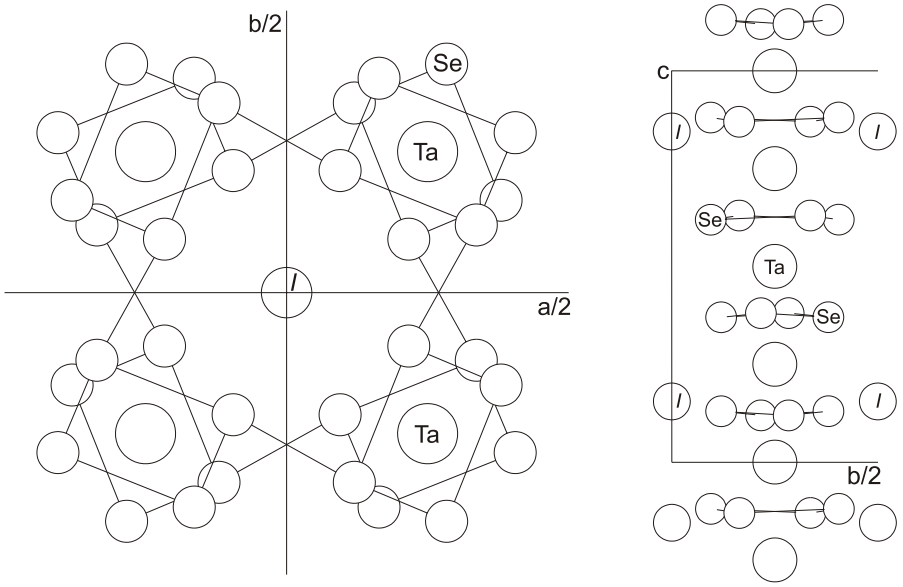

FIGURE 5.1: Projection of the basic structure of one unit cell onto the $(\vec{a}, \vec{b})$ plane is shown on the left whereas the side view of one chain is shown on the right [133].

below T_c^{3D} is revealed by the X-ray [68] and electron diffraction experiments [140]. The modulation wavevector of the modulation is $\vec{q_s} = (\pm\eta, \pm\eta, \pm\delta)$ where $\eta = 0.045$ and $\delta = 0.085$ [141].

Such a small value of the modulation wavevector can be understood in terms of band-structure arguments. The band structure of $(TaSe_4)_2I$ is interpreted by folding the d_{z^2} band into one fourth of the original Brillouin zone. On the other hand, the quarter-filled d_{z^2} leads to a Fermi wavevector $k_F = \frac{1}{4}\frac{\pi}{d} = 0.5c^*$, where d is the Ta-Ta distance along the chain. In other words, due to tetramerization k_F is located on the edge of the new Brillouin zone, whereas the CDW modulation wavevector $q_s = 2k_F$ is folded to $k = 0$. The finite size of q_s stems from the fact that $(TaSe_4)_2I$ contains two chains in the unit cell. The interaction between the two chains makes the d_{z^2} band split into a doublet, and the folding effect of the Brillouin zone deviates the k_F from $0.5c^*$ to $0.458c^*$ [142], also causing q_s to fold to a finite value near $k = 0$.

5.2 Motivation

As we have already mentioned in Section 2.6, the ratio between the low temperature electronic gap and the Peierls transition temperature is often found to be too large, $\frac{2\Delta}{k_B T_c^{3D}} \gg 3.5$ (see Equation 2.16). This motivated Aubry et al. [86, 86] to explain the CDW physics with an alternative strong-coupling description. In this picture, the

CDW is described as a dense bipolaronic fluid, while the gap energy $2\Delta \approx 3000$ K corresponds to the binding energy of a single bipolaron. The transition occurs once the repulsive residual interaction energy between bipolarons E_{rep} is overcome by the gain in the electronic energy due to charge density modulation, so E_{rep} can be estimated to be of the order of magnitude of T_c^{3D}. Since the bipolaron binding energy is usually far greater than the repulsive residual interaction energy between bipolarons, one expects to find $T_c^{3D} \ll 2\Delta/k_B$

Therefore, the validity of the weak coupling model rests heavily on the assumption that the ratio between intrachain and interchain interaction energies is large. The relevant interactions here are both electronic and elastic because the CDW formation is caused by their interplay. This is why one needs to be careful when determining the system anisotropy from the measurements of electrical resistivity because it reflects only the electron mean path.

The direct information about the correlation lengths and the q-dependent order parameter can be resolved from diffuse x-ray scattering data with measurements being performed on some compounds such as $NbSe_3$ and $K_{0.3}MoO_3$ [143]. The gap measurements on $K_{0.3}MoO_3$, analyzed in the weak-coupling framework, suggest the ratio T_c^{MF}/T_c^{3D} to be 2–3 [54, 120]. However, the ratio of the in-chain ($\xi_{||}$) and the largest transverse ($\xi_{\perp}$) correlation lengths is only a factor of 4, as obtained from the x-ray measurements [144, 145]. It is important to note that the largest transverse correlation length is always larger than the relevant interchain distance. Therefore, despite being widely recognized as one of the prototype one-dimensional CDW materials, the validity of the weak coupling theory is experimentally not firmly established in the case of $K_{0.3}MoO_3$.

$(TaSe_4)_2I$, on the other hand, presents a system, where the weak coupling theory is even less likely to be applicable. The material undergoes a Peierls transition near 260 K with gap energy of $2\Delta \approx 3000$ K $= 11.5 k_B T_c^{3D}$, as obtained from the resistivity [138, 139] and optical data [146]. The X-ray measurements [68] also indicate, that the correlation length ratio is very small, $\xi_{||}/\xi_{\perp} \approx 1$–2.

These experimental findings pointing towards the conclusion that $(TaSe_4)_2I$ is a strong-coupling system motivated us to examine the material using femtosecond spectroscopy in order to determine if there was any major qualitative difference in the electronic dynamics between the strong and weak coupling regimes.

5.3 Experimental Results

The preliminary experiments on $(TaSe_4)_2I$ were performed at the Jožef Stefan Institute, with a detailed and systematic study of the intensity and temperature dependence of the photoinduced transient signal performed at the University of Konstanz. Therefore, unless specifically stated otherwise, the results presented in this section will be presumed to have been measured at the Konstanz University using the fast scanning technique that is described in detail in Section 3.1.3. We used 40 fs laser pulses at 1.55 eV (λ = 800 nm) from a regenerative amplifier with a repetition rate of 250 kHz as a source of both photoexcitation (*pump*) and *probe* pulse trains (see Section 3.1.3). The experiments were performed on a single crystal of $(TaSe_4)_2I$. The direction of the *probe* beam was chosen to be parallel to the chain direction ([001]) while the polarization of the *pump* beam was perpendicular to the *probe*. The polarization alignment was performed by taking advantage of the experimental observation that the reflectivity changes by more than three-fold when the light polarization is rotated by $\pi/2$, as is shown in the inset of Figure 5.2a. This is also in accordance with the data found in the literature [147]. The absolute minimum in reflectivity R with respect to the beam polarization corresponded well to the chain direction. The *pump* and *probe* beams were focused onto the sample with diameters of $d_{pump} = (90 \pm 4)$ μm and $d_{probe} = (45 \pm 2)$ μm. The average power of the *pump* beam was varied between 50 μW and 20 mW, which corresponds to fluences of 2 $\mu J/cm^2$ – 800 $\mu J/cm^2$ on the probed spot. The samples were mounted in an optical cryostat and the temperature was varied between 4 and 300 K using liquid helium as a cooling agent. The temperatures were measured at the cold finger of the cryostat.

It should also be noted here that even though the sample surface was relatively large (approximately 0.2 cm^2) and seemingly mostly flat, it was relatively difficult to find a spot with a diameter $d = 100$ μm, where the reflected beam would be of high quality. On the majority of the sample the reflected beam was line-shaped due to the diffraction on the surface. The diffraction of light was caused by the diffraction grating-like structure of single strands of $(TaSe_4)_2I$ on the surface of the sample. This structure occurs almost always when the sample is cleaved - due to the one dimensionality of the crystal structure, the sample cleaves in single strands, leaving a grating-like structure on the surface. After cleaving the sample several times, we were able to find an elongated (pointing in the chain direction) flat surface on the sample with good optical quality which enabled us to conduct the experiments.

5.3.1 Low Perturbation Regime

The temperature dependence of the signal obtained in the low-perturbation regime is presented in Figures 5.2 and 5.3. In Figure 5.2 we show the photoinduced transient signal measured at several arbitrarily selected temperatures below and above the transition temperature $T_c^{3D} = 260$ K. The incoherent part of the signal consists of a sum of a step-like signal, a fast decaying component with a 200 fs dynamics and a slower decaying component with a 1 ps dynamics. The amplitude of the faster incoherent signal ($\tau_1 \approx 200$) is negative and seems to increase with temperature (see 5.3). The amplitude of the slower incoherent signal ($\tau_2 \approx 1$ ps) is positive and decreases with increasing temperature. To obtain a more quantitative result, we used a similar approach as in the previous chapter to fit the data. We found that the data above the transition temperature can be well modeled by a single exponential decay. The non-oscillatory data below the transition temperature fit well to a sum of two exponential functions and a step function (see Figure 5.4a). The fit residual contains the oscillatory part of the data (see Figure 5.4b) which can then be analyzed separately by means of FFT or fitting.

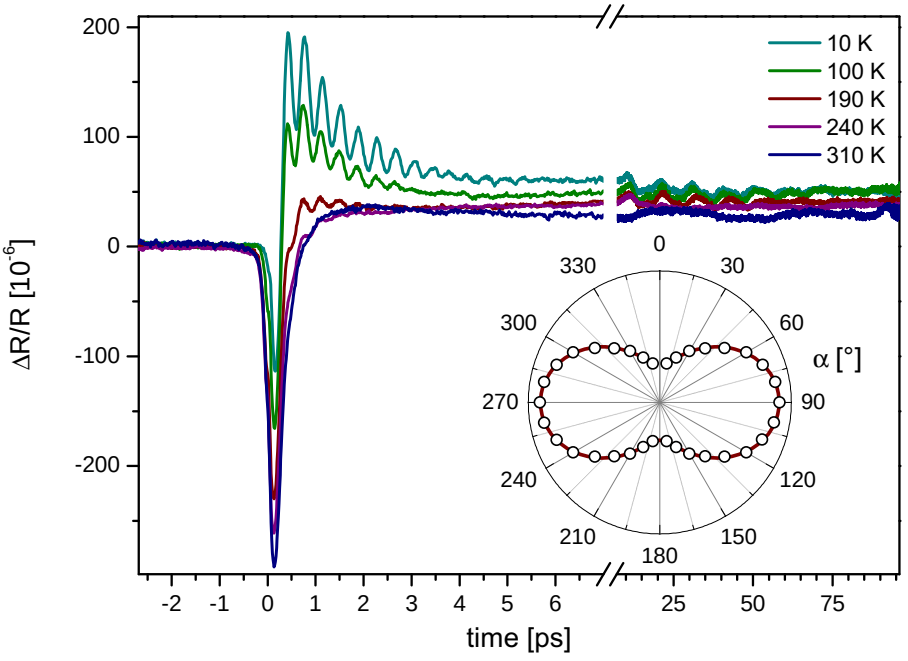

FIGURE 5.2: PI reflectivity changes in $(TaSe_4)_2I$ following photoexcitation with a 40 fs optical pulse at different temperatures. The measurements were performed with the *probe* polarization along the chains. The inset shows the polarization dependence of normalized reflectivity where the angle $\alpha = 0$ corresponds to the chains direction. The open circles are the measured data and the line is the sine fit that fits almost perfectly.

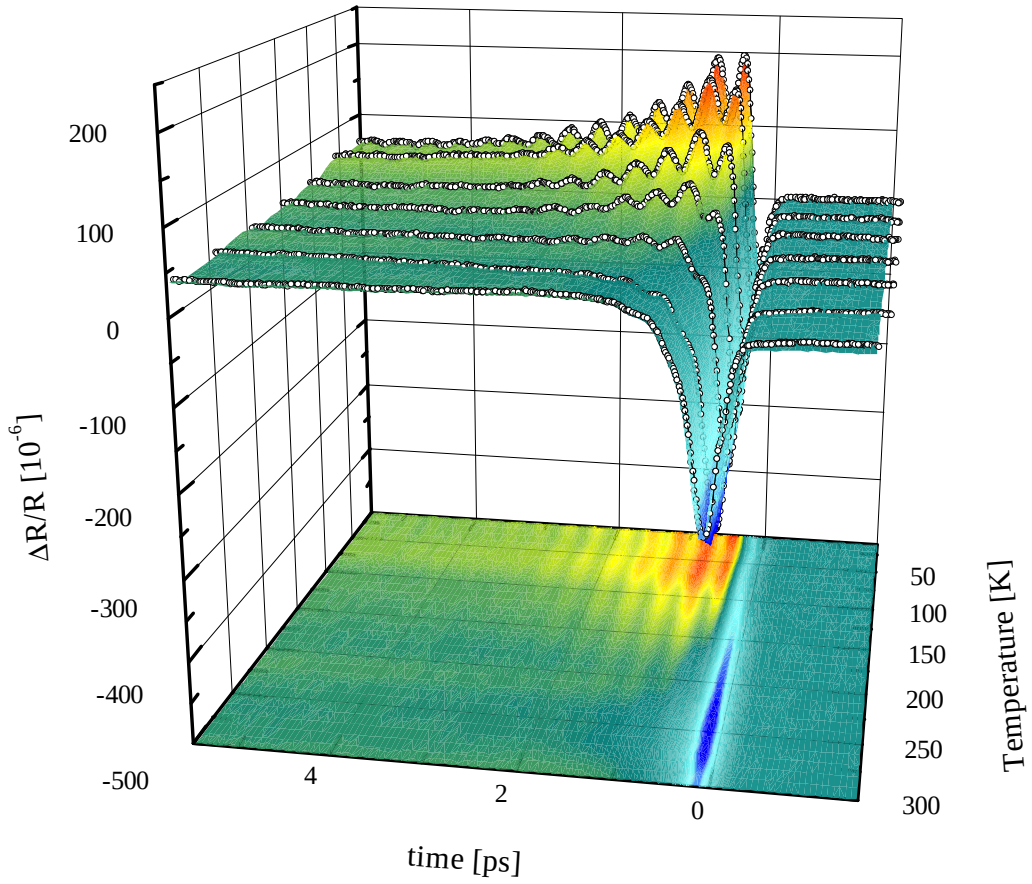

FIGURE 5.3: We plot the temperature dependence of the PI reflectivity changes in $(TaSe_4)_2I$ as a 3D surface. For presentation purposes, we also plot several transient signals on the same graph (open circles).

The following fitting function was used in the analysis of the non-periodic component of the transient signal:

$$\begin{aligned} S(t) &= \left[A_1(t)e^{-t/\tau_1} + A_2(t)e^{-t/\tau_2} + A_3\right] H(t), \\ H(t) &= \begin{cases} 1, & \text{if } t > 0 \\ 0, & \text{if } t \leq 0 \end{cases} . \end{aligned} \tag{5.1}$$

We plot the absolute values of the amplitudes A_1, A_2 and A_3 obtained from the fit in Figure 5.5a together with the temperature dependence of the electronic gap. The amplitude $|A_1|$ ($\tau_1 \approx 200$ fs) increases with temperature and has a local maximum near the transition temperature. The temperature behavior of the amplitude A_2 ($\tau_2 \approx 1$ ps) is particularly interesting since it follows the temperature dependence of the superlattice reflections intensities in $(TaSe_4)_2I$ (solid triangles). The amplitude A_3 does not display

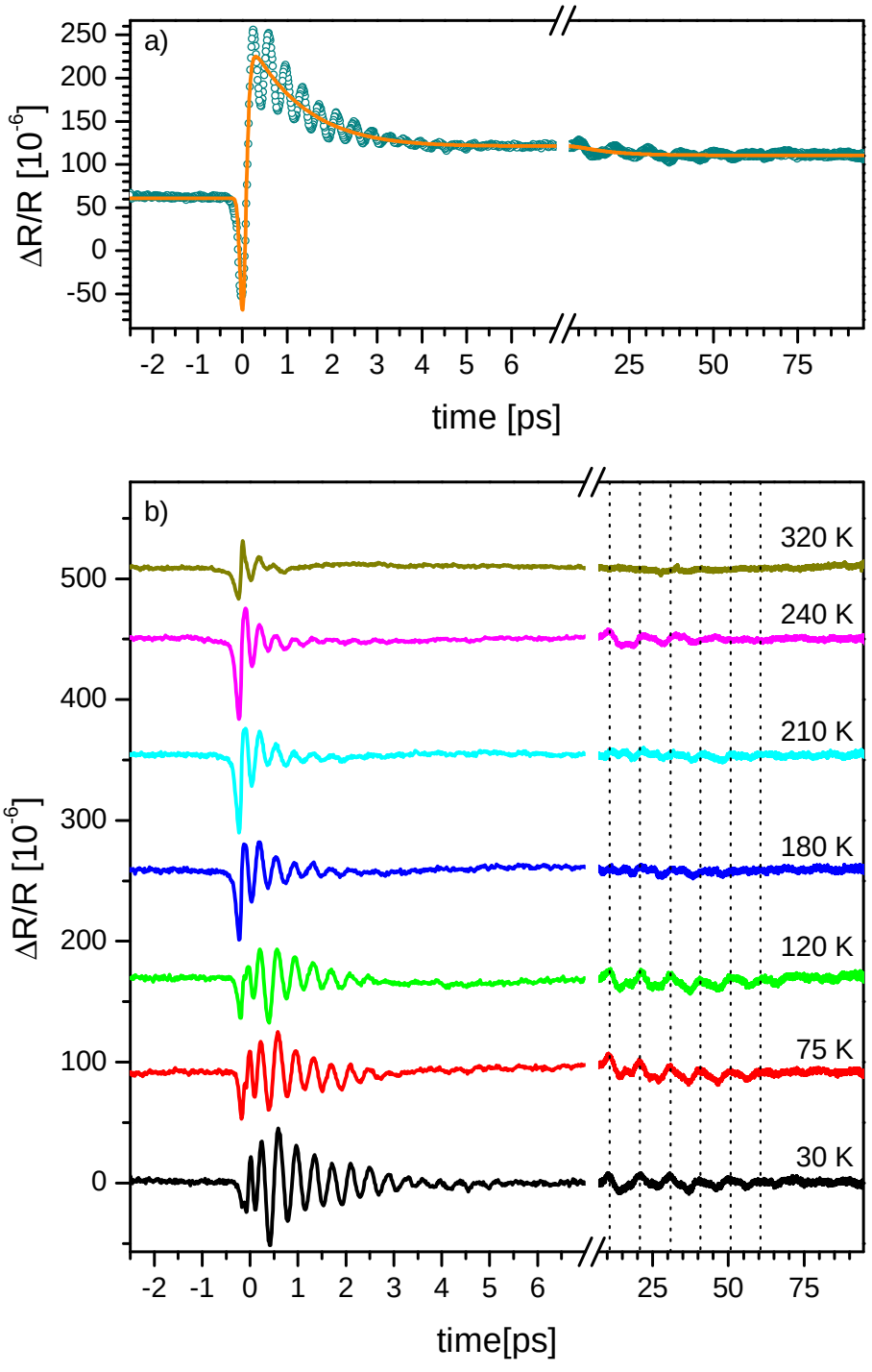

FIGURE 5.4: a) A typical fit (line) of a PI reflectivity transient (open circles). b) The fit residual showing oscillations in the high and low frequency range. The vertical lines denote an oscillation period at low temperature. The data have been offset for clarity.

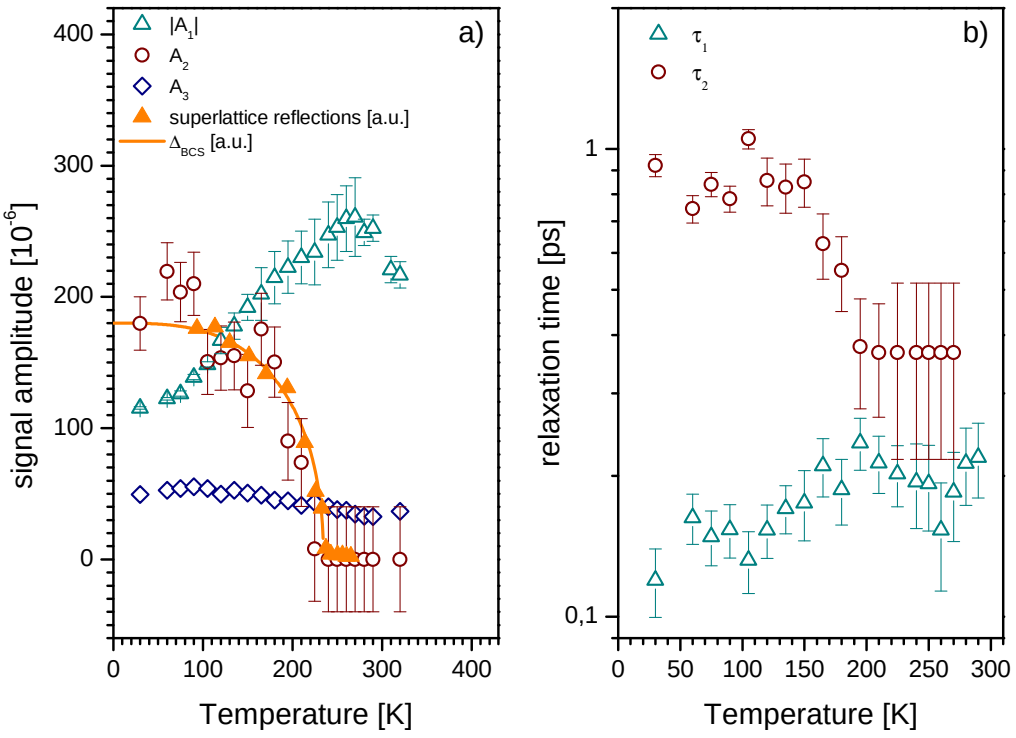

FIGURE 5.5: a) The temperature dependence of the amplitudes of the three incoherent signal components (open symbols). The normalized superlattice reflection intensities obtained from Ref. [68] are also plotted for comparison (solid triangles) and display the same temperature dependence as A_2. The solid line is the temperature dependence of thy BCS gap obtained from the superlattice reflections. b) The temperature dependence of the relaxation times of the two exponentially decaying signal components.

any pronounced temperature dependence as it decreases almost linearly from low to high temperatures. Due to the very slow dynamics of the latter signal we ascribe it to single pulse heating. Additional experimental confirmation for this assignment comes from the intensity dependent measurements which are described in Section 5.3.2.

We plot the temperature dependence of the two relaxation times obtained by fitting the data using Equation 5.1 in Figure 5.5b. The dynamics of the faster process slows down with increasing temperature as the relaxation time increases from $\tau_1(T = 30\,\mathrm{K}) = 120\,\mathrm{fs}$ to $\tau_1(T = 300\,\mathrm{K}) = 250\,\mathrm{fs}$. On the other hand, the relaxation time of the slower process decreases with temperature, as it changes its value from $\tau_2(T = 30\mathrm{K}) = 1\mathrm{ps}$ to $\tau_2(T = 300\,\mathrm{K}) = 350\,\mathrm{fs}$. The temperature dependence of both relaxation times is quantitatively very similar to the temperature dependence of the two relaxation times in $K_{0.3}MoO_3$ (see Figure 4.3) although it should be noted that the two relaxation times in $K_{0.3}MoO_3$ differ by almost two orders of magnitude at low temperatures and by only a factor of 5 in $(TaSe_4)_2I$.

The relatively large error bars in Figures 5.5a and 5.5b stem from the fact that fitting a bipolar bi-exponential decay with similar relaxation times can be quite difficult due to

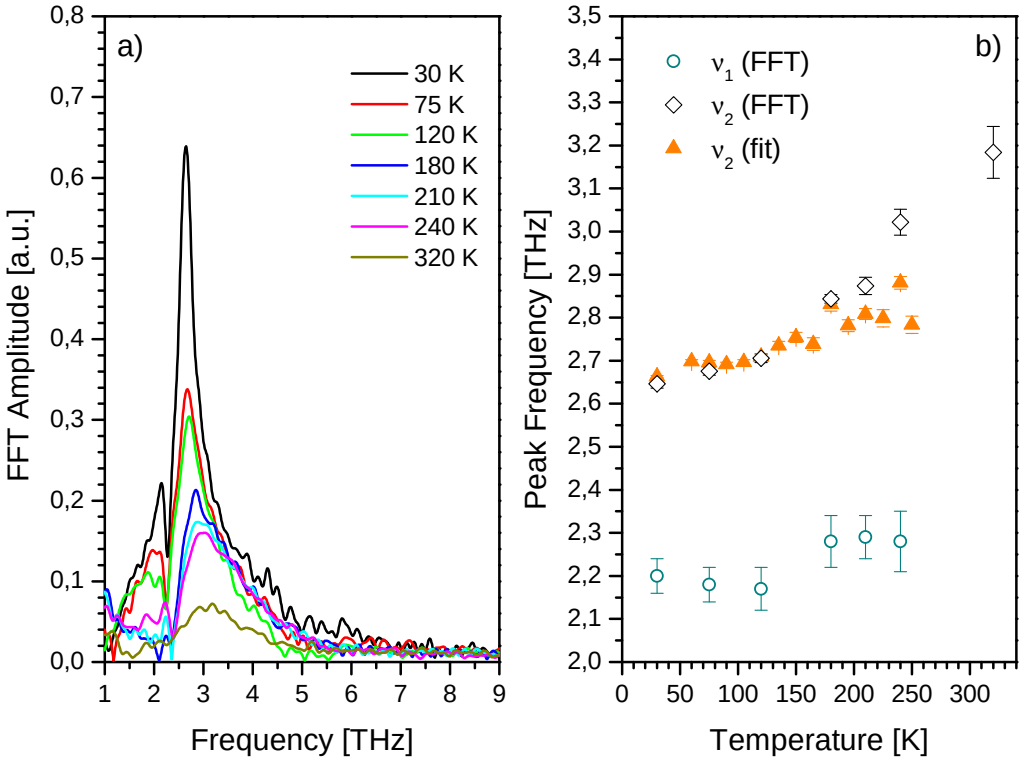

FIGURE 5.6: a) The temperature dependence of the high frequency part of the FFT spectrum. b) The temperature dependencies of both peak frequencies obtained by FFT analysis (open symbols) and fitting (full symbols).

the co-dependency of the fitting parameters. In fact, the parameter τ_2 had to be fixed to a constant value above 170 K to achieve convergence of the fitting parameters.

After fitting out the incoherent part of the signal (see Figure 5.4), we performed FFT analysis of the residual oscillatory data (see Figure 5.4b). We present the results of the analysis in Figure 5.6. In Figure 5.6a we present the high frequency part of the FFT spectrum containing what looks like two asymmetric peaks at 2.2 THz and 2.6 THz with different amplitudes. This kind of shape of the FFT spectrum is obtained for two damped oscillators with close frequencies. However, for two modes with close frequencies, the maxima in the FFT spectrum do not correspond to their respective central frequencies (see Figure 5.7). In our case the amplitude of the 2.6 Thz mode is about one order of magnitude larger than the amplitude of the 2.2 THz mode so one expects that the maximum of that peak in the FFT spectrum corresponds well to the actual frequency of the mode. We confirmed this by fitting the oscillatory data with a function of the form $S(t) = \cos(2\pi\nu t - \phi)e^{-t/\tau}$. We found that the temperature dependence of the frequency of the 2.6 THz mode obtained from the fit and FFT matches well (see Figure 5.6a).

In order to get some more insight about the temperature dependency of the 2.2 THz mode, we simulated several signals $f(t)$ of two damped oscillators of the form $f(t) =$

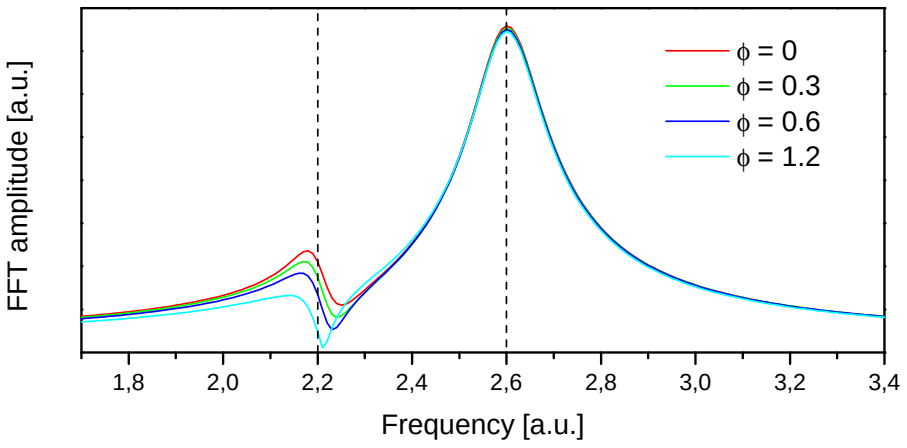

FIGURE 5.7: The FFT spectra of simulated data of two modes with frequencies $\omega_1 = 2.2$ and $\omega_2 = 2.6$ as a function of the relative phase ϕ. The vertical dashed lines mark the two central frequencies of the modes.

$B_1 \cos(2\pi\omega_1 t - \phi)e^{-t/\tau_1} + B_2 \cos(2\pi\omega_2 * t)e^{-t/\tau_2}$. Here the amplitudes are chosen[1] to be $B_1 = 10$, $B_2 = 1$, frequencies are $\omega_1 = 2.2$, $\omega_2 = 2.6$ and damping constants are $\tau_1 = 4$, $\tau_2 = 2$, whereas the relative phase ϕ is a free parameter. FFT analysis was performed on the simulated data and is presented in Figure 5.7. We found that the maximum of the stronger mode remains roughly constant due to its high amplitude, while the peak of the weaker mode shifts to lower frequencies for all phases. Moreover, ω_1 lies on the edge of the steep high frequency tail of the 2.2 mode for all relative phases. This analysis helped us obtain the temperature dependency of the frequency of the 2.2 THz mode that we plot in Figure 5.6a. There the frequency of the 2.2 THz mode is defined as the central frequency of the high frequency tail of the 2.2 THz peak in the FFT spectrum.

Both peaks presented in Figure 5.6a show expected temperature behavior, which means decreasing amplitude and increasing widths with increasing temperature. The frequency dependence of these two peaks is shown in Figure 5.6b. The frequency of the weaker peak remains roughly constant between 30 K – 120 K and it increases within error bars above 180 K. The frequency of the stronger peak increases by almost 15% from 30 K to 260 K. We were tempted to assign the 2.6 THz mode as the amplitude mode (AM) due to its high amplitude which also follows similar temperature dependence as the amplitude of the AM in $K_{0.3}MoO_3$. However, we found this assigment unlikely since the AM should soften with increasing temperature (see Equation 2.12).

The obtained temperature dependence of the high frequency part of the FFT spectrum is in accordance with different Raman scattering measurements in the literature [148, 149], however the authors could not offer a suitable explanation for the hardening of the 2.6 THz (90 cm^{-1}) mode [148] and even suggested that it was just a fitting artifact [149]. On

[1]The goal was to choose parameters that correspond well to the experimentally obtained spectra.

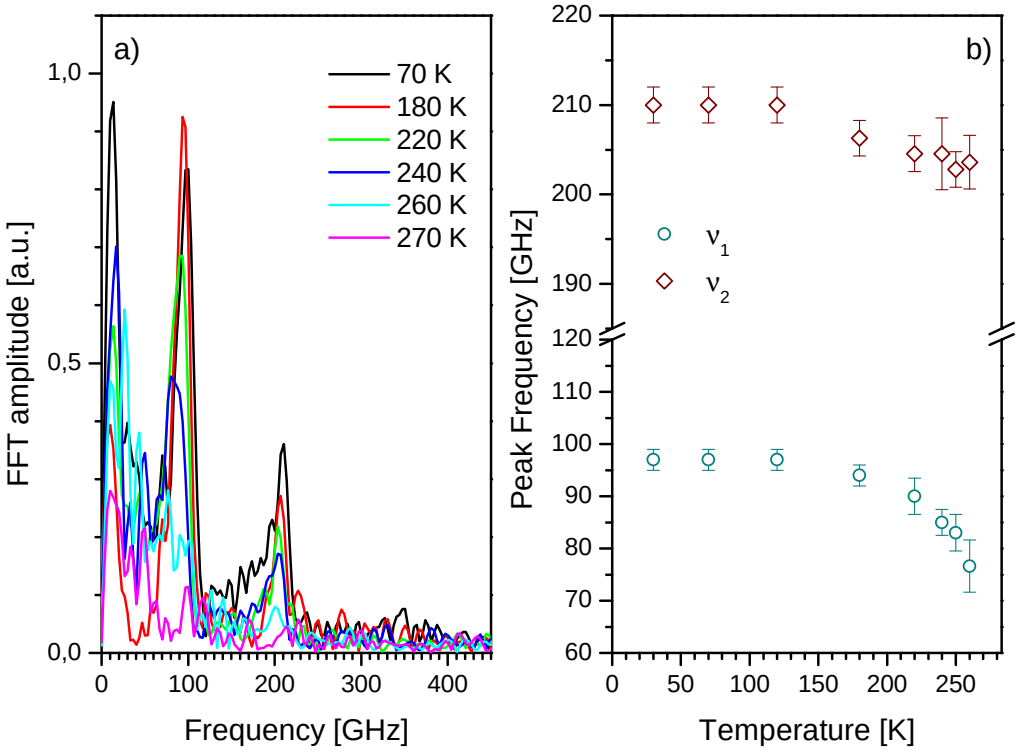

FIGURE 5.8: a) The temperature dependence of the low frequency part of the FFT spectrum. b) The temperature dependencies of the two peak frequencies obtained by FFT analysis.

the other hand, the observation of the hardening of the 2.6 THz mode is not consistent with the Raman scattering measurements by Sugai et al. [142], who assigned the 2.6 THz mode as the AM. According to their measurements, the frequency of the 2.6 peak should be constant below the transition temperature. They proposed a CDW transition model where the anomalous temperature dependence of the AM frequency was explained by strong interaction between the Kohn anomaly transversal optical (TO) mode and the transversal acoustic (TA) mode, both of which are on the same branch of the extended Brillouin zone of the $TaSe_4$ unit. As a consequence of the interaction, the TA mode condenses prior to the Kohn-anomaly TO mode. We find it important to note that while this model could account for a constant frequency of the 2.6 THz mode within the experimental uncertainty [142], the model can not explain our observations that the frequency of the 2.6 THz mode increases with temperature.

In Figure 5.8a we display the three low frequency modes at frequencies $\nu_1 \approx 100$ GHz and $\nu_2 \approx 200$ GHz and $\nu_3 \approx 10$ GHz. The entire time window in our measurements was 100 ps (see Figure 5.2) determining the resolution of the FFT as $\Delta\nu \approx 10$ GHz, therefore the part of the FFT spectrum where $\nu \leq 10$ GHz, including the mode at $\nu \approx 10$ GHz is beyond our resolution and is consequently not reliable. As a result, only the two modes with higher frequencies will be discussed. The temperature dependence of

the amplitude and width (damping) of the low frequency and high frequency modes is similar, meaning that the amplitude decreases with increasing temperature whereas the damping increases. The frequencies of the two low frequency modes obtained from the FFT spectrum are plotted in Figure 5.8. The frequency of the 200 GHz peak slightly decreases with increasing temperature but this softening is within the error bars of the measurement. On the other hand, the softening of the 100 GHz peak reaches ≈20%, well beyond the error bars. Our results are consistent with the neutron scattering measurements [37] of the TA phonon frequency and damping at the CDW satellite position. This kind of temperature dependency of frequency is similar to the temperature dependence of frequency of the AM mode in $K_{0.3}MoO_3$, however the neutron scattering measurements [37] reveal no indication of a change in line-shape associated with a splitting of the TA response into phason and AM, which the authors attribute to the strong-coupling CDW physics (see Section 2.6). The phonon splitting into the phason and AM is a weak-coupling CDW fingerprint predicted by numerical simulations [75] and measured by means of neutron scattering [76] in $K_{0.3}MoO_3$. On the other hand, the neutron scattering measurements in $(TaSe_4)_2I$ are not entirely conclusive since a limited amount of phason-amplitudon decoupling could be present but may go undetected due to the finite frequency and wavevector resolution [37].

We plot the temperature dependence of the area under the peaks in the FFT spectrum[2] in Figure 5.9. The amplitudes of the high frequency modes (Figure 5.9a) decrease with temperature, however we do not observe any pronounced temperature behavior near the transition temperature. Furthermore, the temperature dependence of the amplitude of the 2.6 THz mode seems to be approximately linear. On the other hand , the temperature behavior of the amplitudes of the two low frequency modes seems to be more pronounced (Figure 5.9b), especially the temperature dependence of the amplitude of the 100 GHz mode, which is approximately constant from 30 K – 180 K and abruptly decreases above that temperature.

5.3.2 High Perturbation Regime

In the second stage of our experiments, we studied the intensity dependence of the PI reflectivity dynamics in $(TaSe_4)_2I$ at different temperatures. In Figure 5.10 several PI transients normalized to the excitation fluence are plotted as a function of the *pump* fluence. At fluences 20 $\mu J/cm^2$ – 200 $\mu J/cm^2$ (solid lines in Figure 5.10), there is little change in the dynamics however the amplitudes of different signal components begin to change. In that fluence range, the amplitudes of both exponentially decaying

[2]The amplitude A of a damped oscillatory signal $A\sin(\omega t)\exp(-t/\tau)$ is proportional to the area under the peak in the corresponding FFT spectrum.

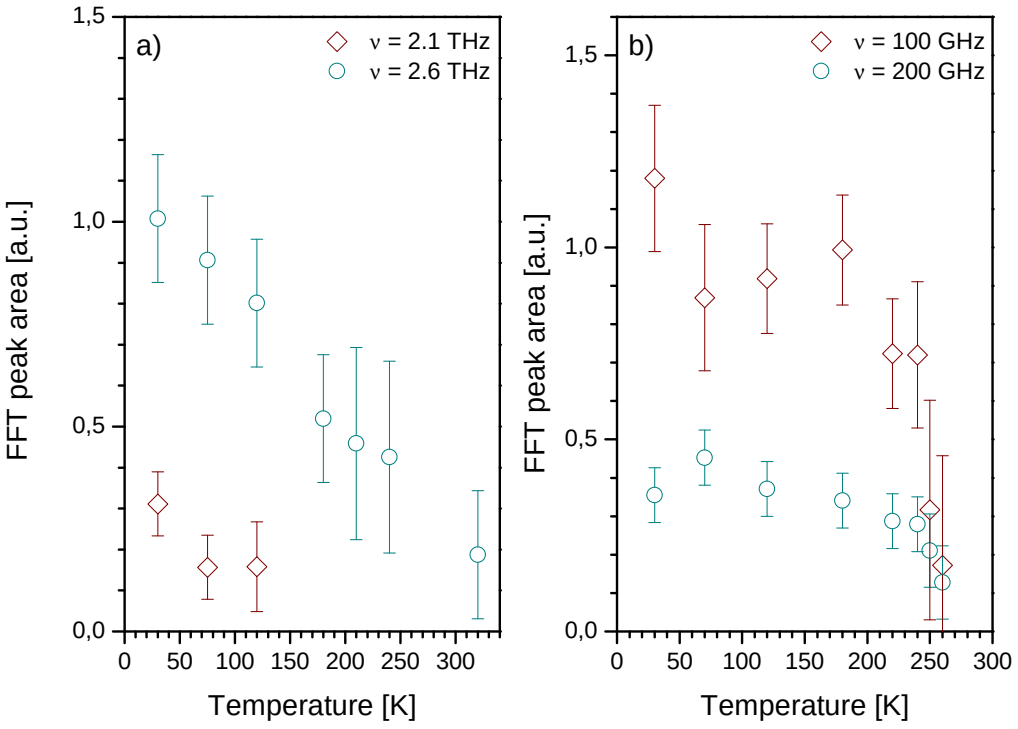

FIGURE 5.9: The temperature dependence of the area under the peaks in the FFT spectrum. In a) we display the areas of the two high frequency peaks whereas in b) we display the areas of two low frequency peaks.

components are linearly proportional to the excitation fluence whereas the amplitude of the oscillations show sublinear intensity dependence above 40 μJ/cm^2. At fluences above 200 μJ/cm^2 (dotted lines in Figure 5.10) there is an obvious qualitative change in the dynamics of the signal which also coincides with the onset of sublinear dependency of the amplitude of the 200 fs exponential decay component with excitation intensity.

The data was further analyzed using the same fitting procedure that was used earlier in this section (see Equation 5.1). The amplitudes of the two exponentially decaying signals A_1 and A_2 are shown in Figure 5.11a as a function of excitation fluence. Both amplitudes display similar saturation behavior above $F \approx 200$ μJ/cm^2 as was observed in the intensity dependence of the amplitudes of the 200 fs and 5 ps signals in $K_{0.3}MoO_3$ (see Figure 4.10) that was attributed to the melting of the CDW. It is reasonable to assume that the saturation has the same origin in $(TaSe_4)_2I$. Under that assumption, we fitted the intensity dependence of the signal amplitude at different temperatures using the model presented in Section 3.2.1. Due to the high anisotropy of the sample the estimated penetration depths of the two beams were $\delta_{probe} = (137 \pm 27)$ nm and $\delta_{pump} = (55 \pm 11)$ nm. Using these parameters together with the measured beam-widths ($2\rho_{pump} = (90 \pm 4)$ μm and $\rho_{probe} = (45 \pm 2)$ μm), we estimate the reflectivity change

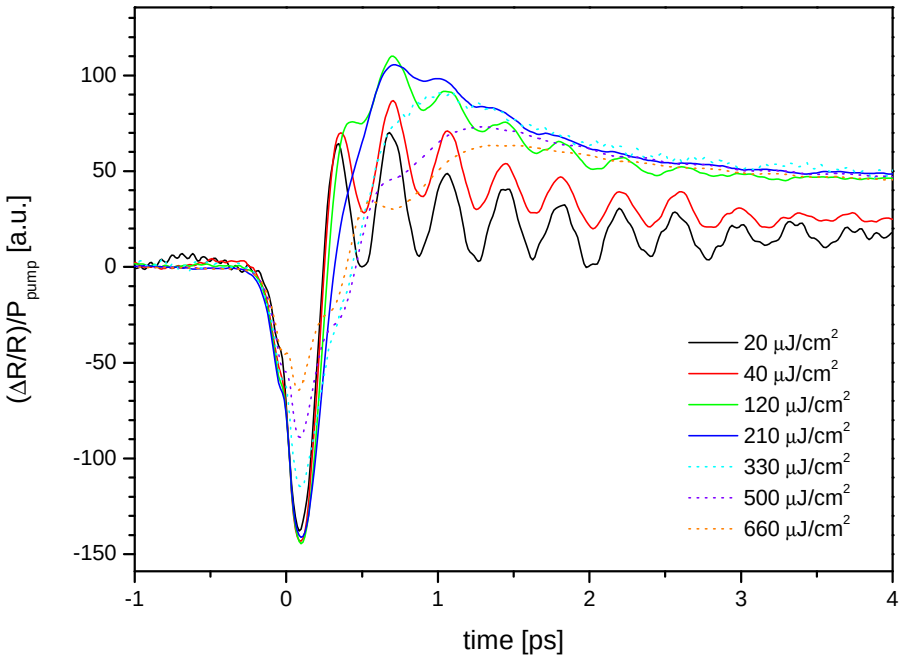

FIGURE 5.10: PI reflectivity changes in $(TaSe_4)_2I$ normalized to the excitation fluence at different *pump* fluences. The dynamics of transients where $F \leq 200$ μJ/cm^2 (solid lines) appears to be qualitatively different from the dynamics of the transients where $F > 200$ μJ/cm^2 (dotted lines).

using Equation 3.29, $\frac{\Delta R}{\Delta R_s}(F = F_s) \approx 0.35 \cdot (1 \pm 0.6)$. We plot the obtained values of the saturation fluence F_s in Figure 5.12 as a function of temperature.

The determined low temperature value for the the saturation fluence is therefore $F_s = (90 \pm 50)$ μJ/cm^2. To evaluate this number, we compared it to the energy gain by the electronic subsystem upon CDW condensation, given by Equation 4.2. Using $\Delta = (120 \pm 6)$ meV [138, 139], $\epsilon_F = 0.059$ eV – 0.68 eV [60, 137, 150] and $n(\epsilon_F) = 1.3$ eV^{-1} – 14.4 eV^{-1} [150], we obtain $E_{el}(4K) = (160 \pm 70)$ meV/u.c.v.. On the other hand, the saturation energy obtained from F_s is $E_s = (70 \pm 40)$ meV/u.c.v, which is well within the errorbar of E_{el}.

We plot the intensity dependence of the amplitude of the step-like signal in the inset of Figure 5.11a. Due to the very slow dynamics of this signal component[3] and due to the linear intensity dependence of its amplitude over the entire fluence range, we conclude that this is signal is caused by the transient heating of the sample (also see Section 3.1.4.2).

The relaxation times τ_1 and τ_2 of the two exponentially decaying signal components are plotted in Figure 5.11b as a function of excitation intensity. There seems to be

[3]Relaxation time was much longer than 100 ps, which is the time window of our measurement.

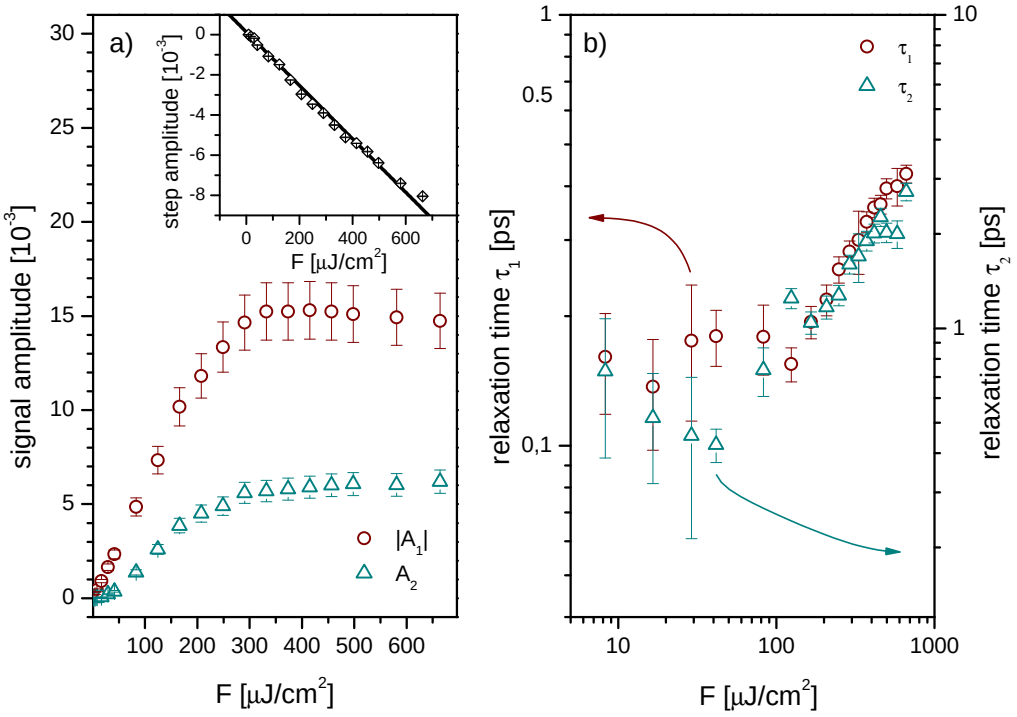

FIGURE 5.11: a) The amplitudes of the two exponentially decaying signal components as a function of *pump* fluence. The inset shows linear intensity dependence of the amplitude of the step-like signal. b) The relaxation times of the two exponentially decaying signal components as a function of excitation intensity. The inset shows the temperature dependence of the saturation fluence F_s. The dashed line is obtained from Equation 4.2.

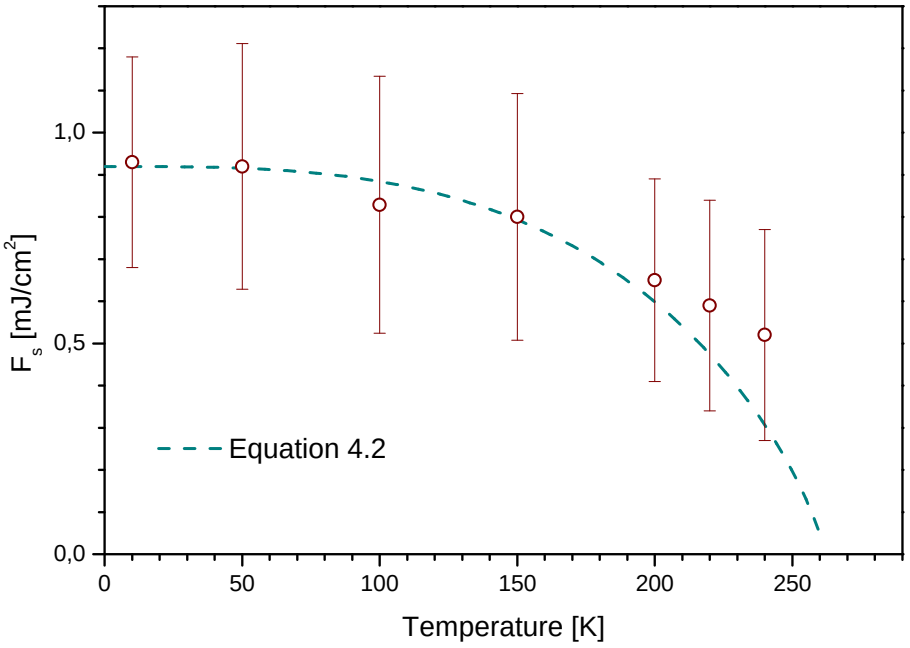

FIGURE 5.12: The temperature dependence of the saturation fluence F_s (open circles). The temperature dependence of the electronic energy gain due to CDW formation given by Equation 4.2 is plotted as a dashed line.

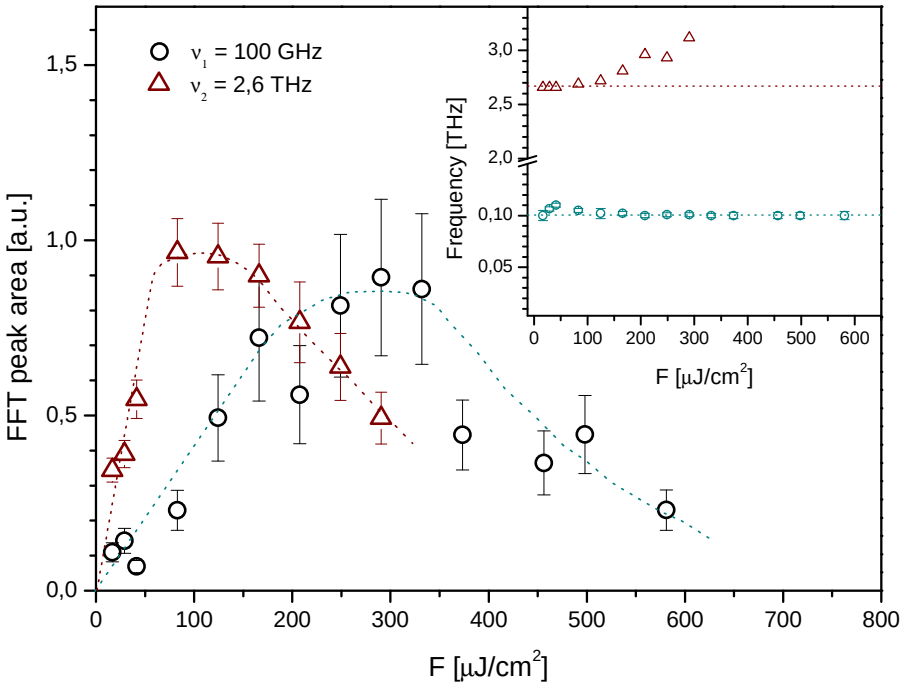

FIGURE 5.13: The intensity dependence of the amplitudes of the 100 GHz (open circles) and 2.6 THz modes (open triangles). The intensity dependence of frequencies of these two modes is shown in the inset. The dotted lines are guides to the eye.

no dynamics change within error bars when $F \leq 200$ μJ/cm^2. At higher fluences the dynamics of both processes slow down with increasing excitation intensity.

We performed FFT analysis of the oscillatory response as a function of excitation fluence. In Figure 5.13 we plot areas of the 100 GHz and 2.6 THz peaks[4]. The area of the 100 GHz peak increases linearly with excitation fluence when *pump* fluence is less than $F_1 \approx 200$ μJ/cm^2, where it reaches a plateau, and starts decreasing when $F_2 \approx 350$ μJ/cm^2. The onset of the plateau at $F \approx 200$ μJ/cm^2 corresponds well to the excitation fluence where there is observable change in the shape of the transients (see Figure 5.10). The fact that this signal is still observed at F as high as 600 μJ/cm^2 is not unusual due to the vastly different optical penetration depths of *pump* and *probe* beams. It is also experimental proof that heating was not an issue because the amplitude of the 100 GHz oscillation has been shown to drop to zero above T_c^{3D} (see Figure 5.9), which was clearly not achieved even at $F = 600$ μJ/cm^2. The intensity dependence of the area of the 2.6 THz peak is qualitatively the same as that of the 100 GHz mode, however that signal component reaches the plateau at $F < 100$ μJ/cm^2.

In the inset of Figure 5.13 we display the intensity dependence of the frequencies of 100 GHz and 2.6 THz modes. We observe a small increase $\Delta\nu_1 \approx 10$ GHz in the frequency of

[4]The low - and high-frequency FFT spectra were obtained separately with different normalizations so the ratio of the two mode amplitudes does not correspond to the absolute value.

the 100 GHz mode between 20 μJ/cm^2 and 100 μJ/cm^2. However, since the frequency resolution is not greater than $\Delta\nu_1$, ν_1 can be deemed constant over the entire fluence range. The frequency ν_2 is approximately constant at fluences that are smaller than $F_2 \approx 100$ μJ/cm^2. At higher fluences ν_2 increases by $\Delta\nu_2 \approx 250$ GHz.

5.4 Conclusions

From the measurements over a wide temperature and excitation fluence range in $(TaSe_4)_2I$ it follows that the dynamics of recovery of the CDW parameter shows a qualitatively similar temperature and intensity dependence as the recovery of the CDW order parameter in $K_{0.3}MoO_3$ and $Rb_{0.3}MoO_3$. The lack of excitation intensity dependence in relaxation dynamics at low temperatures suggests that the slowing-down of dynamics, predicted by the RT model in both weak- and strong-bottleneck regimes, is not valid for $(TaSe_4)_2I$.

In short, we have found only indications of different physics in weakly and strongly coupled systems. It follows from the excitation intensity measurements that the saturation energy E_{sat} corresponds to the theoretically predicted mean-field value within the errorbars, however it is noteworthy that the measured E_{sat} is smaller than the predicted value. This is unusual because in principle, one would expect to have to invest a bit more energy to melt the CDW since the absorbed energy is always distributed between the phonon and electron subsystems. This means that measuring a higher E_{sat} than the theoretically predicted value is expected and has also been observed in high temperature superconductors [28], however a lower E_{sat} could be a consequence of strong coupling in $(TaSe_4)_2I$.

It is difficult to assign the different exponential signals and we lack a theoretical model to compare the signals to. We have observed that both electronic signal amplitudes show a saturation behavior with increasing intensity suggesting that both are fingerprints of the order parameter dynamics. The same can also be concluded from the temperature dependence of both electronic signal amplitudes that show a very universal temperature dependence that is similar to the temperature dependence of the amplitudes in $K_{0.3}MoO_3$.

Finally, the temperature and intensity dependency of the phonons seem to rule out the 2.6 THz phonon as the AM due to a substantial increase in frequency with increasing temperature. However, we see no good reason why the 100 GHz transversal optical mode could not be assigned as the dominant mode contributing to the AM in $(TaSe_4)_2I$.

Chapter 6

Summary and Conclusions

Femtosecond time-resolved (TR) optical spectroscopy is a rather new tool for studying dynamics and associated low energy electronic structure in correlated electron systems [23, 24, 30–33, 38–42]. In this technique sample under investigation is photoexcited by a femtosecond optical pulse and the resulting relaxation dynamics is measured by following the dynamics of changes in the dielectric function as a function of the time delay after perturbation with a short pulse in the time domain. It is however important to emphasize that the relation between the recorded reflectivity change transients and their associated physical processes is usually not straightforward. Some signal components can easily be recognized by complementary methods, e.g. coherent oscillations can be compared to the Raman phonon spectra, whereas the assignment of others can pose a serious experimental and theoretical challenge. To determine the origin of the multicomponent signal, one needs to systematically change important system parameters, e.g. temperature, electric field, pressure, etc. and analyze the subsequent changes in the signal transients.

In the case of the first data obtained by *femtosecond time-resolved spectroscopy* on a quasi one dimensional CDW material, i.e. $K_{0.3}MoO_3$ [23], dramatic changes in the dynamics of the fast signal ($\tau \approx 200$ fs) were observed upon cooling through the CDW transition temperature which led people to associate this component with the order parameter. The abrupt drop of the amplitude of the fast transient and the relaxation time divergence were explained in terms of fast thermalization ($\tau \approx 10$ fs) of quasiparticles (QP) and phonons, causing a bottleneck in the relaxation of QP. Effectively, this is the RT scenario in the strong bottleneck regime which is described in more detail in Appendix A. Importantly, the model predicts divergence of the QP relaxation time at low temperatures with decreasing excitation intensity, which was not addressed in the original paper [23] due to heating problems. However, several arguments could be made against the simple RT model interpreted in CDWs, where the main argument against

it is the lack of any measurements confirming the existence of phonons with energies surpassing the CDW gap 2Δ.

The RT predictions and contrary arguments, together with the potential that advances in ultrafast laser systems brought, helped us realize that further experiments should help us better understand the CDW physics in $K_{0.3}MoO_3$ and perhaps in general. This motivated us to systematically investigate the relaxation dynamics of the photoinduced (PI) reflectivity changes in $K_{0.3}MoO_3$ as a function of temperature (4 K – 300 K), excitation intensity and applied electric field. When comparing our experiments to the original paper [23], we should emphasize that not only were we able to measure at temperatures below 50 K, but we also added new degrees of freedom that were the applied electric field and the ability to change the excitation intensity by more than four orders of magnitude. We found that the mechanism governing the recovery of the order parameter needs to be revisited because while the observed divergence in relaxation time near the transition temperature [23] suggests qualitatively similar processes as in superconductors, the complete absence of excitation intensity dependence in relaxation dynamics suggests that this is not the case. Additionally, the lack of excitation intensity and applied electric field dependence of the second relaxation process ($\tau_2 \approx 10$ ps) suggests that this process is not related to the dynamics of the phase mode as was tentatively suggested in the original paper [23]. Instead, we suggest that the two different time-scales may stem from the experimental observation that the two subsystems (i.e. electrons and lattice) that interact to define the order parameter, are decoupled on very short time-scales. This would mean that on very short time-scales (shorter than the period of the AM) after photoexcitation we can not describe the system with a single (equilibrium) complex order parameter, leading to relaxation dynamics on different time scales. The details of this process are so far unknown since we do not have a microscopic model to describe it.

We have conducted for the first time extensive and systematic studies of the high perturbation regime in $K_{0.3}MoO_3$, where we monitored the PI reflectivity changes as a function of excitation intensity and temperature. We successfully showed that the CDW can be non-thermally melted [29]. We observed good agreement between the measured energy needed to melt the CDW E_{sat}, and the energy gain by the electronic subsystem upon CDW condensation. This, together with the extremely fast order parameter recovery dynamics, and the observation of zone-folded phonons high above E_{sat}, led us to believe that during the process of melting and sub-ps recovery of the electronic modulation the lattice remains nearly frozen. In this picture, the frozen lattice provides a strong potential well for the excited electrons, driving them to reform the charge density modulation on a time scale which is typical for electron-phonon thermalization. In addition,

this picture could be valid for this whole class of low dimensional material, in particular for the systems with strong electron-phonon interactions that lead to phenomena like charge density modulation, because they all exhibit extremely fast order recovery dynamics [10, 23, 24, 40, 41, 43, 118].

Motivated by the possibility of being able to study CDWs using techniques such as *terahertz pump-probe* technique and *ultrafast electron diffraction* to obtain complementary information on CDW physics, we grew several series of thin films of $K_{0.3}MoO_3$ using pulsed laser deposition. We used several characterization tools among which the *femtosecond time-resolved spectroscopy* was one of them. The data suggest that domains of two different phases form in films. So far, we were unable to extract a lot of information about the sizes of the CDW domains, but judging from the fact that the PI transients in film and bulk are qualitatively the same, their minimum size can be estimated to be substantially larger than the CDW coherence length ($\xi \approx 1$ nm – 10 nm). Studies of the strongly coupled $(TaSe_4)_2I$ system were motivated by our desire to learn more about the role of the electron-phonon interaction strength in CDW physics. A systematic study of the PI reflectivity change as a function of temperature implementing *femtosecond time-resolved spectroscopy* revealed that not only is the PI response qualitatively similar in $(TaSe_4)_2I$ and $K_{0.3}MoO_3$, but also that the temperature behavior of the relaxation of the order parameter follows qualitatively the same temperature dependence in both systems.

A systematic study of the PI response in the high-perturbation regime was also performed in $(TaSe_4)_2I$ and we successfully showed that the CDW can be non-thermally melted in this system. The comparably low value of the energy needed to melt the CDW E_{sat} obtained from these measurements could be a consequence of the strong electron-phonon coupling, however this should be for now considered a speculation since E_{sat} and the calculated energy gain by the electronic subsystem upon CDW condensation match within the considerably large experimental errorbars.

Finally we studied also the PI reflectivity oscillations in $(TaSe_4)_2I$ in real time. We recorded and analyzed their temperature and excitation intensity dependence and found our results to be in good agreement with the Raman [148, 149] and Neutron scattering [37] data. We found that the hardening of the 2.6 THz TO mode with increasing temperature seems to rule out the assigment of this mode to the AM. On the other hand the strong softening of the 100 GHz TA mode lends support that this low frequency mode could be the dominant mode contributing to the AM in $(TaSe_4)_2I$. However, we have found from the excitation intensity measurements that the 2.6 THz TO mode saturates before the 100 GHz TA mode, suggesting an interesting interplay between the two modes, which has already been discussed elsewhere [142].

Acknowledgements

First of all, I would like to express my utmost gratitude toward my advisor Assist. Prof. Dr. Jure Demšar for his guidance throughout the course of this work. He has handled his first time role of being an advisor impeccably well. I would also like to thank Assist. Prof. Dr. Viktor Kabanov for many stimulating discussions and invaluable input that helped me better understand my work. I am grateful to Prof. Dragan Mihailović for giving me an opportunity to be a part of his team and for his important scientific input.

Furthermore, I would like to thank all my colleagues at the Complex Matter Department at Jožef Stefan Institute from whom I have learned a lot. Special thanks goes to dr. Primož Kušar, whose enthusiasm and help with the experimental part of my work is greatly appreciated. For their help with the atomic force microscopy, the due thanks goes to dr. Klemen Kunstelj and Jure Strle.

The better part of the experiments presented in this thesis were performed at the University of Konstanz. I am very grateful to Assist. Prof. Dr. Jure Demšar for inviting me there and to Hanjo Schäfer, David Städter and Marcus Beyer for their warm welcome, for the valuable help in the laboratory and for their contributions in the data analysis.

Also, I would like to thank Prof. Katica Biljaković and dr. Damir Starešinić from the Zagreb Institute of Physics for the year long collaboration and especially for sharing with me their vast knowledge. I am indebted to Damir Dominko for his large contribution in growth and characterisation of thin films and to dr. Krešimir Salamon, for performing the low angle X-ray measurements and for his invaluable interpretation of the data.

The thin films were grown at the Laser-Surface-Plasma Interactions Laboratory at the Bucharest National Institute for Lasers, Plasma, and Radiation Physics, thanks to Prof. Ion Mihailescu and his group. Special thanks goes to Gabriel Socol whose expertise was indispensable for growing thin films.

For serving as members of the thesis Commission and for a critical refereeing of the thesis, Prof. Dragan Mihailović, Prof. Katica Biljaković and Assist. Prof. Dr. Viktor Kabanov are warmly acknowledged.

I am grateful to my family for their never ending support.

To my dearest Špela and Junior, you were my greatest inspiration.

Appendix A

Rothwarf-Taylor Model

Studies of nonequilibrium carrier dynamics in materials with an energy gap focus on the identification of relaxation processes and direct measurements of the relaxation times. The theoretical model that has been most commonly used to interpret the dynamics in CDW materials [23], superconductors [24, 34] and heavy fermions [112] is a phenomenological Rothwarf-Taylor (RT) model which describes the evolution of quasiparticle (QP) and high frequency phonon (HFP) populations via a set of two nonlinear differential equations [151], which were shown to follow from the general set of kinetic equations for a superconductor [152]. In this Appendix the RT model is presented and the corresponding analytical soulutions of the model obtained by Kabanov et al. [34] are discussed.

Rothwarf and Taylor have pointed out that electron-phonon coupling should be considered when studying the relaxation [151]. Two QPs excited across the superconducting (SC) gap Δ with energies $\geq \Delta$ can recombine and create a HFP with $\hbar\omega \geq 2\Delta$. A HFP can subsequently break an electron-hole pair so the superconducting recovery is governed by the decay of the HFP population. The dynamics of QP and HFP populations is determined by [151]:

$$\frac{dn}{dt} = I_0 + \eta N - Rn^2 \tag{A.1}$$

$$\frac{dN}{dt} = J_0 - \frac{\eta}{2}N + \frac{R}{2}n^2 - \gamma(N - N_T). \tag{A.2}$$

n and N are concentrations of QPs and HFPs, respectively, η is the probability for electron-hole pair breaking by HFP absorption, and R is the bare QP recombination rate with the creation of a HFP. N_T is the concentration of HFPs in thermal equilibrium

at temperature T, and γ is their decay rate. I_0 and J_0 represent the external sources of QPs and HFPs, respectively (caused by an optical pulse in our case).

There are two channels for HFP decay that must be considered in determining γ. The first of the two is the anharmonic decay of HFP (one must remember that $\hbar\omega \leq 2\Delta$ phonons do not have sufficient energy to break electron-hole pairs) while the second channel is the diffusion of HFP into the crystal [36]. The main temperature dependence of γ appears near the transition temperature due to the closing of the gap [36]. Some temperature dependence is also expected at low temperatures, however because it is very weak γ can be considered to be temperature independent.

Equations A.1 and A.2 can be written in a dimensionless form. To do so, dimensionless QP and HFP concentrations are defined as $q \equiv \frac{R}{\eta}n$ and $p \equiv \frac{R}{\eta}N$, while the dimensionless time and HFP decay rate are $\theta \equiv \eta t$ and $\tilde{\gamma} \equiv \gamma/\eta$. The femtosecond optical pulse is usually shorter than the characteristic SC time scales so I_0 and J_0 can be approximated by δ functions leading to initial concentrations of QPs $q_0 = \frac{R}{\eta}n_0$ and HFP $p_0 = \frac{R}{\eta}N$. Using the new definitions Equations A.1 and A.2 reduce to

$$\frac{dq}{d\theta} = p - q^2, \tag{A.3}$$

$$\frac{dp}{d\theta} = -\frac{p}{2} + \frac{q^2}{2} - \tilde{\gamma}(p - p_T), \tag{A.4}$$

where $p_T = \frac{R}{\eta}N_T$ is the dimensionless concentration of HFPs in thermal equilibrium. The thermal equilibrium concentrations of HFPs and QPs p_T and q_T satisfy the detailed balance equation[1] $p_T = q_T^2$. The initial conditions for Equations A.3 and A.4 are $p(0) = p_0$ and $q(0) = q_0$.

There are several limiting cases to consider. Depending on the intensity of the excitation pulse, the *weak perturbation regime* where $(p_0 - p_T), (q_0 - q_T) \ll 1$ and the *strong perturbation regime* where $(p_0 - p_T), (q_0 - q_T) \gg 1$ can be defined. The decay rate of HFPs $\tilde{\gamma}$ determines how the SC recovery is governed. The case when $\tilde{\gamma} \ll 1$ is called the *strong bottleneck regime* where a quasiequilibrium between QPs and HFPs is established and SC recovery is governed entirely by $\tilde{\gamma}$. The other limiting case when $\tilde{\gamma} \gg 1$ is called the *weak bottleneck regime* where HFPs decay rate is so fast that they don't significantly change the QP dynamics.

[1] This is the solution of Equation A.3 in equilibrium.

In order to determine the limiting cases, the dimensionless thermal QP and HFP concentrations should be estimated. If $D(\omega) = \frac{9\nu\omega^2}{\omega_D^3}$ is the phonon density of states where ω_D is the Debye energy, it follows that the HFP thermal concentration is

$$N_T = \frac{36\nu\Delta^2 T}{\omega_D^3} \exp\left(\frac{-2\Delta}{k_B T}\right). \tag{A.5}$$

On the other hand, the QP density per unit cell volume is given by [36]

$$n_T = N(0)\sqrt{2\pi\Delta k_B T} \exp\left(-\frac{\Delta}{k_B T}\right), \tag{A.6}$$

where $N(0)$ is the electronic density of states per unit cell. Combining the equilibrium solution of Equation A.1 $\frac{\eta}{R} = \frac{n_T^2}{N_T}$ with Equations A.5 and A.6, it follows that

$$\frac{\eta}{R} = \frac{N(0)^2 \pi \omega_D^3}{18\nu\Delta} \tag{A.7}$$

Regardless of the value of η/R, the high perturbation limit is reached when the photoexcitation is close to the density required for complete depletion of the SC state. This can be shown if a temperature $\tilde{T}$ is estimated where $q_{\tilde{T}} \approx 1$ ($n_{\tilde{T}} \approx \eta/R$). It follows that $\tilde{T} \approx \Delta / \ln\left(\frac{\Delta^2 \nu E_F}{\omega_D^3}\right)$, so n_T is comparable to η/R only in the close vicinity of T_c.

A.1 Strong Bottleneck Regime

In the *strong bottleneck regime* the decay rate of the HFP is slow enough ($\tilde{\gamma} \ll 1$) that they govern the recovery of the QPs. Two distinct time scales can be defined. The first time-scale is much shorter while the second one is much longer than the decay rate $\tilde{\gamma}$.

A.1.1 Prebottleneck Dynamics

Prebottleneck dynamics describes the short time scale evolution of QP and HFP concentrations preceding the relaxation when $\theta \leq 1/\gamma$. For such short timescales, there is hardly any decay of HFPs so the last term in Equation A.4 can be neglected. This leads to the conservation law

$$q(\theta) + 2p(\theta) = q_0 + 2p_0 \tag{A.8}$$

Using the conservation law, the solutions for QP and HFP populations can be analytically obtained.

$$q(\theta) = -\frac{1}{4} - \frac{\xi^{-1}}{2} + \frac{\xi^{-1}}{1 - K\exp(-\frac{\theta}{\xi})}, \tag{A.9}$$

$$p(\theta) = \frac{1}{2}\left[\frac{1}{8} + \frac{\xi^{-1}}{2} + \frac{\xi^{-2}}{2} - \frac{\xi^{-1}}{1 - K\exp(-\frac{\theta}{\xi})}\right], \tag{A.10}$$

where constants $\xi^{-1} = \sqrt{\frac{1}{4} + 4p_0 + 2q_0}$ and $K = \frac{4q_0+1-2\xi^{-1}}{4q_0+1+2\xi^{-1}}$ are defined. At times $\theta > 1$ dimensionless concentrations $q(\theta)$ and $p(\theta)$ reach the quasistationary solution

$$\begin{aligned} q_s &= \frac{1}{4}\left(\sqrt{1 + 16p_0 + 8q_0} - 1\right), \\ p_s &= q_s^2. \end{aligned} \tag{A.11}$$

The prebottleneck dynamics depends on the initial populations of QPs and HFPs and two distinct regimes can be characterized by the parameter K. The regime $0 < K \leq 1$ corresponds to the situation when the number of photoexcited quasiparticles is larger than the quasistationary solution (see Equation A.11) so $q(\theta)$ rapidly decreases during the formation of the bottleneck. When $-1 \leq K < 0$, the number of photoexcited HPFs is greater than their quasistationary, so due to Equation A.8, the QP density increases after photoexcitation.

A.1.2 Superconducting State Recovery Dynamics

When times $\theta \geq 1/\tilde{\gamma}$, the HFP decay term determines the dynamics of both concentrations. To describe the recovery, a function $s(\theta) = q(\theta)^2 - p(\theta)$ is introduced. Since QP and HFP concentrations are slowly decreasing, $s(\theta) \approx \tilde{\gamma}(p - p_T)$. Clearly $s(\theta) \ll p, q$ and is a slowly decaying function so $ds/d\theta \ll s$. Therefore the derivative $ds/d\theta = 2q\frac{dq}{d\theta} - \frac{dp}{d\theta}$ can be neglected ($ds/d\theta \approx 0$), which simplifies Equations A.3 and A.4 to

$$[1 + 4q(\theta)]\frac{dq(\theta)}{d\theta} = -2\tilde{\gamma}\left(q(\theta)^2 - q_T^2\right). \tag{A.12}$$

After integration, an analytical solution is obtained

$$-2\tilde{\gamma}\theta = \left(2 + \frac{1}{2q_T}\right) \ln\left[\frac{q - q_T}{q_s - q_T}\right] + \left(2 - \frac{1}{2q_T}\right) \ln\left[\frac{q + q_T}{q_s + q_T}\right]. \tag{A.13}$$

The solutions for prebottleneck and recovery dynamics can be combined to obtain an approximate solution for $q(\theta)$ valid for all times after photoexcitation

$$q(\theta) = q_1(\theta) + q_2(\theta) - q_s, \tag{A.14}$$

where $q_1(\theta)$ and $q_2(\theta)$ are obtained from Equations A.9 and A.13, respectively. To illustrate that Equation A.14 describes the solutions of Equations A.3 and A.4, Kabanov et al. [34] calculated the numerical solution and compared it with the approximation given by Equation A.14 and found excellent agreement for all limiting cases.

A.1.3 Low Temperature Limit

At low temperatures $q_T \ll 1$ so $2 \ll \frac{1}{2q_T}$ can also be assumed which reduces Equation A.13 to

$$q(\theta) = q_T + \frac{2q_T(q_s - q_T)\exp(-\theta/\tau_T)}{(q_s + q_T) - (q_s - q_T)\exp(-\theta/\tau_T)}. \tag{A.15}$$

The relaxation rate in the above equation is $\tau_T^{-1} = 4\tilde{\gamma}q_T$ and is strongly reduced by the temperature dependent factor $q_T \propto n_T$ at low temperatures. This low temperature divergence of relaxation time was originally attributed to bi-particle dynamics [153] where τ is divergent due to strong reduction of the thermal QP density but it was later shown [34] that τ also diverges in the case of a well established bottleneck.

At small times when $\theta \ll \tau_T$ Equation A.15 reduces to $q(\theta) = \frac{q_s}{1+2q_s\tilde{\gamma}\theta}$. This is the same dynamics as that of the bi-particle recombination. The relaxation rate can then be defined as the slope $\tau^{-1} = \frac{|dq/d\theta|}{q_s - q_T}$ at $\theta \to 0$ and is intensity dependent

$$\tau^{-1} = 2\tilde{\gamma}(q_s + q_T). \tag{A.16}$$

The intensity dependence is observed only if $q_s \gg q_T$ in which case τ^{-1} is proportional to the excitation intensity. This is the case for very low temperatures when $k_B T_c \ll \Delta$.

A.1.4 High Temperature Limit

In the high temperature limit $q_T \geq 1$ so $2 \gg \frac{1}{2q_T}$ and Equation A.13 reduces to

$$q(\theta) = \sqrt{q_T^2 + \left(q_s^2 - q_T^2\right) \exp(-\theta/\tau_T)}. \tag{A.17}$$

The relaxation rate above is $\tau_T^{-1} = \tilde{\gamma}$. It is weakly temperature dependent due to intrinsic temperature dependence of $\tilde{\gamma}$. It is intensity independent since it does not depend on q_s or p_s, which is also the case for τ^{-1}.

A.2 Weak Bottleneck Regime

The weak bottleneck regime is realized when $\tilde{\gamma} \gg 1$. At short times when $\theta \approx \tilde{\gamma} \ll 1$ the last term in A.4 is dominant so the solution is

$$p(\theta) = p_T + (p_0 - p_T) \exp(-\tilde{\gamma}\theta). \tag{A.18}$$

The time scale on which the HFP density reaches its thermodynamic value is determined by $\tilde{\gamma}^{-1}$. This is a very short time scale in the weak bottleneck regime so the QP density has not changed yet. This means that p can be substituted with p_T in Equation A.3. Taking into account that $q_T^2 = p_T$ the solution can be obtained

$$q(\theta) = \frac{q_T \left[q_0 + q_T + (q_0 - q_T) \exp(-2q_T\theta)\right]}{q_0 + q_T - (q_0 - q_T) \exp(-2q_T\theta)}. \tag{A.19}$$

The signal slope at $\theta = 0$ is intensity dependent if $q_0 \gg q_T$ with

$$\tau^{-1} = q_0 + q_T, \tag{A.20}$$

which is similar to the case of a strong bottleneck. The main difference between the two regimes is that the absolute value of τ^{-1} is reduced by the HFP decay time in the strong bottleneck case.

A.3 Photoinduced Quasiparticle Density

Solution of Equations A.3 and A.4 allows comparison of the theoretically and experimentally obtained $Q(T)$. In the strong bottleneck regime, the saturation densities are determined by Equation A.11. On the other hand, the initial concentrations can be written as

$$q_0 = q_T + \Delta q, \tag{A.21}$$

$$p_0 = p_T + \Delta p, \tag{A.22}$$

where Δq and Δp are the initially photoinduced concentrations of both species. In the weak perturbation limit where $\Delta q, \Delta p \ll 1$ the amplitude of the signal is given by

$$Q(T) \propto q_s - q_T \approx \frac{2\Delta p + \Delta q}{\sqrt{1 + 16p_T + 8q_T}}. \tag{A.23}$$

If Q is normalized to its low temperature value, $A = Q/Q_{T\to 0K}$ and taking into account that $p_T = q_T^2$ and $q_T = R\frac{n_T}{\eta}$, the temperature dependence of the QPs can be obtained, $n_T \propto A^{-1} - 1$. The relation is expected to be general, irrespective of the gap symmetry which allows direct estimation of the temperature dependence of the QP density in thermal equilibrium.

In the weak bottleneck case, Q should be proportional to the excitation intensity, and temperature independent at low temperatures, while increasing when $T \to T_c$ due to closing of the gap. On the other hand, the amplitude should gradually decrease in the strong bottleneck regime, which is the case for the SC studied so far [34].

Equation A.16 can also be rewritten into a form that allows direct comparison of theory and experimental data. Assuming $\tilde{\gamma}$ to be temperature independent and expressing q_T with Equation A.6, Equation A.16 can be written as

$$\tau(T) = \frac{1}{\Phi + a_1(\Delta T)^{1/2}\exp(-\frac{\Delta}{k_B T})}. \tag{A.24}$$

In the above equation $\Phi = a_2\,(q_s - q_T)$ whereas a_1 and s_2 are fitting parameters. Since $q_s - q_T$ is measured directly (see Equation A.23), the only fitting parameters are a_1, a_2 and Δ. a_1 and a_2 determine the magnitude of q_T and $q_s - q_T$, respectively. This means that at intermediate temperatures, when $q_s - q_T \ll q_T$, τ is governed by the temperature

dependence of q_T showing $\exp(\frac{-\Delta}{k_B T})$ dependence. At low enough temperatures $q_s \gg q_T$ and the relaxation time saturates with decreasing temperature. However since it is inversely proportional to q_s, it diverges with decreasing excitation intensity in the $T \to 0$ limit (also see Equation A.11).

Appendix B

List of publications

Publications in refereed journals

1. A. Tomeljak, H. Schäfer, D. Städter, M. Beyer, K. Biljaković, and J. Demšar. Dynamics of Photoinduced Charge-Density-Wave to Metal Phase Transition in $K_{0.3}MoO_3$. *Phys. Rev. Lett.*, 102(6):066404, 2009.

2. A. Tomeljak, B. Kavčič, H. Schäfer, V.V. Kabanov, D. Mihailović, D. Starešinić, K. Biljaković and J. Demšar. Femtosecond nonequilibrium dynamics in quasi-1D CDW systems $K_{0.3}MoO_3$ and $Rb_{0.3}MoO_3$. *Physica B: Condensed Matter*, 404(3-4):548–551, 2009.

3. A. Drenik, A. Tomeljak, M. Mozetič, A. Vesel, D. Babič and M. Balat. Behaviour of neutral hydrogen atom density in the presence of a sample holder in a plasma reactor. *Vacuum*, 84(1):90–93, 2009.

Conference proceedings

1. A. Tomeljak, T. Mertelj, D. Mihailović, I. Bergenti, V. Dediu. Photoinduced insulator-metal transition in (Pr,Ca)MnO_3 : ultrafast optical reflectivity study. *Ultrafast dynamics of collective excitations in solids, 355. WE-Heraeus-Seminar, Vitte, Hiddensee island, Germany.* Wilhelm und Else Heraeus-Stiftung, 2005, p. 100.

2. A. Tomeljak, J. Demšar, A. J. Taylor, F. Galli, J. A. Mydosh. Femtosecond real-time studies of $Lu_5Ir_4Si_{10}$ charge wave compounds. *SKRADIN'06 workshop, Recent developments in low dimensional charge density wave conductors, programe and [extended] abstracts*, 2006. - p. 56.

3. D. Dominko, A. Tomeljak, D Mihailović, J. Demšar. Growing thin films of charge density wave system $Rb_{0.3}MoO_3$ by pulsed laser deposition. *Functionalized nanoscale materials, devices and systems, proceedings of the NATO Advanced Study Institute on Functionalized Nanoscale Materials, Devices and Systems for Chem. -bio Sensors, Photonics, and Energy Generation and Storage. (NATO science for peace and security series, seria B, Physics and biophysics)* / editors A. Vaseashta, I. N. Mihailescu. Dordrecht; London: Springer, 2008. - p. 399-402.

4. A. Tomeljak, J. Demšar. Thin-films of a charge density wave compound $Rb_{0.3}MoO_3$. *EUROMAT 2007.* Deutsche Gesellschaft fr Materialkunde, 2007.

5. A. Tomeljak, B. Kavčič, V.V. Kabanov, D. Mihailović, D. Starešinić, K. Biljaković and J. Demšar. Femtosecond nonequilibrium dynamics in quasi-1D CDW systems $K_{0.3}MoO_3$ and $Rb_{0.3}MoO_3$. *Program and abstracts / International Workshop on Electronic Crystals, ECRYS-2008*, 2008.

Bibliography

[1] A. H. Zewail. Femtochemistry: Atomic-scale dynamics of the chemical bond using ultrafast lasers, 1999. Nobel lecture.

[2] C Rischel, A Rousse, I Uschmann, PA Albouy, JP Geindre, P Audebert, JC Gauthier, E Forster, JL Martin, and A Antonetti. Femtosecond time-resolved X-ray diffraction from laser-heated organic films. *Nature*, 390(6659):490–492, 1997.

[3] C Rose-Petruck, R Jimenez, T Guo, A Cavalleri, CW Siders, F Raksi, JA Squier, BC Walker, KR Wilson, and CPJ Barty. Picosecond-milliangstrom lattice dynamics measured by ultrafast X-ray diffraction. *Nature*, 398(6725):310–312, 1999.

[4] A. Cavalleri, Cs. Tóth, C. W. Siders, J. A. Squier, F. Ráksi, P. Forget, and J. C. Kieffer. Femtosecond Structural Dynamics in VO_2 during an Ultrafast Solid-Solid Phase Transition. *Phys. Rev. Lett.*, 87(23):237401, 2001. doi: 10.1103/PhysRevLett.87.237401.

[5] C. W. Siders, A. Cavalleri, K. Sokolowski-Tinten, Cs. Tóth, T. Guo, M. Kammler, M. Horn von Hoegen, K. R. Wilson, D. von der Linde, and C. P. J. Barty. Detection of Nonthermal Melting by Ultrafast X-ray Diffraction. *Science*, 286(5443):1340–1342, 1999. doi: 10.1126/science.286.5443.1340. URL `http://www.sciencemag.org/cgi/content/abstract/286/5443/1340`.

[6] Lin X. Chen, Wighard J. H. Jager, Guy Jennings, David J. Gosztola, Anneli Munkholm, and Jan P. Hessler. Capturing a Photoexcited Molecular Structure Through Time-Domain X-ray Absorption Fine Structure. *Science*, 292(5515):262–264, 2001. doi: 10.1126/science.1057063. URL `http://www.sciencemag.org/cgi/content/abstract/292/5515/262`.

[7] Bradley J. Siwick, Jason R. Dwyer, Robert E. Jordan, and R. J. Dwayne Miller. An Atomic-Level View of Melting Using Femtosecond Electron Diffraction. *Science*, 302(5649):1382–1385, 2003. doi: 10.1126/science.1090052. URL `http://www.sciencemag.org/cgi/content/abstract/302/5649/1382`.

[8] Hyotcherl Ihee, Vladimir A. Lobastov, Udo M. Gomez, Boyd M. Goodson, Ramesh Srinivasan, Chong-Yu Ruan, and Ahmed H. Zewail. Direct Imaging of Transient Molecular Structures with Ultrafast Diffraction. *Science*, 291(5503):458–462, 2001. doi: 10.1126/science.291.5503.458. URL `http://www.sciencemag.org/cgi/content/abstract/291/5503/458`.

[9] Bradley J. Siwick, Jason R. Dwyer, Robert E. Jordan, and R. J. Dwayne Miller. Ultrafast electron optics: Propagation dynamics of femtosecond electron packets. *Journal of Applied Physics*, 92(3):1643–1648, 2002. doi: 10.1063/1.1487437. URL `http://link.aip.org/link/?JAP/92/1643/1`.

[10] L. Perfetti, P. A. Loukakos, M. Lisowski, U. Bovensiepen, H. Berger, S. Biermann, P. S. Cornaglia, A. Georges, and M. Wolf. Time Evolution of the Electronic Structure of 1T-TaS_2 through the Insulator-Metal Transition. *Physical Review Letters*, 97(6):067402, 2006. doi: 10.1103/PhysRevLett.97.067402. URL `http://link.aps.org/abstract/PRL/v97/e067402`.

[11] L Perfetti, P A Loukakos, M Lisowski, U Bovensiepen, M Wolf, H Berger, S Biermann, and A Georges. Femtosecond dynamics of electronic states in the Mott insulator 1T-TaS_2 by time resolved photoelectron spectroscopy. *New Journal of Physics*, 10(5):053019 (17pp), 2008. URL `http://stacks.iop.org/1367-2630/10/053019`.

[12] U Keller. Recent developments in compact ultrafast lasers. *Nature*, 424(6950):831–838, 2003. doi: 10.1038/nature01938.

[13] J. Shah. *Ultrafast Spectroscopy of Semi-conductors and Semiconductor Nanostructures.* Springer Verlag, 1999.

[14] P. Kusar, J. Demsar, D. Mihailovic, and S. Sugai. A systematic study of femtosecond quasiparticle relaxation processes in $La_{2-x}Sr_xCuO_4$. *Phys. Rev. B*, 72(1):014544, Jul 2005. doi: 10.1103/PhysRevB.72.014544.

[15] M. L. Schneider, J. Demsar, Y. Glinka, A. Klimov, A. Krapf, S. Rast, Y. H. Ren, Weidong Si, Y. Xu, X. H. Zeng, I. Bozovic, G. Lpke, R. Manzke, R. Sobolewski, A. T. Taylor, N. H. Tolk, X. X. Xi, R. Joynt, and M. Onellion. Ultrafast carrier relaxation dynamics in single-layer cuprates. *EPL (Europhysics Letters)*, 60(3):460, 2002. URL `http://stacks.iop.org/0295-5075/60/i=3/a=460`.

[16] G. P. Segre, N. Gedik, J. Orenstein, D. A. Bonn, Ruixing Liang, and W. N. Hardy. Photoinduced changes of reflectivity in single crystals of yba$_2$cu$_3$o$_{6.5}$ (ortho ii). *Phys. Rev. Lett.*, 88(13):137001, Mar 2002. doi: 10.1103/PhysRevLett.88.137001.

[17] D. Mihailovic and J. Demsar. Time-Resolved Optical Studies of Quasiparticle Dynamics in High-Temperature Superconductors : Experiments and Theory *in Spectrosopy of Superconducting Materials*, chapter 16, pages 230–244. ACS Symposium Series 730. The American Chemical Society: Washington, D.C., 1999.

[18] Robert A. Kaindl, Marc A. Carnahan, Daniel S. Chemla, Seongshik Oh, and James N. Eckstein. Dynamics of Cooper pair formation in $Bi_2Sr_2CaCu_2O_{8+\delta}$. *Phys. Rev. B*, 72 (6):060510, Aug 2005. doi: 10.1103/PhysRevB.72.060510.

[19] R. D. Averitt, A. I. Lobad, C. Kwon, S. A. Trugman, V. K. Thorsmølle, and A. J. Taylor. Ultrafast Conductivity Dynamics in Colossal Magnetoresistance Manganites. *Phys. Rev. Lett.*, 87(1):017401, Jun 2001. doi: 10.1103/PhysRevLett.87.017401.

[20] T Mertelj, AA Bosak, OY Gorbenko, AR Kaul, and D Mihailovic. Ultrafast optical response in giant magnetoresistance manganites. *Int. J. Mod. Phys. B*, 14(29-31):3584–3589, 2000.

[21] T. Ogasawara, T. Kimura, T. Ishikawa, M. Kuwata-Gonokami, and Y. Tokura. Dynamics of photoinduced melting of charge/orbital order in a layered manganite $La_{0.5}Sr_{1.5}MnO_4$. *Phys. Rev. B*, 63(11):113105, Mar 2001. doi: 10.1103/PhysRevB.63.113105.

[22] O. V. Misochko, E. M. Kaidashev, N. Georgiev, T. Dekorsy, and I. N. Zakharchenko. A time-resolved optical study of the paramagnetic dielectric-ferromagnetic metal transition in $La_{0.7}Ca_{0.3}MnO_3$. *J. Exp. Theor. Phys.*, 97(4):788–793, 2003. doi: 10.1134/1.1625069. URL `http://www.springerlink.com/content/c12139n37w1619m8`.

[23] J. Demsar, K. Biljaković, and D. Mihailovic. Single Particle and Collective Excitations in the One-Dimensional Charge Density Wave Solid $K_{0.3}MoO_3$ Probed in Real Time by Femtosecond Spectroscopy. *Phys. Rev. Lett.*, 83(4):800–803, Jul 1999. doi: 10.1103/PhysRevLett.83.800.

[24] J. Demsar, L. Forró, H. Berger, and D. Mihailovic. Femtosecond snapshots of gap-forming charge-density-wave correlations in quasi-two-dimensional dichalcogenides 1T-TaS_2 and 2H-$TaSe_2$. *Phys. Rev. B*, 66(4):041101, 2002. doi: 10.1103/PhysRevB.66.041101.

[25] J. Demsar, R. D. Averitt, K. H. Ahn, M. J. Graf, S. A. Trugman, V. V. Kabanov, J. L. Sarrao, and A. J. Taylor. Quasiparticle Relaxation Dynamics in Heavy Fermion Compounds. *Phys. Rev. Lett.*, 91(2):027401, 2003. doi: 10.1103/PhysRevLett.91.027401.

[26] K. H. Ahn, M. J. Graf, S. A. Trugman, J. Demsar, R. D. Averitt, J. L. Sarrao, and A. J. Taylor. Ultrafast quasiparticle relaxation dynamics in normal metals and heavy-fermion materials. *Phys. Rev. B*, 69(4):045114, Jan 2004. doi: 10.1103/PhysRevB.69.045114.

[27] M. Rinni, R. Tobey, N. Dean, J. Itatani, Y. Tomioka, Y. Tokura, R. W. Schoenlein, and A. Cavalleri. Control of the electronic phase of a manganite by mode-selective vibrational excitation. *Nature*, 449(7158):72, 2007. doi: 10.1038/nature06119. URL `http://dx.doi.org/10.1038/nature06119`.

[28] P. Kusar, V. V. Kabanov, J. Demsar, T. Mertelj, S. Sugai, and D. Mihailovic. Controlled Vaporization of the Superconducting Condensate in Cuprate Superconductors by Femtosecond Photoexcitation. *Physical Review Letters*, 101(22):227001, 2008. doi: 10.1103/PhysRevLett.101.227001. URL `http://link.aps.org/abstract/PRL/v101/e227001`.

[29] A. Tomeljak, H. Schäfer, D. Städter, M. Beyer, K. Biljakovic, and J. Demsar. Dynamics of Photoinduced Charge-Density-Wave to Metal Phase Transition in $K_{0.3}MoO_3$. *Phys. Rev. Lett.*, 102(6):066404, 2009. doi: 10.1103/PhysRevLett.102.066404. URL `http://link.aps.org/abstract/PRL/v102/e066404`.

[30] D. Mihailovic, D. Dvorsek, V. V. Kabanov, J. Demsar, L. Forró, and H. Berger. Femtosecond data storage, processing, and search using collective excitations of a macroscopic quantum state. *Applied Physics Letters*, 80(5):871–873, 2002. doi: 10.1063/1.1447594. URL `http://link.aip.org/link/?APL/80/871/1`.

[31] A.A. Tsvetkov, D.M. Sagar, P.H.M. van Loosdrecht, D. van der Marel, and S. van Smaalen. Selective Coherent Excitation of Charge Density Waves. *Acta Physica Polonica B*, 34(2): 384, 2003.

[32] Yuhang Ren, Gunter Lüpke, and Zhu'an Xu. Photoinduced charge-density-wave dynamics in $K_{0.3}MoO_3$. *Applied Physics Letters*, 84(12):2169–2171, 2004. doi: 10.1063/1.1689391. URL `http://link.aip.org/link/?APL/84/2169/1`.

[33] Attila Virosztek and Kazumi Maki. Collective modes in charge-density waves and long-range Coulomb interactions. *Phys. Rev. B*, 48(3):1368–1372, Jul 1993. doi: 10.1103/PhysRevB.48.1368.

[34] V. V. Kabanov, J. Demsar, and D. Mihailovic. Kinetics of a Superconductor Excited with a Femtosecond Optical Pulse. *Phys. Rev. Lett.*, 95(14):147002, Sep 2005. doi: 10.1103/PhysRevLett.95.147002.

[35] A. Tomeljak, B. Kavcic, H. Schfer, V.V. Kabanov, D. Mihailovic, D. Staresinic, K. Biljakovic, and J. Demsar. Femtosecond nonequilibrium dynamics in quasi-1D CDW systems $K_{0.3}MoO_3$ and $Rb_{0.3}MoO_3$. *Physica B: Condensed Matter*, 404(3-4):548 – 551, 2009.

doi: DOI:10.1016/j.physb.2008.11.049. URL http://www.sciencedirect.com/science/article/B6TVH-4V0TD4F-C/2/988faa9fd850c296a641e432ada2c154.

[36] V. V. Kabanov, J. Demsar, B. Podobnik, and D. Mihailovic. Quasiparticle relaxation dynamics in superconductors with different gap structures: Theory and experiments on $YBa_2Cu_3O_{7-\delta}$. *Phys. Rev. B*, 59(2):1497–1506, Jan 1999. doi: 10.1103/PhysRevB.59.1497.

[37] J E Lorenzo, R Currat, P Monceau, B Hennion, H Berger, and F Levy. A neutron scattering study of the quasi-one-dimensional conductor $(TaSe_4)_2I$. *Journal of Physics: Condensed Matter*, 10(23):5039, 1998. URL http://stacks.iop.org/0953-8984/10/i=23/a=010.

[38] Y. Toda, K. Tateishi, and S. Tanda. Anomalous coherent phonon oscillations in the commensurate phase of the quasi-two-dimensional 1T- TaS_2 compound. *Phys. Rev. B*, 70(3): 033106, Jul 2004. doi: 10.1103/PhysRevB.70.033106.

[39] K. Shimatake, Y. Toda, and S. Tanda. Quenching of phase coherence in quasi-one-dimensional ring crystals. *Physical Review B (Condensed Matter and Materials Physics)*, 73(15):153403, 2006. doi: 10.1103/PhysRevB.73.153403.

[40] K. Shimatake, Y. Toda, and S. Tanda. Selective optical probing of the charge-density-wave phases in $NbSe_3$. *Physical Review B (Condensed Matter and Materials Physics)*, 75(11): 115120, 2007. doi: 10.1103/PhysRevB.75.115120. URL http://link.aps.org/abstract/PRB/v75/e115120.

[41] Dodderi M Sagar, Artem A Tsvetkov, Daniele Fausti, Sander van Smaalen, and Paul H M van Loosdrecht. Coherent amplitudon generation in blue bronze through ultrafast interband quasi-particle decay. *Journal of Physics: Condensed Matter*, 19(34):346208 (12pp), 2007. URL http://stacks.iop.org/0953-8984/19/346208.

[42] R. V. Yusupov, T. Mertelj, J.-H. Chu, I. R. Fisher, and D. Mihailovic. Single-Particle and Collective Mode Couplings Associated with 1- and 2-Directional Electronic Ordering in Metallic RTe_3 (R = Ho,Dy,Tb). *Physical Review Letters*, 101(24):246402, 2008. doi: 10.1103/PhysRevLett.101.246402. URL http://link.aps.org/abstract/PRL/v101/e246402.

[43] F. Schmitt, P. S. Kirchmann, U. Bovensiepen, R. G. Moore, L. Rettig, M. Krenz, J.-H. Chu, N. Ru, L. Perfetti, D. H. Lu, M. Wolf, I. R. Fisher, and Z.-X. Shen. Transient Electronic Structure and Melting of a Charge Density Wave in $TbTe_3$. *Science*, 321(5896): 1649–1652, 2008. doi: 10.1126/science.1160778. URL http://www.sciencemag.org/cgi/content/abstract/321/5896/1649.

[44] H. Fröhlich. On the Theory of Superconductivity: The One-Dimensional Case. *Proceedings of the Royal Society of London. Series A. Mathematical and Physical Sciences*, 223(1154):296–305, 1954. doi: 10.1098/rspa.1954.0116. URL http://rspa.royalsocietypublishing.org/content/223/1154/296.abstract.

[45] R. E. Peierls. *Quantum Theory of Solids*. Oxford U.P., London, 1955.

[46] J. Sólyom. The Fermi gas model of one-dimensional conductors. *Advances in Physics*, 28 (2):201–303, 1979. doi: 10.1080/00018737900101375. URL http://www.informaworld.com/10.1080/00018737900101375.

[47] H. R. Zeller. in *Solid State physics*, volume 13, page 31. Vieweg, Stuttgart, 1973.

[48] P. Monçeau, N. P. Ong, A. M. Portis, A. Meerschaut, and J. Rouxel. Electric Field Breakdown of Charge-Density-Wave Induced Anomalies in $NbSe_3$. *Phys. Rev. Lett.*, 37 (10):602–606, Sep 1976. doi: 10.1103/PhysRevLett.37.602.

[49] N. P. Ong and Pierre Monceau. Anomalous transport properties of a linear-chain metal: $NbSe_3$. *Phys. Rev. B*, 16(8):3443–3455, Oct 1977. doi: 10.1103/PhysRevB.16.3443.

[50] A. H. Thompson, A. Zettl, and G. Grüner. Charge-Density-Wave Transport in TaS_3. *Phys. Rev. Lett.*, 47(1):64–67, Jul 1981. doi: 10.1103/PhysRevLett.47.64.

[51] G. Grüner, A. Zettl, W. G. Clark, and A. H. Thompson. Observation of narrow-band charge-density-wave noise in TaS_3. *Phys. Rev. B*, 23(12):6813–6815, Jun 1981. doi: 10.1103/PhysRevB.23.6813.

[52] William Fogle and Jerome H. Perlstein. Semiconductor-to-Metal Transition in the Blue Potassium Molybdenum Bronze, $K_{0.30}MoO_3$; Example of a Possible Excitonic Insulator. *Phys. Rev. B*, 6(4):1402–1412, Aug 1972. doi: 10.1103/PhysRevB.6.1402.

[53] A. Wold, W. Kunnmann, R. J. Arnott, and A. Ferretti. Preparation and Properties of Sodium and Potassium Molybdenum Bronze Crystals. *Inorganic Chemistry*, 3(4):545–547, 1964. doi: 10.1021/ic50014a022. URL `http://pubs.acs.org/doi/abs/10.1021/ic50014a022`.

[54] G. Travaglini, P. Wachter, J. Marcus, and C. Schlenker. The blue bronze $K_{0.3}MoO_3$: A new one-dimensional conductor. *Solid State Communications*, 37(7):599 – 603, 1981. ISSN 0038-1098. doi: DOI:10.1016/0038-1098(81)90143-5. URL `http://www.sciencedirect.com/science/article/B6TVW-46MFD3D-1T8/2/05c189dd1b55fbcef7362c3c3588d12b`.

[55] E. J. Woll and W. Kohn. Images of the Fermi Surface in Phonon Spectra of Metals. *Phys. Rev.*, 126(5):1693–1697, Jun 1962. doi: 10.1103/PhysRev.126.1693.

[56] Mingliang Tian, Lin Chen, and Yuheng Zhang. Temperature dependence of the structural parameters of the host lattice in blue bronze $K_{0.3}MoO_3$. *Phys. Rev. B*, 62(3):1504–1507, Jul 2000. doi: 10.1103/PhysRevB.62.1504.

[57] R. S. Kwok and S. E. Brown. Thermal conductivity of the charge-density-wave systems $K_{0.3}MoO_3$ and $(TaSe_4)_2I$ near the Peierls transition. *Phys. Rev. Lett.*, 63(8):895–898, Aug 1989. doi: 10.1103/PhysRevLett.63.895.

[58] R. S. Kwok, G. Gruner, and S. E. Brown. Fluctuations and thermodynamics of the charge-density-wave phase transition. *Phys. Rev. Lett.*, 65(3):365–368, Jul 1990. doi: 10.1103/PhysRevLett.65.365.

[59] J. W. Brill, M. Chung, Y. K. Kuo, X. Zhan, E. Figueroa, and George Mozurkewich. Thermodynamics of the Charge-Density-Wave Transition in Blue Bronze. *Phys. Rev. Lett.*, 74(7):1182–1185, Feb 1995. doi: 10.1103/PhysRevLett.74.1182.

[60] George Grüner. *Density Waves in Solids*, volume 89 of *Frontiers in Physics*. Addison-Wesley Publishing Company, 1994.

[61] P. Monceau. *Electronic Properties of Quasi One-Dimensional Compounds*. D. Reidel Publishing Company, 1. edition, 1985.

[62] Neil W. Ashcroft and David N. Mermin. *Solid State Physics*. Thomson Learning, Toronto, January 1976. ISBN 0030839939.

[63] Charles Kittel. *Introduction to Solid State Physics*. John Wiley & Sons, NY, 8th edition edition, November 2005. ISBN 047141526X.

[64] J. Bardeen, L. N. Cooper, and J. R. Schrieffer. Theory of Superconductivity. *Phys. Rev.*, 108(5):1175–1204, Dec 1957. doi: 10.1103/PhysRev.108.1175.

[65] V. L. Ginzburg and L. D. Landau. On the Theory of superconductivity. *Zh. Eksp. Teor. Fiz.*, 20:1064–1082, 1950.

[66] A. A. Abrikosov, L. Gorkov, and I. Dzyaloshinsky. *Methods of Quantum Field Theory in Statistical Physics (Selected Russian Publications in the Mathematical Sciences.)*. Dover Publications Inc., new ed edition, April 1976. ISBN 0486632288.

[67] R. M. Fleming. Electric-field depinning of charge-density waves in $NbSe_3$. *Physical Review B*, 22(5606), 1980.

[68] H. Fujishitaa, M. Satoa, and Hoshinoa S. Incommensurate superlattice reflections in quasi one dimensional conductors, $(MSe_4)_2I$ (M=Ta and Nb). *Solid State Communications*, 49 (4):313–316, 1984.

[69] M Sato, H Fujishita, and S Hosnino. Neutron scattering study on the structural transition of quasi-one-dimensional conductor $K_{0.3}MoO_3$. *Journal of Physics C: Solid State Physics*, 16(24):L877–L882, 1983. URL `http://stacks.iop.org/0022-3719/16/L877`.

[70] L.D. Landau and EM. Lifschitz. *Statistical Physics*. Pergamon Press, London, 1959.

[71] P. A. Lee, T. M. Rice, and P. W. Anderson. Conductivity from charge or spin density waves. *Solid State Comm.*, 14(8):703–709, 1974.

[72] P.W. Anderson. *Basic Notions in Condensed Matter Physics*. Benjamin-Cummings, Redwood City, CA, 1984.

[73] Yoshinori Nakane and Satoshi Takada. Theory of Sound Wave and Phason in a Quasi One-Dimensional Incommensurate CDW System I. —*Long-Range Coulomb Effect*—. *Journal of the Physical Society of Japan*, 54(3):977–988, 1985. doi: 10.1143/JPSJ.54.977. URL `http://jpsj.ipap.jp/link?JPSJ/54/977/`.

[74] K. Y. M. Wong and S. Takada. Effects of quasiparticle screening on collective modes: Incommensurate charge-density-wave systems. *Phys. Rev. B*, 36(10):5476–5492, Oct 1987. doi: 10.1103/PhysRevB.36.5476.

[75] E. Tuti and S. Bariić. Dynamic structure factor of a one-dimensional Peierls system. *Phys. Rev. B*, 43(10):8431–8436, Apr 1991. doi: 10.1103/PhysRevB.43.8431.

[76] J. P. Pouget, B. Hennion, C. Escribe-Filippini, and M. Sato. Neutron-scattering investigations of the Kohn anomaly and of the phase and amplitude charge-density-wave excitations of the blue bronze $K_{0.3}MoO_3$. *Phys. Rev. B*, 43(10):8421–8430, Apr 1991. doi: 10.1103/PhysRevB.43.8421.

[77] R. Comes and G. Shirane. *Highly Conducting One Dimensional Solids*, page 17. Plenum, New York, 1979.

[78] K. Carneiro, G. Shirane, S. A. Werner, and S. Kaiser. Lattice dynamics of $K_2Pt(CN)_4Br_{0.3}{\cdot}3.2\ D_2O$ (KCP) studied by inelastic neutron scattering. *Phys. Rev. B*, 13 (10):4258–4273, May 1976. doi: 10.1103/PhysRevB.13.4258.

[79] G. Shirane, S. M. Shapiro, R. Comès, A. F. Garito, and A. J. Heeger. Phonon dispersion and Kohn anomaly in tetrathiafulvalene-tetracyanoquinodimethane (TTF-TCNQ). *Phys. Rev. B*, 14(6):2325–2334, Sep 1976. doi: 10.1103/PhysRevB.14.2325.

[80] G. Grüner. The dynamics of charge-density waves. *Rev. Mod. Phys.*, 60(4):1129–1181, Oct 1988. doi: 10.1103/RevModPhys.60.1129.

[81] L. Degiorgi, B. Alavi, G. Mihály, and G. Grüner. Complete excitation spectrum of charge-density waves: Optical experiments on $K_{0.3}MoO_3$. *Phys. Rev. B*, 44(15):7808–7819, Oct 1991. doi: 10.1103/PhysRevB.44.7808.

[82] D M Sagar, D Fausti, S Yue, C A Kuntscher, S van Smaalen, and P H M van Loosdrecht. A Raman study of the charge-density-wave state in $A_{0.3}MoO_3$ (A = K, Rb). *New Journal of Physics*, 10(2):023043 (11pp), 2008. URL `http://stacks.iop.org/1367-2630/10/023043`.

[83] K Nomura, K Kume, and M Sato. Direct evidence for the sliding motion of CDW-the motional narrowing of ^{87}Rb NMR. *Journal of Physics C: Solid State Physics*, 19(13): L289–L292, 1986. URL `http://stacks.iop.org/0022-3719/19/L289`.

[84] A. Jánossy, C. Berthier, P. Ségransan, and P. Butaud. Measurement of the sliding charge-density-wave phase velocity in $Rb_{0.3}MoO_3$. *Phys. Rev. Lett.*, 59(20):2348–2351, Nov 1987. doi: 10.1103/PhysRevLett.59.2348.

[85] S. Aubry and P. Quemerais. *Low-Dimensional Properties of Molybdenum Bronzes and Oxides*, page 295. Dordrecht: Kluwer Academic, 1989.

[86] Serge Aubry, Gilles Abramovici, and Jean-Luc Raimbault. Chaotic polaronic and bipolaronic states in the adiabatic Holstein model. *Journal of Statistical Physics*, 67(3):675–780, 1992. doi: 10.1007/BF01049725. URL `http://www.springerlink.com/content/u32764h21385g6q2`.

[87] A S Alexandrov and N F Mott. Do pairs exist above T_c? *Superconductor Science and Technology*, 6(4):215–224, 1993. URL `http://stacks.iop.org/0953-2048/6/215`.

[88] J. Ranninger. The polaron scenario for high T_c superconductivity. *Physica C: Superconductivity*, 235-240(Part 1):277 – 280, 1994. ISSN 0921-4534. doi: DOI:10.1016/0921-4534(94)91368-4. URL `http://www.sciencedirect.com/science/article/B6TVJ-46V0GX5-2V/2/465c902b72129bd3968a28d0d5ae18e1`.

[89] J.C. Diels and W. Rudolf. *Ultrashort Laser Pulse Phenomena*. Academic Press, Inc., 1996.

[90] P. M. W. French. The generation of ultrashort laser pulses. *Reports on Progress in Physics*, 58:169–262, 1995.

[91] M. Nisoli, S. De Silvestri, and O. Svelto. Generation of high energy 10 fs pulses by a new pulse compression technique. *Applied Physics Letters*, 68(20):2793–2795, 1996. doi: 10.1063/1.116609. URL `http://link.aip.org/link/?APL/68/2793/1`.

[92] Jeff Squier, Frangçois Salin, Gerard Mourou, and Donald Harter. 100-fs pulse generation and amplification in Ti:AI_2O_3. *Opt. Lett.*, 16(5):324–326, 1991. URL `http://ol.osa.org/abstract.cfm?URI=ol-16-5-324`.

[93] *Operator's Manual - The Coherent Mira Seed Laser*. Coherent, Inc., Santa Clara, CA, 1997.

[94] Bahaa E. A. Saleh and Malvin Carl Teich. *Fundamentals of Photonics*. John Wiley & Sons, New York, 1991.

[95] *Operator's Manual - RegA Model 9050 Laser*. Coherent, Inc., Santa Clara, CA, 1997.

[96] A. Yariv. *Quantum Electronics*. John Wiley & Sons, New York, NY, 3rd edition, 1989.

[97] Paul A. Temple. An introduction to phase-sensitive amplifiers: An inexpensive student instrument. *American Journal of Physics*, 43(9):801–807, 1975. doi: 10.1119/1.9690. URL http://link.aip.org/link/?AJP/43/801/1.

[98] Andrej Likar. *Osnove fizikalnih merjenj in merilnih sistemov*. Izbrana poglavja iz fizike. DMFA, 26 edition.

[99] Paul Horowitz and Winfield Hill. *The art of electronics*. Cambridge Univ. Press, Cambridge, 1980.

[100] T. N. Thomas, C. J. Stevens, A. J. S. Choudhary, J. F. Ryan, D. Mihailovic, T. Mertelj, L. Forro, G. Wagner, and J. E. Evetts. Photoexcited carrier relaxation and localization in $Bi_2Sr_2Ca_{1-y}YyCu_2O_8$ and $YBa_2Cu_3O_{7-\delta}$: A study by femtosecond time-resolved spectroscopy. *Phys. Rev. B*, 53(18):12436–12440, May 1996. doi: 10.1103/PhysRevB.53.12436.

[101] J. H. Bechtel. Heating of solid targets with laser pulses. *Journal of Applied Physics*, 46 (4):1585–1593, 1975. doi: 10.1063/1.321760. URL http://link.aip.org/link/?JAP/46/1585/1.

[102] J. Demsar, M. Zavrtanik, B. Podobnik, V. I. Dediu, and D. Mihailovic. Photoresponse of Y-Ba-Cu-O thin rims on the μs time scale-evidence for localized states near E_F. *Journal of Superconductivity and Novel Magnetism*, 10(4):455–458, 1997. doi: 10.1007/BF02765737.

[103] H. S. Carlslaw and J. C. Jaeger. *Conduction of heat in Solids*. Oxford University Press, UK, second edition, 1985.

[104] J. Demšar. *Photoexcited Carrier Relaxation in High Temperature Superconductors probed by Ultrafast Optical Spectroscopy*. PhD thesis, University of Ljubljana, 2000.

[105] Philip B. Allen. Theory of thermal relaxation of electrons in metals. *Phys. Rev. Lett.*, 59 (13):1460–1463, Sep 1987. doi: 10.1103/PhysRevLett.59.1460.

[106] Z. Bihar, D. Staresinic, K. Biljakovic, and T. Sambongi. Charge-density-wave fluctuation contribution to the thermal conductivity of $K_{0.3}Mo0_3$. *EPL (Europhysics Letters)*, 40(1): 73, 1997. URL http://stacks.iop.org/0295-5075/40/i=1/a=073.

[107] T. Mertelj. *Influence of doping on optical phonons in high temperature superconductors*. PhD thesis, University of Ljubljana, 1996.

[108] Z. Vardeny and J. Tauc. Picosecond coherence coupling in the pump and probe technique. *Optics Communications*, 39(6):396 – 400, 1981. ISSN 0030-4018. doi: DOI:10.1016/0030-4018(81)90231-5. URL http://www.sciencedirect.com/science/article/B6TVF-46DF99T-5F/2/97e42288a91e02f4739dda58084336ee.

[109] H. J. Zeiger, J. Vidal, T. K. Cheng, E. P. Ippen, G. Dresselhaus, and M. S. Dresselhaus. Theory for displacive excitation of coherent phonons. *Phys. Rev. B*, 45(2):768–778, Jan 1992. doi: 10.1103/PhysRevB.45.768.

[110] T. E. Stevens, J. Kuhl, and R. Merlin. Coherent phonon generation and the two stimulated Raman tensors. *Phys. Rev. B*, 65(14):144304, Mar 2002. doi: 10.1103/PhysRevB.65.144304.

[111] J. Graham and A. D. Wadsley. The crystal structure of the blue potassium molybdenum bronze, $K_{0.28}MoO_3$. *Acta Crystallographica*, 20(1):93–100, Jan 1966. doi: 10.1107/S0365110X66000173. URL http://dx.doi.org/10.1107/S0365110X66000173.

[112] Jure Demsar, Verner K. Thorsmølle, John L. Sarrao, and Antoinette J. Taylor. Photoexcited Electron Dynamics in Kondo Insulators and Heavy Fermions. *Physical Review Letters*, 96(3):037401, 2006. doi: 10.1103/PhysRevLett.96.037401. URL `http://link.aps.org/abstract/PRL/v96/e037401`.

[113] B. Zawilski, J. Marcus, and T. Klein. A multiple origin for non-linear transport properties in $K_{0.3}MoO_3$ molybdenum blue bronze. *EPL (Europhysics Letters)*, 50(1):75, 2000. URL `http://stacks.iop.org/0295-5075/50/i=1/a=075`.

[114] N. Ogawa, A. Shiraga, R. Kondo, S. Kagoshima, and K. Miyano. Photocontrol of dynamic phase transition in the charge-density wave material $k0.3moo3$. *Phys. Rev. Lett.*, 87(25): 256401, Nov 2001. doi: 10.1103/PhysRevLett.87.256401.

[115] L. R. Testardi. Destruction of Superconductivity by Laser Light. *Phys. Rev. B*, 4(7): 2189–2196, Oct 1971. doi: 10.1103/PhysRevB.4.2189.

[116] J. Demsar, R. D. Averitt, A. J. Taylor, V. V. Kabanov, W. N. Kang, H. J. Kim, E. M. Choi, and S. I. Lee. Pair-Breaking and Superconducting State Recovery Dynamics in MgB_2. *Phys. Rev. Lett.*, 91(26):267002, 2003. doi: 10.1103/PhysRevLett.91.267002.

[117] J. Demsar, R. D. Averitt, A. J. Taylor, W. N. Kang, H. J. Kim, E. M. Choi, and S. I. Lee. Photoinduced Conductivity Dynamics Studies of MgB_2 Thin Films. *Int. J. Mod. Phys. B*, 17(18):3675, 2003.

[118] D. Dvorsek, V. V. Kabanov, K. Biljakovic, and D. Mihailovic. Nonequilibrium electronic and structural Jahn-Teller dynamics in $(NbSe_4)_3I$. *Physical Review B (Condensed Matter and Materials Physics)*, 74(8):085211, 2006. doi: 10.1103/PhysRevB.74.085211. URL `http://link.aps.org/abstract/PRB/v74/e085211`.

[119] G. Travaglini and P. Wachter. Charge-density-wave-phase–mode evidence in one-dimensional $K_{0.3}MoO_3$. *Phys. Rev. B*, 30(4):1971–1978, Aug 1984. doi: 10.1103/PhysRevB.30.1971.

[120] D. C. Johnston. Thermodynamics of Charge-Density Waves in Quasi One-Dimensional Conductors. *Phys. Rev. Lett.*, 52(23):2049–2052, Jun 1984. doi: 10.1103/PhysRevLett.52.2049.

[121] S. Williamson, G. Mourou, and J. C. M. Li. Time-Resolved Laser-Induced Phase Transformation in Aluminum. *Phys. Rev. Lett.*, 52(26):2364–2367, Jun 1984. doi: 10.1103/PhysRevLett.52.2364.

[122] J. Cao, Z. Hao, H. Park, C. Tao, D. Kau, and L. Blaszczyk. Femtosecond electron diffraction for direct measurement of ultrafast atomic motions. *Applied Physics Letters*, 83(5): 1044–1046, 2003. doi: 10.1063/1.1593831. URL `http://link.aip.org/link/?APL/83/1044/1`.

[123] Y. Aharonov and D. Bohm. Significance of Electromagnetic Potentials in the Quantum Theory. *Phys. Rev.*, 115(3):485–491, Aug 1959. doi: 10.1103/PhysRev.115.485.

[124] R. A. Webb, S. Washburn, C. P. Umbach, and R. B. Laibowitz. Observation of h/e Aharonov-Bohm Oscillations in Normal-Metal Rings. *Phys. Rev. Lett.*, 54(25):2696–2699, Jun 1985. doi: 10.1103/PhysRevLett.54.2696.

[125] Yu. I. Latyshev, O. Laborde, P. Monceau, and S. Klaumünzer. Aharonov-Bohm Effect on Charge Density Wave (CDW) Moving through Columnar Defects in $NbSe_3$. *Phys. Rev. Lett.*, 78(5):919–922, Feb 1997. doi: 10.1103/PhysRevLett.78.919.

[126] M. I. Visscher and B. Rejaei. Collective charge density wave motion through an ensemble of aharonov-bohm rings. *EPL (Europhysics Letters)*, 43(6):617, 1998. URL http://stacks.iop.org/0295-5075/43/i=6/a=617.

[127] Sharon M. DeLand, George Mozurkewich, and L. D. Chapman. X-ray investigation of charge-density-wave pinning in blue bronze. *Phys. Rev. Lett.*, 66(15):2026–2029, Apr 1991. doi: 10.1103/PhysRevLett.66.2026.

[128] D. B. Chrisey and G. K. Hubler, editors. *Pulsed laser deposition of thin films*. Wiley-Interscience, 1994.

[129] O. C. Mantel, H. S. J. van der Zant, A. J. Steinfort, C. Dekker, C. Træholt, and H. W. Zandbergen. Thin films of the charge-density-wave oxide $Rb_{0.30}MoO_3$ by pulsed-laser deposition. *Phys. Rev. B*, 55(7):4817–4824, Feb 1997. doi: 10.1103/PhysRevB.55.4817.

[130] O.C. Mantel. *Mesoscopic Charge Density Wave Wires*. PhD thesis, Technische Universiteit Delft, 1999.

[131] M. Dressel and G. Grüner. *Electrodynamics of Solids*. Cambridge University Press, 2002.

[132] P. Gressier, L. Guemas, and A. Meerschaut. Preparation and structure of ditantalum iodide octaselenide, Ta_2ISe_8. *Acta Crystallographica Section B*, 38(11):2877–2879, Nov 1982. doi: 10.1107/S0567740882010176. URL http://dx.doi.org/10.1107/S0567740882010176.

[133] Sander van Smaalen, Erwin J Lam, and Jens Ldecke. Structure of the charge-density wave in $(TaSe_4)_2I$. *Journal of Physics: Condensed Matter*, 13(44):9923, 2001. URL http://stacks.iop.org/0953-8984/13/i=44/a=308.

[134] L. Forr, J. R. Cooper, A. Jnossy, and M. Maki. Hall effect in the charge density wave system $(TaSe_4)_2I$. *Solid State Communications*, 62(10):715 – 718, 1987. ISSN 0038-1098. doi: DOI:10.1016/0038-1098(87)90415-7. URL http://www.sciencedirect.com/science/article/B6TVW-46P7JWJ-3R6/2/2d8737f24e2b4a46b6339931727aa26e.

[135] C. Bansal and K. Surendranath. Thermopower behaviour of incommensurate charge density wave systems – $(NbSe_4)_{10/3}I$ and $(TaSe_4)_2I$. *Solid State Communications*, 76(2):209 – 212, 1990. ISSN 0038-1098. doi: DOI:10.1016/0038-1098(90)90544-L. URL http://www.sciencedirect.com/science/article/B6TVW-46Y3CST-SF/2/9ca05fe38c2d3d47d70fe803812505e8.

[136] P. Gressier, M.H. Whangbo, A. Meerschaut, and J. Rouxel. Electronic structures of transition-metal tetrachalcogenides $(MSe_4)_nI$ (M = Nb, Ta). *Inorganic Chemistry*, 23 (9):1221–1228, 1984.

[137] H.P. Geserich, G. Scheiber, M. Dorrler, F. Lvy, and P. Monceau. Optical investigation of the Peierls gap in the chain-like conductor $(TaSe_4)_2I$. *Physica B+C*, 143(1-3):198 – 200, 1986. ISSN 0378-4363. doi: DOI:10.1016/0378-4363(86)90093-8. URL http://www.sciencedirect.com/science/article/B6X43-46FJ154-54/2/5886f736b2b2b416aaf63bff61598a2d.

[138] Z. Z. Wang, M. C. Saint-Lager, P. Monceau, M. Renard, P. Gressier, A. Meerschaut, L. Guemas, and J. Rouxel. Charge density wave transport in $(TaSe_4)_2I$. *Solid State Communications*, 46(4):325 – 328, 1983. ISSN 0038-1098. doi: DOI:10.1016/0038-1098(83)90662-2. URL http://www.sciencedirect.com/science/article/B6TVW-46Y3BDG-DF/2/6fbe8c6fbf98e0df93275979c0bdabde.

[139] M. Maki, M. Kaiser, A. Zettl, and G. Grner. Charge density wave transport in a novel inorganic chain compound, $(TaSe_4)_2I$. *Solid State Communications*, 46(7):497 – 500, 1983. ISSN 0038-1098. doi: DOI:10.1016/0038-1098(83)90676-2. URL http://www.sciencedirect.com/science/article/B6TVW-46NY3V3-25R/2/e00a20a393583aaf6ebf106a3a89ab78.

[140] C Roucau, R Ayroles, P Gressier, and A Meerschaut. Electron microscopy study of transition-metal tetrachalcogenide $(MSe_4)_nI$ (M=Nb, Ta). *Journal of Physics C: Solid State Physics*, 17(17):2993, 1984. URL http://stacks.iop.org/0022-3719/17/i=17/a=007.

[141] H Fujishita, M Sato, and S Hoshino. X-ray diffraction study of the quasi-one-dimensional conductors $(MSe_4)_2I$ (M=Ta and Nb). *Journal of Physics C: Solid State Physics*, 18(6):1105, 1985. URL http://stacks.iop.org/0022-3719/18/i=6/a=007.

[142] S. Sugai, M. Sato, and S. Kurihara. Interphonon interactions at the charge-density-wave phase transitions in $(TaSe_4)_2I$ and $(NbSe_4)_2I$. *Phys. Rev. B*, 32(10):6809–6818, Nov 1985. doi: 10.1103/PhysRevB.32.6809.

[143] J. P. Pouget and R. Comes. *Charge Density Waves in Solids*, volume 25 of *Modern Problems in Condensed Matter Sciences*. New York: Elsevier, 1989.

[144] J.P. Pouget, C. Noguera, A.H. Moudden, and R. Moret. Structural study of the charge-density-wave phase transition of the blue bronze : $K_{0.3}MoO_3$. *J. Phys. France*, 46(10):1731–1742, 1985. doi: 10.1051/jphys:0198500460100173100. URL http://dx.doi.org/10.1051/jphys:0198500460100173100.

[145] S. Girault, A. H. Moudden, and J. P. Pouget. Critical x-ray scattering at the Peierls transition of the blue bronze. *Phys. Rev. B*, 39(7):4430–4434, Mar 1989. doi: 10.1103/PhysRevB.39.4430.

[146] D. Berner, G. Scheiber, A. Gaymann, H. Geserich, P. Monceau, and F. Lévy. Temperature dependence of the Peierls gap in $(TaSe_4)_2I$. *J. Phys. IV France*, 03:255–258, 1993. doi: 10.1051/jp4:1993251. URL http://dx.doi.org/10.1051/jp4:1993251.

[147] A. Schwartz, M. Dressel, B. Alavi, A. Blank, S. Dubois, G. Grüner, B. P. Gorshunov, A. A. Volkov, G. V. Kozlov, S. Thieme, L. Degiorgi, and F. Lévy. Fluctuation effects on the electrodynamics of quasi-one-dimensional conductors above the charge-density-wave transition. *Phys. Rev. B*, 52(8):5643–5652, Aug 1995. doi: 10.1103/PhysRevB.52.5643.

[148] Tomoyuki Sekine, Taisaku Seino, Mitsuru Izumi, and Etsuyuki Matsuura. Raman study of charge-density-wave phase transition in quasi-one-dimensional conductor $(TaSe_4)_2I$. *Solid State Communications*, 53(9):767 – 771, 1985. doi: DOI:10.1016/0038-1098(85)90216-9. URL http://www.sciencedirect.com/science/article/B6TVW-46MFJF7-2CB/2/7596a2e0983f287cd74019e93032227c.

[149] A. Zwick, M.A. Renucci, P. Gressier, and A. Meerschaut. A raman study of the peierls transition in $(TaSe_4)_2I$. *Solid State Communications*, 56(11):947 – 952, 1985. doi: DOI:10.1016/S0038-1098(85)80031-4. URL http://www.sciencedirect.com/science/article/B6TVW-4GSCH0R-9/2/ad1438ffcd6f44b97832094e19c078e3.

[150] D. C. Johnston, M. Maki, and G. Grner. Influence of charge density wave fluctuations on the magnetic susceptibility of the quasi one-dimensional conductor (tase4)2i. *Solid State Communications*, 53(1):5 – 8, 1985. ISSN 0038-1098. doi: DOI:10.1016/0038-1098(85)90672-6. URL http://www.sciencedirect.com/science/article/B6TVW-46NXXKS-Y/2/a88301753e6ac5e19978a3968281ec8c.

[151] Allen Rothwarf and B. N. Taylor. Measurement of Recombination Lifetimes in Superconductors. *Phys. Rev. Lett.*, 19(1):27–30, Jul 1967. doi: 10.1103/PhysRevLett.19.27.

[152] Yu. N. Ovchinnikov and V. Z. Kresin. Nonstationary state of superconductors: Application to nonequilibrium tunneling detectors. *Phys. Rev. B*, 58(18):12416–12421, Nov 1998. doi: 10.1103/PhysRevB.58.12416.

[153] J. Demsar, R. Hudej, J. Karpinski, V. V. Kabanov, and D. Mihailovic. Quasiparticle dynamics and gap structure in $HgBa_2Ca_2Cu_3O_{8+\delta}$ investigated with femtosecond spectroscopy. *Phys. Rev. B*, 63(5):054519, Jan 2001. doi: 10.1103/PhysRevB.63.054519.

List of Figures